AN ABSTRACT OF THE DISSERTATION OF

Carmine C. Chickadel for the degree of Doctor of Philosophy in Oceanography
presented on September 7, 2007.
Title: Remote Measurements of Waves and Currents over Complex Bathymetry

Abstract approved: _____
Robert A. Holman

Waves are the primary input of energy in the nearshore region, and together with the currents forced through the transfer of momentum that occurs during the wave breaking process they are the principal mechanism for sediment transport in the nearshore. The basic physics of waves and currents are thought to be well understood, and simple models for waves and current interacting with simple (alongshore-uniform bathymetry) generally agree with *in situ* measurements. However, alongshore variability is ubiquitous, and the predictability of waves and currents over complex bathymetry is an important research topic. Significant effort has been placed into understanding and predicting (modeling) the kinematics and dynamics of waves and currents, but the accuracy of these models are largely untested, due to the lack of appropriate wave and current measurements.

This dissertation first details the development and application of an optical remote sensing technique to measure the shape of wave frequency-direction spectra over large scale complex bathymetry. The optical wave spectral estimation technique is based on the wave slope dependence of reflected skylight, and while not a metric of the absolute wave energy, the measurement technique is shown to agree with the frequency and directional distributions of *in situ* measurements. Simultaneously, the optical technique offers increased directional resolution. Maps of the wave direction field over a submarine canyon, using the optical technique, show dramatic changes in the wave divergence and convergence which coincides with details of the large scale bathymetry gradients.

The last section of this dissertation analyzes 14 months of surf zone longshore currents measured from a two-dimensional array using a previously described optical remote sensing technique. Based on metrics developed in the study, the longshore currents are shown to be alongshore nonuniform for the majority (70%) of the observations, suggesting that a simple one-dimensional force balance circulation model is not generally applicable. Related tests of a point model only show moderate skill when predicting the peak longshore current (rms error 0.38 m/s). Though cases of two-dimensional circulation (i.e. rip currents) are shown to coincide with alongshore-variable bathymetry, a metric of the degree of alongshore bathymetry variability, γ_B, has poor skill of predicting the strength of spatial longshore current variability.

Remote Measurements of Waves and Currents over Complex Bathymetry

by
Carmine C. Chickadel

A DISSERTATION

submitted to

Oregon State University

in partial fulfillment of
the requirements for the
degree of

Doctor of Philosophy

Presented September 7, 2007
Commencement June 2008

Doctor of Philosophy dissertation of Carmine C. Chickadel presented on September 7, 2007.

APPROVED:

Major Professor, representing Oceanography

Dean of the College of Oceanic & Atmospheric Sciences

Dean of the Graduate School

I understand that my dissertation will become part of the permanent collection of Oregon State University libraries. My signature below authorizes release of my dissertation to any reader upon request.

Carmine C. Chickadel, Author

ACKNOWLEDGEMENTS

Even after putting down the words under these pages, and probably because of it, I am still amazed when I look at the waves on the beach and the rolling sand. I can't imagine that there are not several lifetimes of thought that might pass to really understand it. In this actual sea of unknowing I am buoyed by the thrill and happiness that I get from watching it happen and appreciating it.

The first thanks goes to my advisor, Rob Holman, for providing me the ultimate opportunity to pursue my doctorate, and letting me take my sweet time about it. Furthermore, I appreciate the scientific view and critical thinking he afforded me. Thank you to my committee members, Tuba Ozkan-Haller for her incredible ability to teach even me, Mick Haller for his focused and thoughtful examination of science I presented, Paul Komar for his vast nearshore experience and perspective, and Mike Freilich for all of the signal processing knowledge he imparted.

I would not have enjoyed graduate school nearly as much without the many friends I shared it with. Thanks to Jason Chaytor, Matt Arsenault, Heather Benway, Jason Killian, Joe Long, Meg Palmsten, Kristen Splinter, Dan Clark, Kevin McGown and Linden Clarke (and family) among many other I can't fit in these few pages. I will single out John "Squarepants" Stanley for a special thanks. I can only hope there are other graduate students to laugh at your jokes, and get them while I'm gone from the CIL, 'cause how can I be in two places at once when I'm not anywhere at all.

Thank you to my grandmother and artistically inclined parents, brother and sister for always understanding my science-y part and encouraging me to always pursue it. I owe the most thanks to my wife and sons for wanting me to come home when I was late and continuing on without me when I was not around for dinner and weekends. Thanks you for providing me with the love and support I needed.

This work was funded by the Office of Naval Research Coastal Geosciences program under grant number N0001402-1-015. In situ measurements from NCEX

were kindly provided by Steve Elgar and Bob Guza, and offshore wave measurements from Duck were provided by the staff and researchers at the Field Research Facility.

TABLE OF CONTENTS

TABLE OF CONTENTS (Continued)

LIST OF FIGURES

LIST OF FIGURES (Continued)

LIST OF FIGURES (Continued)

LIST OF FIGURES (Continued)

LIST OF TABLES

LIST OF APPENDIX FIGURES

Remote Measurements of Waves and Currents over Complex Bathymetry

Chapter 1: Introduction

Surface gravity waves are generated at sea by persistent winds and disperse as they approach the ocean's margins. The character of the waves, defined by their height, distance from trough to crest, and period, the time it takes for the passage of two consecutive wave crests to pass a stationary point, depends on the duration and speed of the wind and the fetch over which it blows. A continuum of wave periods and heights propagating in different directions are generated, and the details of the free surface of the ocean motions can be described by the superposition of multiple wave trains, each of single peak period and direction. This is exactly the definition of a sampled two-dimensional wave spectrum, where the wave variance, or energy, is partitioned into discrete blocks of frequency (the inverse of wave period) and direction. The wave spectrum is therefore a compact way of representing the wave field.

The kinematics and dynamics of waves in deep water are well described by linear wave theory [*Mei*, 1983]. Waves propagating onshore begin to be affected by shallower water depths near the shoreline. This is marked by decreases in wave phase speed and transformations in the wave profile from a simple sinusoid to a more peaked, skewed profile. In a narrow banded wave spectrum shoaling is evident by the development of frequency harmonics and directional convergence, if bathymetry contours are straight and parallel. In the more typical case of complex bathymetry, trenches or depressions cause wave divergence, defocusing, while shoals cause wave convergence, or focusing. In the case where the waves do not lose energy through dissipation, their wave height will increase when they are convergent and decrease when they diverge.

In the surf zone, a region close to shore (typically less than a few meters mean water depth), waves develop increasing asymmetry until they eventually

become unstable and "break" as the peaks collapse, entrain air, and transfer momentum to the water column. This thrust, derived from gradients in the radiation stress [*Longuet-Higgins and Stewart*, 1964], can occur whenever the wave height changes, and is available to push water in the cross-shore and alongshore directions. Cross-shore gradients in onshore directed radiation stress are balanced by pressure gradients due to sea surface elevation changes, and in the alongshore, when wave approach obliquely to the shoreline, currents are forced and are mainly balanced by friction with the bottom. Mean alongshore directed currents, alternately called longshore currents, are parallel to the shoreline and are strongest at the location of maximum wave forcing. Over plane beaches, where wave characteristics (height and direction) and bathymetry are uniform alongshore, longshore currents have a simple single peaked profile maximum near the maximum of wave forcing tapering to zero at the shoreline and near the offshore edge of the surf zone. Over more complex, alongshore non-uniform bathymetry, the subsequent variations in the alongshore wave height and direction cause variations in the magnitude and direction of this wave-driven forcing. In turn, the complex wave patterns force alongshore pressure gradients, and alongshore variable cross-shore and longshore currents. Rip currents, cross-shore directed narrow current jets, are a typical feature of complex bathymetry and occur at the convergence of longshore currents, usually coincident with cross-shore parallel depressions or channels.

Waves and the resulting mean currents result in the transport of sediment, which in net effect can produce erosion or accretion at the shoreline. Increased societal demands on the coastal regions of the world have spurred significant scientific and engineering interest in the physical behavior of the nearshore, with the primary goal of predicting morphologic change (i.e. erosion and accretion), which, in turn, necessitates accurate predictions of waves and currents. Simple point and one dimensional (horizontal) profile wave and current models assume alongshore uniform bathymetry and waves. However, alongshore variability is

arguably the most common state of nearshore bathymetry [*Lippmann and Holman*, 1990], so that the predictability of waves and currents over complex bathymetry is an important research topic. Models that can be used over general (complex) bathymetry to predict waves and currents in two (horizontal) or three dimensions are available, but the accuracy of those models are largely untested, and have only seldom compared with field data due to the lack of appropriate wave and current measurements. The nearshore is a difficult sampling environment, where pounding waves, strong currents and moving sediment make *in situ*, long-term (weeks and months to years) sampling of a dense array (tens of meters spacing) over a large spatial area ($10^4 m^2$ to $10^6 m^2$) a nearly impossible challenge. Furthermore, due to their sensitivity to the bottom boundary, wave and current models (except point longshore current models) require extensive, accurate and hard-to-measure bathymetry.

A clear engineering advantage lies in predicting sediment transport using the simplest wave and current models, specifically those models assuming alongshore uniform forcing and bathymetry. However, appropriate observations to examine and characterize the large spatial and long-term temporal scales of variability of currents and waves are lacking, and not likely to be sampled via *in situ* instruments. Remote sensing is a logical choice to provide the necessary observations, and work, especially in the last twenty or more years, has advanced technology and techniques. Optical imaging, in particular, can provide the large spatial coverage while simultaneously achieving fine spatial resolution, high frequency sampling, low cost and easy deployment [*Holman et al.*, 1993; *Holman and Stanley*, 2007].

Optical signals in the nearshore are especially rich. The reflected light from waves slope variation, bright intensity from breaking waves, and residual foam are apparent to the unaided eye, and these signals have been exploited to estimate nearshore circulation [*Holland et al.*, 2001; *Chickadel et al.*, 2003], open ocean wave statistics [e.g. *Cox and Munk*, 1954], swash statistics [*Holman and Guza*,

1984; *Holland and Holman*, 1993], and topography and bathymetry [*Holman et al.*, 1991; *Holland and Holman*, 1997; *Stockdon and Holman*, 2000; *Dugan et al.*, 2001b; *Aarninkhof et al.*, 2005].

This dissertation describes research using optical remote sensing to measure waves and currents in the nearshore, with the ultimate goal of characterizing their dynamics over complex bathymetry. Chapter 2 presents the development and field tests of an optical technique to measure directional wave spectra in the nearshore. The technique provides highly resolved spectra using a reduced set of optical time series data, based on an existing nonparametric (maximum likelihood) spectral estimation technique. Chapter 3 describes an application of the optical directional spectrum technique to quantify the shoaling wave field at Black's Beach in La Jolla, California. It has been observed for many years that the waves there are refracted over the complex bathymetry associated with a submarine canyon close to shore. Chapter 4 transitions from waves to how waves force currents, and presents a long-term analysis of mean longshore currents, based on remote sensing measurements. The analysis documents alongshore variability of observed currents and its coincidence with alongshore variable nearshore bathymetry. Chapter 5 presents a summary of combined conclusions for these three manuscripts.

1.1 References

Aarninkhof, S.G.J., B.G. Ruessink, and J.A. Roelvink, (2005), Nearshore subtidal bathymetry from time-exposure video images, in *Journal of Geophysical Research*.

Chickadel, C.C., R.A. Holman, and M.F. Freilich (2003), An optical technique for the measurement of longshore currents, *Journal of Geophysical Research*, *108* (C11), 3364.

Cox, C., and W. Munk (1954), The measurement of the roughness of the sea surface from photographs of the sun's glitter, *Journal of the Optical Society of America*, *44*, 838-850.

Dugan, J.P., C.C. Piotrowski, and J.Z. Williams (2001b), Water depth and surface current retrevials from airborne optical measurements of surface gravity wave dispersion, *Journal of Geophysical Research*, *106* (C8), 16903-16915.

Holland, K.T., and R.A. Holman (1993), The statistical distribution of swash maxima on natural beaches, *Journal of Geophysical Research*, *98* (C6), 10,271-10,278.

Holland, K.T., and R.A. Holman (1997), Video estimation of foreshore topography using trinocular stereo, *Journal of Coastal Research*, *13* (1).

Holland, K.T., J.A. Puleo, and T.N. Kooney (2001), Quantification of swash flows using video-based particle image velocimetry, *Coastal Engineering*, *44*, 65-77.

Holman, R.A., and R.T. Guza (1984), Measuring run-up on a natural beach, *Coastal Engineering*, *8*, 129-140.

Holman, R.A., T.C. Lippmann, P.V. O'Neill, and K. Hathaway (1991), Video estimation of subaerial beach profiles, *Marine Geology*, *97*, 225-231.

Holman, R.A., J. A.H. Sallenger, T.C. Lippmann, and J.W. Haines (1993), The application of video image processing to the study of nearshore processes, *Oceanography*, *6* (3), 78-85.

Holman, R.A., and J. Stanley (2007), The history and technical capabilities of Argus, *Coastal Engineering*, *54* (6-7), 477-491.

Lippmann, T.C., and R.A. Holman (1990), The spatial and temporal variability of sand bar morphology, *Journal of Geophysical Research*, *95* (C7), 11,575-11,590.

Longuet-Higgins, M.S., and R.W. Stewart (1964), Radiation stresses in water waves; a physical discussion, with applications, *Deep-Sea Research*, *11*, 529-562.

Mei, C.C., *The Applied Dynamics of Ocean Surface Waves*, 740 pp., John Wiley & Sons, New York, N.Y., 1983.

Stockdon, H.F., and R.A. Holman (2000), Estimation of wave phase speed and nearshore bathymetry from video imagery, *Journal of Geophysical Research*, *105* (C9), 22,015-22,033.

Chapter 2: Optical estimation of nearshore directional wave spectra

2.1 Abstract

A technique to estimate spectral shape of the wave field outside of the surf zone using remote optical sensing is presented and validated. The technique samples optical radiance intensity time series from a two-dimensional lag array of pixel elements. Sampled times series are processed and $S(f,k,\theta)$, frequency-wavenumber-directional spectra, are calculated using a standard maximum likelihood estimation technique. A simple radiance to sea surface elevation modulation transfer function, k^{-2}, is used to transform optical spectra to sea surface elevation spectra, which are then integrated with respect to wavenumber to generate $S(f,\theta)$. Synthetic tests indicate good theoretical performance of the optical technique. Ground truth tests were conducted over varying lighting conditions with spectra estimated from collocated pressure and velocity measurements (PUV) taken during the Nearshore Canyon Experiment, on 31 October 2003. A total of 96 spectra from six locations outside of the surf zone were compared. Agreement of optical and *in situ* frequency spectral shape was good (average correlation, ρ = 0.88). The standard deviation difference for peak direction at the peak frequency was 5°. Directional spreading in PUV spectra were 52% wider than optical spectra (mean difference of 12°). Examples of bimodal directional spectra, likely due to wave shadowing by offshore islands, were also measured with the optical technique.

2.2 Introduction

Waves generated offshore are the primary source of momentum and energy into the nearshore. These waves typically undergo large changes as they refract and shoal over offshore bathymetry, then as they break in the surf zone. Because all the details of nearshore circulation and the resulting sediment transport are dependent

on the direction and strength of local wave forcing, the transformed wave field must be adequately specified or modeled at all locations of interest. Single statistical representations of the wave field (e.g. peak direction and frequency) are often an oversimplification of the wave field unsuitable, to describe complex wave fields. Complex wave fields can result, for example, from shoaling over irregular bathymetry or from shadowing by offshore islands [e.g. *Pawka*, 1983]. In the latter case, bimodal directional spectra at the peak frequency are common and are not well described by a single direction. By extension, modeled dynamics resulting from the assumption of a simple, single-peaked directional spectra distribution would not be useful due to obvious potential inaccuracy.

Wave spectra are compact ways of representing the distribution of wave variance with direction and frequency and are a common method to characterize any nearshore site. Spectral data are used in several ways. Numerical models require that spectra or similar wave characterizations be specified along model boundaries as an input boundary condition. To validate these models, predicted spectra must be compared with spectral measurements made in the domain interior. For more complicated assimilative models, differences between predictions and measurements can be formally incorporated into correction schemes.

A number of *in situ* instrument solutions for measuring wave spectra have developed, including pressure sensor and current meter combinations (PUV sensors), pitch-and-roll buoys, and slope arrays. Each is compact or relatively compact and has a performance that has been well studied and characterized. However, costs of installation and maintenance are significant, and the logistics of maintaining these sensors in an active surf zone preclude long duration installations or the high-density sampling that is needed to represent wave shoaling on complex bathymetries. Finally, directional resolution for compact in-situ sensors is usually relatively coarse, hence the details of the directional spread derived from these point type arrays are lacking [*Longuet-Higgins et al.*, 1963; *Oltman-Shay and Guza*, 1984]. For example, the work by *Oltman-Shay and Guza*, [1984] shows that

bimodal directional spectra are hard to resolve for peak separations of approximately less than 90°.

Remote sensing offers an alternate set of methods that can be used to overcome the above logistic difficulties and allow data collection to be carried out over extended periods of time or in denied areas. Perhaps the best known of the previous papers is the work by *Cox and Munk* [1954] that derived statistics of the distribution of sea surface slopes based on sun glitter patterns, but an extended set of experiments has built on the principles of wave visibility away from the sun glitter region to estimate directional spectra from single photographs [*Stilwell*, 1969] or directional-frequency spectra from a sequence of images [*Gotwols and Irani*, 1980; *Lubard et al.*, 1980; *Monaldo and Kasevich*, 1981b; *Dugan et al.*, 2001a] . Most of these methods derive spectra from two or three-dimensional Fourier transforms of spatial and temporal video data.

Methods to directly determine wave spectral shape from remote optical data require a model of the relationship between optical signals and the wave field, known as the Modulation Transfer Function or MTF [*Walker*, 1994, see also section 2]. The MTF is complex and nonlinear, though the degree of non-linearity is not well known for general situations and may be approximately linear for a subset of viewing conditions [*Monaldo and Kasevich*, 1981a]. Further numerical models of optical wave spectra, using more complicated forms of the MTF also suggest the MTF was approximately linear, though the studies were limited in scope by existing computational power [*Chapman*, 1981; *Chapman and Irani*, 1981].

Issues with past optical remote sensing efforts have limited measurements of wave spectra and prevented regular use of optical remote sensing for waves in the field. Primarily, complication of the perspective distortion of the image, due to low grazing angle of the sea surface, are only considered as a secondary corrections to the spectrum [e.g. *Stilwell and Pilon*, 1974; *Lubard et al.*, 1980; e.g. *Gotwols and Irani*, 1982]. Attempts to minimize the effect of the perspective warping by

using narrow fields of view limit the maximum wavelength that can be imaged. With the exception of the work by *Dugan et al.* [2001a], the previously referenced papers only consider short gravity waves, O(0.1m) to O(1m), shorter than wavelengths expected for swell waves (O(10-100m) for wave periods around 10s in depths of a few meters, and longer in intermediate to deep water) typically considered the most important forcing in the nearshore, considered here. Lastly, the degree of field testing has been limited to isolated case studies [*Cox and Munk*, 1954; *Stilwell*, 1969; *Stilwell and Pilon*, 1974; *Gotwols and Irani*, 1980; *Dugan et al.*, 2001b].

In this study, we use optical video data – time series of intensity variations – from outside of the surf zone to estiamte energy-normalized frequency-directional wave spectra. The determination of absolute spectral energy magnitudes is beyond the scope of this paper; instead we will compare characteristics of optically and *in situ* derived wave spectral shape. Specifically, our work differs from previous papers in three ways. First, our wavenumber analysis will be based on MLE methods applied to a sparse, non-uniformly spaced array of pixels rather than the full image data needed for Fourier methods, reducing the sampling needs of the method by many orders of magnitude. Second, our method will be applied to low grazing angle situations such as cameras observing from land based vantage points such as headlands and towers, rather than overhead aircraft. Third, our focus will be on resolution of the longer ocean waves (order 10s periods) that dominate the energy fluxes that drive nearshore processes.

The form of this paper is as follows. A mathematical background for full non-linear MTF and motivation for the use of a linear MTF is presented in section 2. Section 3 details the optical methods used to estimate wave spectral shapes, including the use of a two-dimensional array developed specifically for this study, and its application to maximum likelihood spectral estimation technique (section 3.1). We test the linearity of the modulation transform function using realistic, synthetic optical data over a range of lighting conditions (clear and overcast sky)

and wave spectra (section 3.2). Section 4 details ground-truth testing with wave spectra calculated from *in situ* data from the 2003 Nearshore Canyon Experiment, before discussion (section 6) and conclusions are presented (section 7).

2.3 Wave visibility

2.3.1 Radiance model

The solid geometry to describe the optical processes involved for viewing waves can be confusing. To simplify we follow the majority of the straightforward geometric labeling conventions described by *Chapman* [1981] (Figure 2.1). The coordinate system is right handed with the positive *x* axis pointing offshore, the *y* axis parallel to the shoreline and *z* positive up. Unit vectors describing the camera look direction, sea surface normal, incident radiance paths and sun position in the sky are all labeled $\hat{r}$. All nadir (w.r.t. the negative *z* axis), and zenith (w.r.t. the positive *z* axis) angles are labeled γ, and azimuth angles (measured counter-clockwise from the positive *x* axis) are labeled α. Subscripts *c*, *n*, *i*, and *s* of the vectors and angles refer to the camera, surface normal, incident ray, and sun, respectively. The incident ray is related to the surface normal and camera rays by simple geometric reflection,

$$\hat{r}_i = 2\hat{r}_n(\hat{r}_n \cdot \hat{r}_c) - \hat{r}_c, \tag{1}$$

where $(\cdot)$ is the scalar product. This single scattering optical model neglects multiple reflections and shadowing, both of which may become important at low grazing angles.

Wave visibility is a function of the wave slope and the reflected light. The radiance, *I*, reaching an optical sensor (*e.g.* retina or camera sensor) can be expressed as

$$I = L(\gamma_i, \alpha_i)R(\omega), \tag{2}$$

and is composed of the sky radiance distribution, *L*, modified by the Fresnel reflection coefficient, *R*. The incidence sky radiance is a function of zenith angle, γ_i, and azimuth angle, α_i. ω is the angle of incidence of the sky radiance with

respect to the sea surface normal. This model assumes negligible contributions due to upwelling radiance from below the water's surface (due to low grazing angles) or from atmospheric path scattering (due to short optical path lengths). The reflectivity of the surface for an unpolarized radiance source is described by the Fresnel reflection coefficient [*Walker*, 1994],

$$R(\omega) = \frac{1}{2}\left[\frac{\sin^2(\omega-\omega')}{\sin^2(\omega+\omega')} + \frac{\tan^2(\omega-\omega')}{\tan^2(\omega+\omega')}\right] \tag{3}$$

where ω' is the angle of refraction related to ω by Snell's law, $\sin(\omega) = 1.34\sin(\omega')$. When ω equals the Brewster angle (~53 degrees) the reflected light will be completely horizontally polarized.

For the purposes of this paper, only sky radiance models for clear and fully overcast conditions will be considered. The clear sky model we use here [*Hopkinson*, 1954],

$$L_c = K_c\left[\frac{1+\cos^2\mu}{1-\cos\mu}\right]\left[1-\exp\left(\frac{-0.32}{\cos\gamma_i}\right)\right] \tag{4a}$$

where

$$\mu = \cos^{-1}\left(\cos\gamma_s\cos\gamma_i + \sin\gamma_s\sin\gamma_i\cos(\alpha_s-\alpha_i)\right), \tag{4b}$$

is dependent on the sun's zenith, γ_s, and azimuth, α_s, angles, and the constant K_c. Physically, μ is the angle between $\hat{r}_s$ and $\hat{r}_i$. The overcast sky model used here [*Moon and Spencer*, 1942],

$$L_o = K_o(1+2\cos\gamma_i) \tag{5}$$

depends only on the zenith angle. The complexity of modeling the sky luminance for more general situations (i.e. partially cloudy skies) is beyond the scope of this paper, but this may be overcome by having simultaneous measurements through an upward pointing camera, or possibly through approximation by time-averaged images of the sea surface [*Lubard et al.*, 1980].

2.3.2 Slope to radiance modulation transfer function

Accurate estimation of wave spectra from radiance transmitted to the optical sensor depends on the accuracy of the modulation transfer function (MTF) between the two. The MTF for a given wave spectrum, using equations (1) through (5) is nonlinear and is often approximated by a first or second-order Taylor expansion model [*Stilwell*, 1969; *Stilwell and Pilon*, 1974; *Kasevich*, 1975; *Monaldo and Kasevich*, 1981b]. To develop an intuitive understanding of wave visibility, the first-order Taylor approximation of equation (2) [see *Stilwell*, 1969] is,

$$I \approx I_{\gamma_n=0} + \gamma_n \cos(\alpha_n - \alpha_c) K_1 \tag{6}$$

assuming small wave slopes (i.e. $\gamma_n < 20$ degrees), no azimuthal dependence on the sky radiance distribution, L, and where K_1 is a constant. According to (6), wave visibility has a linear first-order dependence on the look-direction wave slope,

$$\gamma_n \cos(\alpha_n - \alpha_c) \approx -\frac{\partial \eta}{\partial x}\cos(\alpha_c) - \frac{\partial \eta}{\partial y}\sin(\alpha_c), \tag{7}$$

where η is the time and space dependent surface elevation at the view point. According to (7) the highest optical contrast for waves occurs when they are viewed along the direction of their propagation (when $\alpha_n = \pm\alpha_c$), and waves are generally not visible when viewing them along-crest.

A second order expansion of wave visibility [e.g. *Kasevich*, 1975] is

$$\begin{aligned} I \approx I_{\gamma_n=0} &+ \gamma_n \cos(\alpha_n - \alpha_c) K_1 + \frac{\gamma_n^2}{2}\cos^2(\alpha_n - \alpha_c) K_2 \\ &+ \frac{\gamma_n^2}{2}\sin^2(\alpha_n - \alpha_c)\cot(\gamma_c) K_3 \end{aligned}, \tag{8}$$

where K_2 and K_3 are constants. As the camera tilt approaches horizontal, the term $\cot(\gamma_c)$ in (8) goes to zero, and the dependence on look-direction wave slope is similar to (6) and (7). For an increasing grazing angle (decreasing nadir angle) this term is of greater importance and becomes dependent on the square of the cross-look wave slope,

$$\gamma_n^2 \sin^2(\alpha_n - \alpha_c) \approx \left[-\frac{\partial \eta}{\partial y}\cos(\alpha_c) + \frac{\partial \eta}{\partial x}\sin(\alpha_c) \right]^2 . \quad (9)$$

The above equations represent the observed radiance for a simple, overcast sky. For sunny or partially cloudy skies, these approximations will show decreasing accuracy. Nevertheless, the increased complexity of full formulations is daunting and our main goal will be to test the accuracy of these simplified relations.

Numerical Monte Carlo simulations by *Chapman and Irani* [1981] reinforce the principles outlined in the Taylor approximations of the slope-to-radiance transformations. First, the authors find that the optical response at the camera to waves is approximately proportional to the wave slope and optical directional wave spectra only differ significantly from modeled spectra as wave azimuths exceed 50 to 60 degrees from the direction of camera look. Furthermore, simulations of lighting conditions for varied sun position for clear skies (using a sun zenith angle, γ_s, of 45 degrees and camera nadir angle, γ_c, of 60 degrees) suggest that a linear MTF is appropriate for a sun azimuth of up to 135 degrees relative to the camera look azimuth (sun behind the camera look direction or up to 45 degrees forward). Simulations for uniformly overcast skies show that the optical response at the camera due to waves is nearly independent of viewing [*Chapman*, 1981], though the linearity of the overcast sky MTF has not been studied.

For the purposes of this paper, we assume the spectral MTF, Γ, to be the simplest linear model, neglecting azimuthal variability and depending only on the linear approximation of slope dependence for wave visibility. Hence,

$$S'(f,k,\theta) = \hat{S}(f,k,\theta)\Gamma(k) \quad (10a)$$

$$\Gamma(k) = k^{-2} \quad (10b)$$

where S' is the estimate of the true wave spectral density, $\hat{S}$ is the observed optical spectral density, f (Hz) is frequency, k (m^{-1}) is wavenumber magnitude, and θ (radians) is direction of wave propagation defined anti-clockwise from 0 for shoreward propagation. In the section 3.1 the maximum likelihood method of

spectral estimation is discussed. In section 3.2 we will investigate the linear MTF assumption through synthetic optical tests.

2.4 Optical wave spectral technique

2.4.1 Frequency-direction spectral estimation

Previous algorithms for directional spectral estimation from optical data have been based on Fourier transform methods in time and both spatial dimensions. These, in turn, required dense sampling from a regular grid of pixels in the domain of interest. Pixel spacing was determined by the minimum wavelength of waves with significant energy while the span of the domain had to be many wavelengths of the longest wavelength of interest. For the current case of sampling from remote video monitoring stations [*Holman and Stanley*, 2007], this would require the return of a prohibitive amount of data from the station to the central lab.

The technique presented here is based on a Maximum Likelihood Estimator (MLE; [*Davis and Regier*, 1977] and described below) method of spectrum computation that makes the same assumption as Fourier methods of a homogeneous wave field over the sampling array, but bases the calculation on the cross-spectral relationships among a small number of spatially-lagged sampling locations. For this paper, the optical frequency-directional wave spectra are estimated with data from a sparse two-dimensional array of 17 sampling locations (Figure 2.2a), called an "alpha" array (so named because the symbol α is often used to indicate wave angle). The selection of particular x-y sampling locations is based on several criteria. The shortest resolvable wavelength (i.e. a Nyquist wavelength) is twice the length of the shortest lag in the array. The maximum wavelength that can be resolved scales with the full size of the array in a way that is best revealed by synthetic testing. Finally, the MLE method is based on cross-spectral characteristics as a function of spatial separation, or lag, between instruments. Thus, instrument locations are chosen to maximize the number of separate lags for

any particular number of instruments. For a two-dimensional analysis, both x and y oriented lags must be considered.

The basic form for the alpha array design is the perpendicular intersection of a six element linear array in the minor axis with a seven element linear array in the major axis, and the addition of four off-axis diagonal elements (Figure 2.2a). The alpha array is oriented with the minor array axis parallel to the cross-shore direction and the major axis parallel to the shoreline, and with a major to minor array aperture ratio (the l_y:l_x , or alongshore to cross-shore ratio) of 2:1. The suite of unique, non-zero lags between all possible instrument locations defines the "co-array". The co-array of the alpha array shows it densely spans the possible lag space up to the maximum array dimensions (Figure 2.2b). The cross-shore dimension of the alpha array is usually scaled to a typical expected wavelength, based on a representative peak frequency and water depth and assuming linear wave theory. For example, an alpha array designed for a 5.5s period wave in 5m water depth would have a cross-shore dimension of about 34m and an alongshore dimension of 68m. The ratio of shortest to longest lag in the cross-shore direction is 1:19, so the minimum lag would be 1.78m and the minimum resolvable wavelength (the Nyquist) would be 3.56m, approximately equivalent to a wave period of approximately 1.5s. Similarly, the longshore lag characteristics of the array determine the resolution characteristics of the array for determining the longshore component of wavenumber. In contrast to linear arrays, both wavenumber components are estimated independently without *a priori* assumptions of wave dispersion. Note that the true wavenumber resolution capability (*i.e.* spectral window) of the array is best examined using realistic synthetic tests, discussed below and detailed in Appendix A.

After design of the array locations in the *x*-*y* plane, the locations of corresponding pixel locations were computed for optical sampling in each camera view. Transformation between world coordinates (assuming a vertical coordinate

of mean sea level) and the corresponding image coordinates is determined through standard photogrammetric techniques [*Holland et al.*, 1997].

The maximum likelihood estimate (MLE) method [*Capon*, 1969; *Davis and Regier*, 1977], is used to calculate frequency-directional wave spectra from an alpha array. The MLE method has been used extensively for calculating directional wave spectra in the nearshore [*Regier and Davis*, 1977; *Pawka*, 1983; *Oltman-Shay and Guza*, 1984; *Freilich et al.*, 1990], and is chosen for this application because it can accept irregularly sampled (in space) data, can provide high resolution estimates, requires no *a priori* assumption of the wave field other than homogeneity, and is efficiently calculated.

The product of the data adaptive MLE method, a spectral estimate of the optical signal, $\hat{S}(f,k,\theta)$, is assumed to be composed of the weighted sum of all possible cross-spectral elements, $\hat{Q}_{nm}(f)$, derived from the observations at array locations

$$\hat{S}(f,k,\theta) = \sum_{n=1}^{N_e}\sum_{m=1}^{N_e} \alpha_{nm}(f,k,\theta)\hat{Q}_{nm}(f) \tag{11}$$

where N_e are the number of instruments in the array. The weights, α_{nm}, are chosen so that the estimator yields the minimum square error of the complex amplitude signal (a plane wave) in the presence of noise [*Capon et al.*, 1967]. The minimization leads to the solution

$$\hat{S}(k,\theta) = \left[\sum_{n=1}^{N_e}\sum_{m=1}^{N_e} \hat{Q}_{nm}^{-1} \exp[2\pi k(l_{x,nm}\cos\theta + l_{y,nm}\sin\theta)]\right]^{-1} \tag{12}$$

where $\hat{Q}_{nm}^{-1}$ is the nm^{th} element of the inverse cross-spectral matrix and $l_{x,nm}$ and $l_{y,nm}$ are the cross-shore and alongshore components of the spacings between the n^{th} and m^{th} instruments in the array, respectively. The frequency notation has been dropped in (12) since the spectral estimates are computed separately within a frequency band.

The MLE method estimates the variance for any wavenumber and direction component in each frequency band, not spectral density, therefore Parseval's theorem – which requires that the sum of the spectral components equal the total variance of the sample time series – is not automatically satisfied. The practice here is to renormalize the total variance within each frequency band so that

$$\Delta k \Delta\theta \sum_{j=1}^{N} \hat{S}(k_j, \theta_j) = \frac{1}{N_e} \sum_{n=1}^{N_e} \hat{Q}_{nn} , \tag{13}$$

where Δk and $\Delta\theta$ are the wavenumber and direction sample spacing at each of the N total k and θ locations. Choices for θ and k are arbitrary in MLE estimates of nearshore wave spectra, though some reasonable choices are clear. Specifically, spectral estimates can be constrained to onshore propagation directions, or $90° > \theta > -90°$. Guided by Fourier analysis analogies, sensible limits for wavenumber resolution used in this technique are $|l_{max}|^{-1} \leq k \leq (2|l_{min}|)^{-1}$, where l_{min} and l_{max} are the shortest and longest lags in the alpha array, and the Nyquist wavenumber for the array is $k_{nyq} = (2|l_{min}|)^{-1}$. Spacings ($\Delta k$ and $\Delta\theta$) within wavenumber and direction limits are just as arbitrary, though there is a trade off of smaller Δk and $\Delta\theta$ for a linear increase in computational time for processing MLE spectra. In subsequent analyses we use $\Delta\theta = 1°$ and $\Delta k = |l_{max}|^{-1}$ (for the design array considered above, $\Delta k \approx 0.0148 \text{m}^{-1}$). Comprehensive synthetic testing with of the alpha array and the MLE spectra are detailed in Appendix A. The tests reveal that the alpha array is well suited to resolve Gaussian directional distributions for wavenumbers less than k_{nyq} /6 based on various metrics including low normalized square error (NSE, equation A2) and the ability to accurately resolve the width of a directional peak and accurately identify peak locations in a bimodal distribution.

The cross-spectral matrix, $\hat{Q}_{nm}$, is computed via the discrete Fourier transform (DFT) using a weighted overlapping (50%) segment averaging (WOSA) technique to reduce estimator variance [see, for example, *Percival and Walden*, 1993]. In each step in the WOSA, a time series block is tapered with a Bartlett

window [*Percival and Walden*, 1993], subjected to the DFT, and averaged with the other blocks. For analyses below we have chosen an ensemble block length, N_b = 128 points, or 64s of 2Hz sampled data. This yields approximately 62 degrees of freedom at each frequency, given a total time series length of 2048 points.

The resulting three-dimensional optical spectrum is reduced to a frequency-direction estimate of the true wave spectrum, S', by weighted integration through k using a first order MTF approximation, Γ (equation 10b),

$$S'(f,\theta) = \int_{k_{\min}}^{k_{\max}} \hat{S}(f,k,\theta) M(f,k) \Gamma(k)\, dk \tag{14}$$

where k_{min} and k_{max} are defined as the wavenumber limits above. An additional weight is imposed to reduce spurious energy outside of the expected concentration of wave energy at the dispersion surface. The dispersion weight, M, is a simple Gaussian hump centered at the linear wave dispersion velocity surface,

$$M(f,k) = \exp\left[\frac{-\left(\frac{f}{k} - \frac{g\tanh(2\pi kh)}{2\pi f}\right)^2}{2\sigma_v}\right] \tag{15}$$

where $\sigma_v = 3\text{ms}^{-1}$ is the standard width of the surface and h is the measured or estimated depth at the array.

2.4.2 Synthetic optical tests

Forward modeling of the radiance reflected to the camera sensor from ocean waves is the most accurate, though processing intensive, way to assess the linearity of the slope-to-radiance transfer function. An extensive set of wave conditions and a subset of lighting conditions are simulated using design frequency-direction spectra composed of joint Gaussian distributions.

$$S(f,\theta) = A\exp\left[\frac{-(\theta-\theta_p)^2}{2\sigma_\theta}\right]\exp\left[\frac{-(f-f_p)^2}{2\sigma_f}\right] + A_n \tag{16}$$

A is the power density amplitude at the peak, θ_p is the wave direction at peak amplitude, σ_θ is the standard directional width, f_p is the peak frequency, σ_f is the standard frequency width, and A_n is the constant background noise amplitude. The relative contribution of background noise is expressed as the noise-to-signal ratio (NSR), equal to the ratio of the total variance of the noise spectrum to the variance of the noiseless wave spectrum. More realistic spectra can be created by cumulative addition of Gaussian distributions to create spectra with sea and swell peaks and bimodal directional spreading.

In the tests described below, sea surface elevation time series of length 1024s, sampled at 2 Hz, were simulated at locations in an alpha array designed for a 5.5s period wave in constant water depth of 5m and used to model radiance at the camera sensor (equation 2) for both clear and overcast skies. Wave spectra of the synthetic optical data were then estimated with the MLE technique and compared to input spectra. For all the synthetic tests the camera is fixed and looking in the direction of the positive x-direction with a tilt of 70° from nadir (20° grazing angle). In the clear sky model, the sun was located at a tilt of 0° from zenith (directly overhead), and for both the clear and overcast sky models radiance magnitudes were normalized to unity, $K_c = K_o = 1$, for ease of computation. Ten realizations were computed for each combination of test parameters, and resulting spectra were averaged to reduce noise. Comparisons of the input spectra with output spectra from modeled visible radiance are quantified using $\rho_{SS'}$, the cross-correlation statistic, defined as

$$\rho_{SS'} = \frac{\sum_{i=1}^{N} (S_i' - \overline{S'})(S_i - \overline{S})}{\left[\sum_{i=1}^{N} (S_i' - \overline{S'})^2 \sum_{i=1}^{N} (S_i - \overline{S})^2 \right]^{1/2}}. \tag{17}$$

where S is the input, or true, spectrum, S' is the estimated spectrum, and N is the number of points in the spectrum. Overbars indicate averages over the total N frequency and directional points modeled. Correlations were also performed for

directional shape at individual frequency bands, $\rho_{SS'}(f)$, in which case N would indicate the number of direction estimates in each band. From here on subscript notation in $\rho_{SS'}$ and $\rho_{SS'}(f)$ is dropped for simplicity.

Initial synthetic tests varied the ratio of total sea-to-swell energy (or SSR, the total energy for sea normalized by the total energy for swell) , and swell peak direction (θ_p) from -60° to 60° by increments of 5°, and with sea and swell directional spreading, σ_θ, fixed at 20° and 5°, respectively. The sea and swell peak frequencies (and widths) are fixed at 0.3 Hz (σ_f = 0.1 Hz) and 0.1 Hz (σ_f = 0.05 Hz), respectively, with the NSR set 0.2. While these tests did not cover the full range of possible conditions, they indicate good agreement of the overall spectral shape, peak direction, and directional spread from synthetic optical data, summarized in Table 1.

Table 2.1 Summary of unimodal synthetic optical data tests, where overbars indicate average values**.**

	f(Hz)	$\overline{\theta_p' - \theta_p}$ (degrees)	rms($\theta_p' - \theta_p$) (degrees)	$\overline{\sigma_\theta' - \sigma_\theta}$ (degrees)	rms($\sigma_\theta' - \sigma_\theta$) (degrees)	$\bar{\rho}$
clear sky model	0.1	0.17	3.5	6.8	9.1	0.80
	0.3	0.22	4.3	-2.1	1.7	0.99
overcast sky model	0.1	0.13	2.9	6.9	8.9	0.80
	0.3	0.28	4.6	-0.7	2.1	0.98

The average directional spectrum correlations versus SSR and peak swell direction, at peak swell and peak frequencies are shown in Figure 2.3. Trends in Figure 2.3a agree with the expected dependence on the wave direction relative to

the camera look direction (i.e. decreased wave visibility dependence seen in equation 7), as correlation in the peak swell band decreases with increased difference between the camera look direction and wave azimuth. However, this is a conservative representation, and this becomes much less important when the component of higher frequency sea-band energy is less (Figure 2.3c), suggesting that the angular dependence (equation 7) can largely be ignored, and that the simple MTF (equation 10) is sufficient to accurately represent the directional shape. Correlation of modeled and estimated directional spread at the peak sea frequency is excellent (average correlation greater than 0.98, Figure 2.3b, d). Differences between estimated and true peak directions at sea and swell are small (average of ~3°; Figure 2.4a, b) and, for swell, increase with the difference between camera look and wave angle directions. Estimated directional widths, σ_θ, are wider than the modeled data for swell (average ~7°; Figure 2.4c), and estimated σ_θ at the peak sea frequency are only slightly narrower than modeled (Figure 2.4d). Overall, the details of spectral estimates in these tests seem to be reasonably invariant to the sky radiance model tested.

The second set of synthetic data was used to test the resolution of two wave trains at the same frequency and different directions. Each wave train was modeled as a Gaussian with f_p = 0.1Hz, σ_f = 0.05 Hz and fixed directional spread σ_θ = 5°, and simulated with a range of directional separation, $\Delta\theta$, from 2° to 120°, centered at normal incidence. The remaining parameter settings were identical to the previous tests. Though the specific parameter space tested was narrow, the results are generalized by normalizing by $2\sigma_\theta$ of the modeled input. The location of the two wave peaks were identified and displayed versus the normalized predicted separation (Figure 2.5). For $\Delta\theta$ less than $4\sigma_\theta$ ($\Delta\theta/2\sigma_\theta = 2$) only one wave peak location was effectively found. For $\Delta\theta > 4\sigma_\theta$ the locations of the directional peaks became identifiable, and became increasingly accurate as $\Delta\theta$ increased.

2.5 Comparisons with *in situ* spectra at NCEX

Ground truth data for method testing came from the multi-investigator Nearshore Canyon Experiment (NCEX) that took place in 2003 at Blacks Beach in California. The NCEX bathymetry was complex, including steep walled submarine canyons just offshore and a curving shoreline that caused complicated wave refraction patterns. These in turn drove interesting and likewise complex nearshore circulation [*Long and Özkan-Haller*, 2005].

Data taken on October 31, from six locations in the study area, were used to ground truth the optical wave spectral technique (Figure 2.6). *In situ* instruments were deployed in water depths from 4m to 6m outside of the surf zone [*Thomson et al.*, in press]. Instrument orientations were generally known only to within five degree due to the accuracy of the internal reference compass (Jim Thomson, personal communication, 2007). MLE frequency-directional spectra were estimated from the *in situ* measurements of pressure and bi-directional horizontal velocity (PUV), or three-component velocity (UVW, only at y = -625m) time series using the DIWASP toolbox [*Johnson*, 2002] in Matlab ®. Spectral directions were given relative to instrument orientation and were rotated to the local Argus reference frame, with the negative y-axis (alongshore) direction approximately 19° west of true north and the positive x-axis pointing offshore.

Optical data at Blacks Beach were collected from computer-controlled digital Argus video cameras and human-controlled Naval Research Laboratory cameras at the Scripps Institute of Oceanography, located on top of the NOAA Fisheries building. These cameras are part of the Argus network, a system of automated nearshore imaging stations with long-term sampling capability, used to quantify nearshore geophysical states and processes (e.g. bathymetry, morphodynamics, and nearshore currents) [see *Aarninkhof and Holman*, 1999; *Holman and Stanley*, 2007]. Two cameras with overlapping views were used, one pointing north and one quartering to the north-west, with sensor dimensions of 1280x960 and 1024x768 pixels, and horizontal fields of view of 36° and 39°,

respectively. Time series of intensity were collected from alpha arrays centered on the *in situ* instrument locations, with the exception of the most southern location (*in situ* instrument location y = -625) where optical collections were located roughly 80m offshore of the *in situ* instrument location (Figure 2.6) due to the limited field of view of the camera. The aperture of each array, documented in Table 2, was sized according to the mean depth at the location. Actual locations of the elements of each array are limited to unit pixel locations, resulting in Alpha arrays with O(m) differences in locations of each element from ideal. However the final real-world locations of elements were known and used in the analysis, so deviations should not introduce error in the resulting spectra, as suggested in Appendix A. Seventeen minute (1024s) time series, coincident with *in situ* time series, were processed according the optical wave spectrum algorithm of section 3.

Table 2.2 Instrument locations, orientations and alpha array properties for the groundtruth experiments.

in situ instrument location		alpha array center location		mean water depth (m)	alpha array orientation (deg. CCW from pos. x-axis)	mean alpha array dimensions		camera resolution (m/pixel)	
x (m)	y (m)	x (m)	y (m)			l_x (m)	l_y (m)	cross-range	along-range
766	-1693	769	-1699	5.8	34.9	36.4	72.7	0.7	12.6
498	-1335	498	-1337	5.9	22.1	36.4	72.8	0.5	5.8
398	-1215	399	-1219	4.1	21.6	30.9	61.8	0.4	4.0
443	-1195	443	-1198	5.9	21.6	36.5	73.0	0.3	4.1
334	-1043	334	-1044	5.9	31.8	36.5	72.9	0.3	2.4
186	-625	261	-653	4.5	0	32.4	64.7	0.1	0.3

Examples of *in situ* and optical wave spectra are shown in Figure 2.7 and demonstrate both the similarity between both estimates and the simultaneous complexity of the wave field. Basic agreement of the frequency spectral distribution, $S(f)$, between *in situ* and optically-derived wave spectra are assessed by simple cross-correlation, as in (17). Directional agreement between *in situ* and optically derived spectra are characterized by comparisons of the mean peak direction and mean directional spread within two frequency bands, a swell band ($0.05\text{Hz} \leq f \leq 0.125\text{Hz}$) and a sea band ($0.125\text{Hz} < f \leq 0.3\text{Hz}$). The ratio of the total energy between the sea and swell bands, SSR, is also compared.

The single peak frequency observed from the optical and PUV spectra (Figure 2.8) varied between the swell and sea peak frequencies, roughly 0.1Hz and 0.175Hz respectively, for both the PUV and optical spectra at all locations. The average peak frequency from the PUV and optical spectra are 0.123 Hz and 0.125 Hz, respectively. Correlations with frequency spectra, $S(f)$ (Figure 2.9), show good agreement between PUV and optical estimates, with an the average correlation (ρ) of 0.88 of the 96 test spectra. Figure 2.9 also shows increased correlation with increasing distance from the camera locations (located approximately at y = -540m), and that the variability, in general, (standard deviation plotted in Figure 2.9) decreases with increasing distance from the camera. It is likely that the increased pixel footprint far from the camera effectively averages out high frequency waves with shorter wavelengths that preferentially contaminate optical spectra.

Directional statistics, including the peak direction, θ_p and directional spreading, σ_θ, were estimated by fitting to a directional distribution model of a Gaussian hump with an offset,

$$S(\theta) = A\exp\left[\frac{-(\theta-\theta_p)^2}{2\sigma_\theta}\right] + B \qquad (18)$$

where A is the peak spectral amplitude and B a noise floor offset. The model is fit to each frequency band for both the *in situ* and optical spectra using a nonlinear

least-squares fitting algorithm [*Marquardt*, 1963]. Model skill, r, and 95% confidence limits on the parameters were calculated and used to exclude poor estimates of θ_p and σ_θ by excluding points with confidence limits larger than ±10° or $r < 0.9$ (79 of 96 spectra, 82%, passed these criteria). The fitted peak direction and spread were compared at the peak frequency, as defined by the PUV spectra. Figure 2.10 shows good agreement between both spectral estimation techniques, with 6.4° root-mean-square (RMS) difference for the peak direction at the peak PUV frequency for a total of 79 observations. There is no clear systematic bias in the average difference between PUV and optical peak directions (Figure 2.11a) with alongshore distance (i.e. pixel resolution), and mean results are consistent with random alignment error of a few degrees between the *in situ* and optical instruments. Likewise, the standard deviation difference between PUV and optical peak directions (Figure 2.11b) has no clear trend with alongshore position, and the total standard deviation difference (5°) is comparable to the expected accuracy of the PUV direction estimation. Finally, optical directional spread estimates (Figure 2.12) at the peak frequency are almost always smaller than PUV directional widths, by an average of 12° (full standard width), which is in agreement with the expectation of wider directional spread estimates from PUV directional spectra.

Steep bathymetric gradients of the Scripps Canyon, at the southern end of the NCEX study site [*Munk and Traylor*, 1947; *Long and Özkan-Haller*, 2005], are expected to cause strong refraction of the incident wave field and result in potentially complex spectra. Furthermore, waves are shadowed by the offshore Channel Islands and diffracted at their boundaries [*Emery*, 1958; *Pawka*, 1982; *Pawka*, 1983]. Examples of optical wave spectra (Figure 2.13) inshore of the canyon show bimodal directional distributions. The time series of wave angle distribution at $f = 0.14$Hz show the development of the directional separations over the day, with a spread between peaks of roughly 15°. At times, the spectra do not show two clear peaks, but instead show a broad flat distribution or a dominant peak and a flat step suggesting a minor peak. In contrast, the *in situ* spectra do not

resolve the bimodal distributions, and effectively have narrower directional spread than the corresponding optical spectra. This last observation is confirmed in Figure 2.12, where the directional spread is wider for the optical spectra at y = -625m. The observation of two closely spaced directional peaks at frequencies shown here is consistent with spectra measured in deeper water by *Pawka* [1983] at nearby Torrey Pines Beach, corresponding to the shadow from San Clemente Island. Again, the lack of similar closely spaced directional peaks in the PUV data is expected due to the inherent coarse resolution of these spectra [*Oltman-Shay and Guza*, 1984], and may account for the larger directional spreading observed in optical spectra.

2.6 Discussion

Lighting conditions, residual foam and wave breaking, and optical sampling errors can all contribute to possible error in optical wave spectral estimation. Each of these is discussed in turn.

2.6.1 Effects of lighting conditions and intermittent breaking

The radiance model for the technique assumes slow variability in the sky dome radiance. In the synthetic tests, both the clear sky model and the uniformly overcast models produced satisfactory results, using only a simple modulation transfer function. However, under natural conditions, nonlinearities can be introduced in several ways. Non-monotonic sky radiance, particularly due to patchy or broken clouds with sharp gradients, will presumably result in a nonlinear MTF. At the extreme, sky dome radiance in the vicinity of the solar disk can be approximated by a delta function, and the reflected signals from this region, commonly referred to as sun glitter, will be highly nonlinear with sea surface slope. It would be feasible to measure the actual sky dome radiance with a wide-angle zenith-pointed camera and invert images of observed intensities for two-dimensional sea surface slope, but the process would be complicated, computer-intensive and likely not unique. Fortunately, the ground truth tests showed

satisfactory results even where the lighting conditions changed throughout the day from overcast to partially cloudy to clear. Furthermore, it is evident that the exclusion of the angular dependence, or $\cos(\alpha_n - \alpha_c)$, (equation 7) into the MTF was reasonable. This is highlighted by the observation that most of the wave directions observed were propagating at right angles to the camera look direction (see Figure 3.6), precisely where predictions based on (7) would force spectral wave energy at to zero.

Wave breaking, white capping and advected residual foam are also not accounted for in the MTF, complicating the analysis for locations inside the surf zone or for higher wind conditions where offshore breaking, foam and white capping are not negligible. However, wave breaking outside of the surf zone will by definition be intermittent, with effective periods much longer than the incident swell band. Similarly, residual foam, left after the passage of a breaker, is also a low-frequency phenomenon, contributing little to the incident frequencies used in this analysis. Thus contamination due to infrequent wave breaking and residual foam is mitigated in the technique by the combination of inverse wavenumber-squared weighting and the masking of energy outside of the expected dispersion surface (equation 14).

Note that this masking requires a rough estimate of the water depth in the vicinity of the array. Climatological information of adequate accuracy is usually available. Alternately, depths can be estimated from *f-k* slices of the three-dimensional optical spectra, making the technique totally standalone [*Stockdon and Holman*, 2000; *Dugan et al.*, 2001b].

2.6.2 Video sampling properties

Uncertainties in photogrammetry and limitations in video sampling resolution can contribute to bias or error in optical wave spectra. Errors in photogrammetry (usually due to errors in estimates of the pointing angles of the camera or due to poor knowledge of lens distortion) can transfer into error of the

calculated real world positions of alpha array elements. Careful testing shows that, for almost all cases, these errors will cause an image shift that is locally near uniform and consists of no more than a few pixels. Thus, these errors yield negligible errors in estimated spectra.

Finite amplitude misregistration is a more difficult problem to deal with. In mapping from the real-world location of each pixel within an alpha array to its corresponding image coordinates, it has been assumed that the vertical location can be approximated by mean sea level. For a wavy sea in which the sea surface elevation differs from this level by a time-varying amount, η, the horizontal position will be in error by $\Delta R = \eta \frac{R}{z_c}$, where z_c is the elevation difference and R is the horizontal range between the real-world pixel location and the camera. $\frac{R}{z_c}$ values are typically up to 10, so a 1.0m height wave will have radial position errors up to ±5m, with crest samples closer to the camera and troughs further away than the design pixel location. Thus, a sinusoidal wave form $\eta = a\cos(kx - \sigma t)$ propagating in the negative x-direction (shoreward) will be sampled not at the intended x position, x_0, but approximately at position $x_0 - \eta \frac{R}{z_c}\cos\psi = x_0 - \frac{aR}{z_c}\cos\psi\cos(kx_0 - \sigma t)$, where ψ is the horizontal camera view angle relative to the positive x-axis. The magnitude of the time-varying phase shift introduced is just $ak\frac{R}{z_c}\cos\psi$. Except at extreme ranges or for very steep seas, values are usually considerably less than ±one radian and yield an asymmetry in the observed wave form.

2.6.3 Application in nearshore research

Though optical and *in situ* spectral shape agree well for the test cases above, the lack of a scaled MTF limits this optical technique to estimating spectral shape

only. However, there are several possibilities for estimating correctly-scaled sea-surface elevation spectra directly from optical data. Assuming radiance transmitted from below the water surface is negligible, calibrated cameras would be used to collect data of both the reflected radiance from the wavy sea surface and the simultaneous sky radiance distribution. This would allow an accurate sky downwelling radiance to be modeled, or for the case of a non-linear sky-radiance distribution it could be measured directly. In turn, absolute spectra (with physical units) could be calculated without any *in situ* sampling, but this may be prohibitive in calculation effort and therefore difficult in practice. Alternately, a simpler sampling scheme consisting of a sparse array of *in situ* instruments, such as pressure sensors, could be used to calibrate magnitudes over an extended and dense array of optical Alpha instruments, thus spanning a region of interest too broad to be sufficiently and easily sampled by *in situ* measurements alone. Finally, wave height has been estimated optically from measurements of the depth of initial wave breaking at the outer edge of the surf zone. This method requires knowledge of water depth at breaking (also observable using optics) and the wave height to depth ratio of breaking waves [*Holland et al.*, 2002].

This optical wave spectrum technique can provide important contributions to nearshore research due to its combined assets of dense and broad temporal and spatial sampling and simple, efficient computation methods. It is expected to be used primarily as a scientific discovery tool for examining wave spectral transformation in the nearshore over widely varying beach bathymetry and wave energy conditions. For example, in a forthcoming paper the authors will compare the evolution of the observed directional wave field with wave model predictions for data collected over the complex canyon bathymetry of the Nearshore Canyon Experiment. In general, observed spectra will be needed for initiating nearshore circulation and sediment transport models on any large domains. Finally, optical wave spectra have been used to estimate water depth and mean currents using inversion of the wave dispersion surface [*Dugan et al.*, 2001b].

2.7 Conclusions

A method for the estimation of wave directional spectral shape from optical measurements from a sparse array of pixels has been developed and tested. Based on maximum likelihood spectra analysis of the cross-spectral matrix from a 17-element 2D wave measurement array (Alpha array), the method was proven to provide simple and reliable estimations of nearshore wave spectral shape for outside of the surf zone. The technique was tested with synthetic experiments to examine its theoretical resolution for ocean wave spectra. Realistic synthetic tests were conducted with complex unimodal and bimodal directional spectra, with high (sea) and low (swell) frequency components, and with an overcast and clear sky radiance model. The tests show accurate estimation of the true directional shape at sea and swell frequencies with average spectral shape correlations greater than 0.98 and 0.8, respectively. Peak directions at swell and sea frequencies were accurately predicted with small RMS error (approximately 3.2° and 4.5°, respectively). Tests with bimodal directional distributions show the optical technique can resolve both wave directional peaks provided the spread between the peaks is roughly twice the width of either peak. Results were mostly independent of the optical sky dome radiance model used.

Ground truth tests comparing *in situ* (PUV) and optical data measured during the 2003 Nearshore Canyon Experiment show good agreement. Correlations of the frequency spectra were high (mean correlation of 0.88 for all 96 spectra), and average peak frequencies agreed well with a difference of only 0.002 Hz between *in situ* and optical spectra. The peak optical and PUV wave directions, at peak frequency bands, showed close agreement with a standard deviation of only 5°. Directional widths for PUV spectra were 52% wider that optical spectra (mean difference of 12° full standard width), suggesting fine resolution of directional spectra is achievable with the optical technique. Finally, examples of bimodal direction spectra (with peak separations of ~15°) near the Scripps Canyon, at the southern end of the NCEX study site, were resolved easily in the optically derived

spectra and not in the PUV derived spectra. The bimodal spectra are consistent with wave shadowing of offshore islands as shown in previous studies.

Though this technique is limited to estimating spectral shape only, simple additions in the future will allow absolute spectral densities and estimates of sea-surface elevation. Even so, the technique is expected to be very useful for basic research on wave field evolution over complex bathymetry, wave model validation and model initiation for nearshore circulation and sediment transport.

2.8 References

Aarninkhof, S., and R. A. Holman (1999), Monitoring the nearshore with video, *Backscatter*, *10*(2), 8-11.

Capon, J. (1969), High-resolution frequency-wavenumber spectrum analysis, *Proceedings of the IEEE*, *57*1408-1418.

Capon, J., R. J. Greenfield, and R. J. Kolker (1967), Multidimensional maximum-likelihood processing of a large apeture seismic array, *Proceedings of the IEEE*, *55*192-211.

Chapman, R. D. (1981), Visibility of rms slope variations on the sea surface, *Applied Optics*, *21*(11), 1959-1966.

Chapman, R. D., and G. B. Irani (1981), Errors in estimating slope spectra from wave images, *Applied Optics*, *20*(20), 3645-3652.

Cox, C., and W. Munk (1954), The measurement of the roughness of the sea surface from photographs of the sun's glitter, *Journal of the Optical Society of America*, *44*838-850.

Davis, R. E., and L. A. Regier (1977), Methods for estimating directional wave spectra from multi-element arrays, *J. Mar. Res.*, *5*(3), 453-477.

Dugan, J. P., G. J. Fetzer, J. Bowden, G. J. Farruggia, J. Z. Williams, C. C. Piotrowski, K. Vierra, D. Campion, and D. N. Sitter (2001a), Airborne optical system for remote sensing of ocean waves, *J. Atm. Ocean. Tech.*, *18*(7), 1267-1276.

Dugan, J. P., C. C. Piotrowski, and J. Z. Williams (2001b), Water depth and surface current retrevials from airborne optical measurements of surface gravity wave dispersion, *J. Geophys. Res.*, *106*(C8), 16903-16915.

Emery, K. O. (1958), Wave patterns off Southern California, *J. Mar. Res.*, *17*133-140.

Freilich, M. H., R. T. Guza, and S. L. Elgar (1990), Observations of nonlinear effects in directional spectra of shoaling gravity waves, *J. Geophys. Res.*, *95*(C6), 9,645-649,656.

Gotwols, B. L., and G. B. Irani (1980), Optical determination of the phase velocity of short gravity waves, *J. Geophys. Res.*, *85*(C7), 3964-3970.

Gotwols, B. L., and G. B. Irani (1982), Charged-coupled device camera system for remotely measuring the dynamics of ocean waves, *Applied Optics*, *21*(5), 851-860.

Holland, K. T., R. A. Holman, T. C. Lippmann, J. Stanley, and N. Plant (1997), Practical use of video imagery in nearshore oceanographic field studies, *IEEE Journal of Ocean Engineering*, *22*(1).

Holland, K. T., J. A. Puleo, N. G. Plant, and J. M. Kaihatu (2002), Littoral Environmental Nowcasting System (LENS), paper presented at IEEE Oceans Conference.

Holman, R. A., and J. Stanley (2007), The history and technical capabilities of Argus, *Coastal Eng.*, *54*(6-7), 477-491.

Hopkinson, R. G. (1954), Measurements of sky luminance distribution at Stockholm, *Journal of the Optical Society of America*, *44*(6), 455-459.

Johnson, D. (2002), DIWASP, a directional wave spectra toolbox for MATLAB®: User Manual, Center for Water Research, University of Western Australia.

Kasevich, R. S. (1975), Directional wave spectra from daylight scattereing, *J. Geophys. Res.*, *80*(33), 4535-4541.

Long, J. W., and H. T. Özkan-Haller (2005), Offshore controls on nearshore rip currents, *J. Geophys. Res.*, *110*(C12007).

Longuet-Higgins, M. S., D. E. Cartwright, and N. D. Smith (1963), Observations of the directional spectrum of sea waves using the motions of a floating buoy, paper presented at Proceedings of the Conference of Ocean Wave Spectra, Prentice Hall.

Lubard, S. C., J. E. Krimmel, L. R. Thebaud, D. D. Evans, and O. H. Shemdin (1980), Optical image and laser slope meter intercomparisons of high frequency waves, *J. Geophys. Res.*, *85*(c9), 4996-5002.

Marquardt, D. W. (1963), An Algorithm for Least-Squares Estimation of Nonlinear Parameters, *Journal of the Society for Industrial and Applied Math*, *11*(2), 431-441.

Monaldo, F. M., and R. S. Kasevich (1981a), Daylight imagery of ocean surfce waves for wave spectra, *J. Phys. Oceanogr.*, *11*272-283.

Monaldo, F. M., and R. S. Kasevich (1981b), Measurement of short-wave modulation using fine time-series optical spectra, *J. Phys. Oceanogr.*, *11*1034-1036.

Moon, P., and D. E. Spencer (1942), Illumination from a non-uniform sky, *Trans. Illum. Eng. Soc. (NY)*, *37*707–726.

Munk, W. H., and M. A. Traylor (1947), Refraction of ocean waves: a process linking underwater topography to beach erosion, *J. Geol.*, *55*1-26.

Oltman-Shay, J. M., and R. T. Guza (1984), A data-adaptive ocean wave directional-spectrum estimator for pitch and roll type measurements, *J. Phys. Oceanogr.*, *14*1800-1810.

Pawka, S. (1982), Wave directional characteristics on a partially sheltered coast, Ph.D. dissertation, Scripps Inst. of Oceanography, University of California, San Diego.

Pawka, S. (1983), Island shadows in wave directional spectra, *J. Geophys. Res.*, *88*(C4), 2579-2591.

Percival, D. B., and A. T. Walden (1993), *Spectral analysis for physical applications: multitaper and conventional univariate techniques*, 583 pp., Cambridge University Press, New York.

Regier, L. A., and R. E. Davis (1977), Observations of the power and directional spectrum of ocean waves, *J. Mar. Res.*, *35*(3), 433–452.

Stilwell, D. (1969), Directional energy spectra of the sea from photographs, *J. Geophys. Res.*, *74*(8), 1974-1986.

Stilwell, D., and R. O. Pilon (1974), Directional spectra of surface waves from photographs, *J. Geophys. Res.*, *79*(9), 1277-1284.

Stockdon, H. F., and R. A. Holman (2000), Estimation of wave phase speed and nearshore bathymetry from video imagery, *J. Geophys. Res.*, *105*(C9), 22,015-022,033.

Thomson, J., S. Elgar, T. H. C. Herbers, and B. Raubenheimer (in press), Refraction and reflection on infragravity waves near submarine canyons, *J. Geophys. Res.*

Walker, R. E. (1994), *Marine light field statistics*, 675 pp., John Wiley and Sons, Inc., New York.

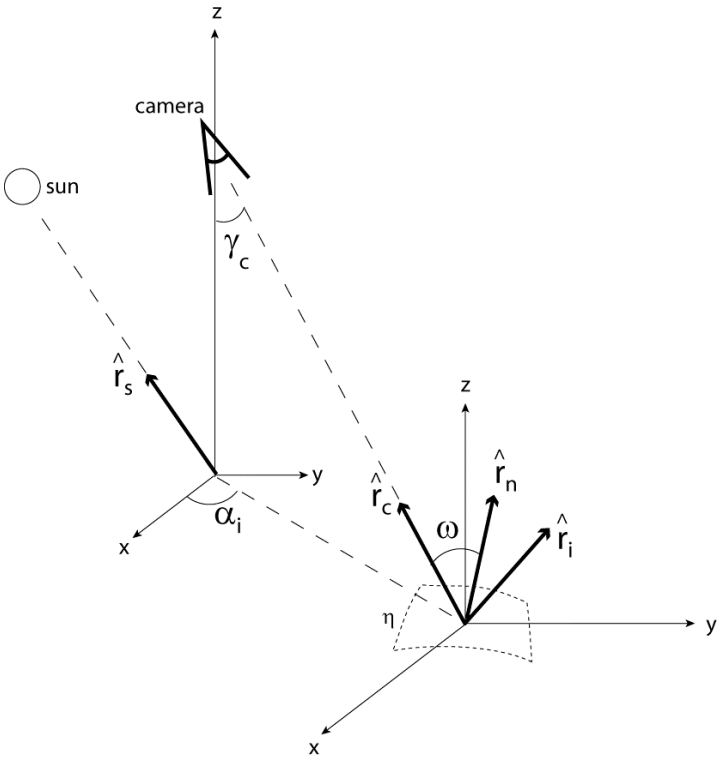

Figure 2.1 Schematic of the viewing geometry. Reflected radiance from the sea surface η, after Chapman [1981], including camera, surface normal, incident and sun unit vectors are shown (subscripts c, n, i and s, respectively). Only the camera azimuth, αi, and nadir tilt, γi, angles are shown for clarity. See section 2.2.1 for definitions of all other labels and symbols.

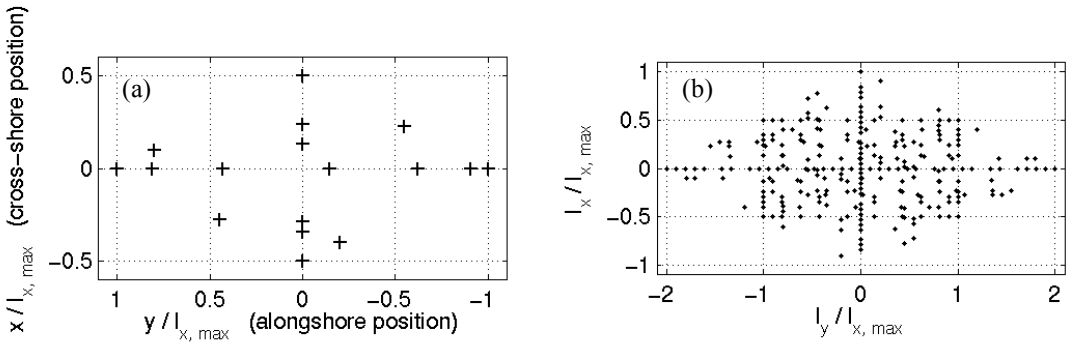

Figure 2.2 (a) Alpha locations normalized by the maximum cross-shore array dimension, l_x. (b) The "co-array" of the array in panel (a), normalized by l_x.

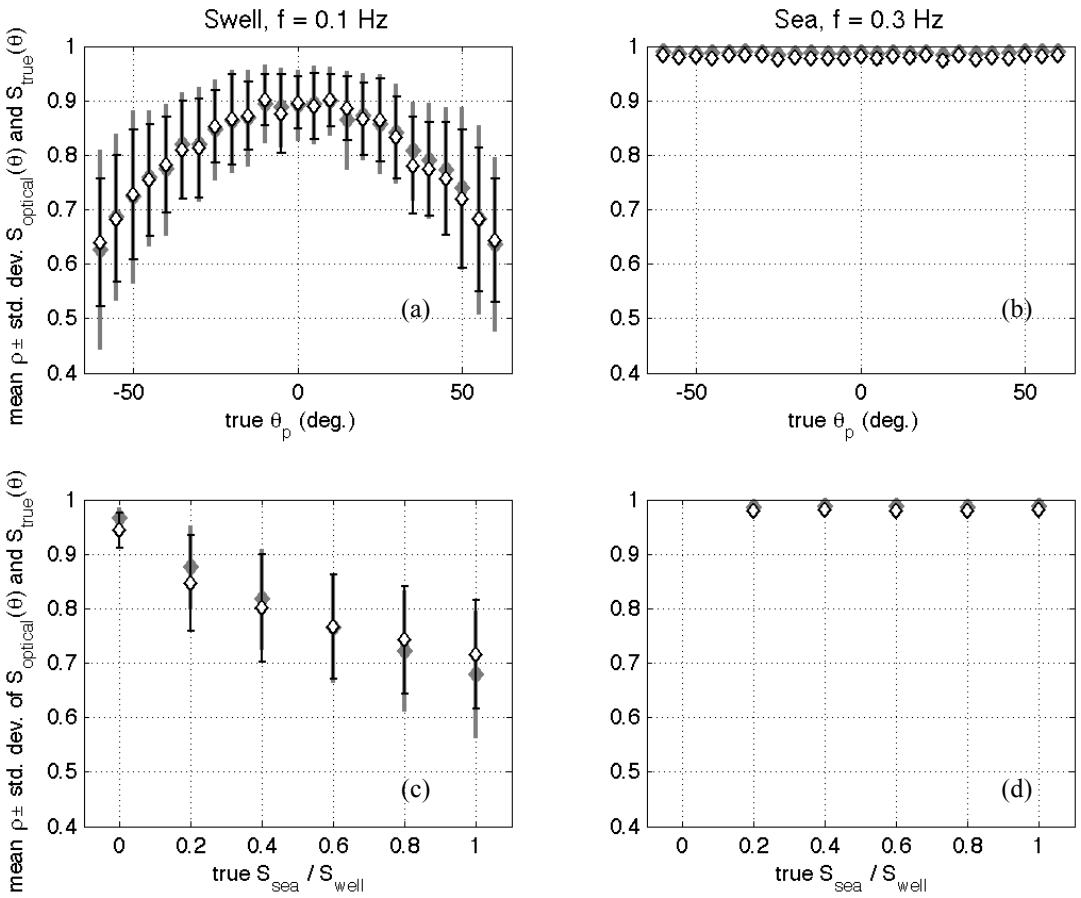

Figure 2.3 (a) Average directional spectra correlation, ρ, between optical and modeled wave spectra, measured at the frequency band $f = 0.1$ Hz, plotted versus change in the modeled peak direction at $f = 0.1$ Hz. Vertical bars show standard deviation for all tests (over all SSR). (c) Average directional spectra correlation, ρ, at $f = 0.1$ Hz versus varying SSR. Panels (b) and (d) show results for the same tests for $f = 0.3$ Hz. For all panels open symbols indicate tests using the overcast sky model, and filled gray symbols indicate tests with the clear sky model.

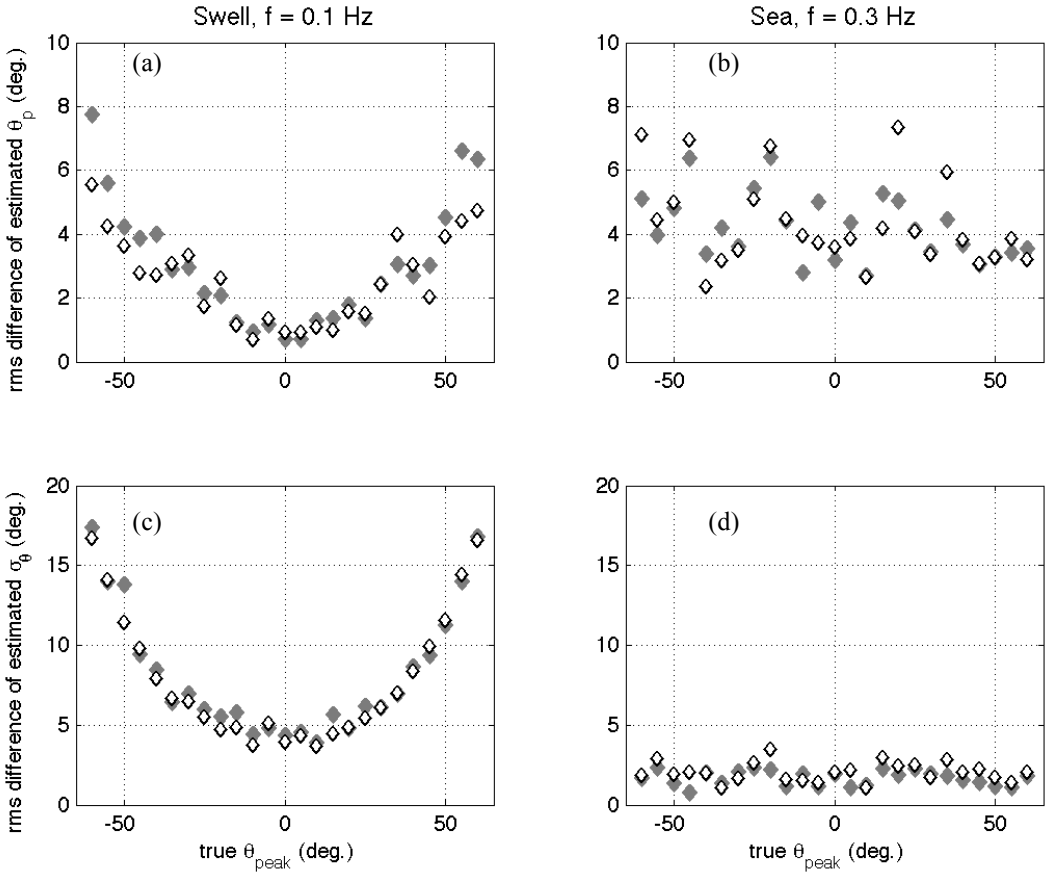

Figure 2.4 (a) RMS difference of optically estimated and true (modeled) peak direction, θ_p, at $f = 0.1$ Hz w.r.t modeled swell direction. (c) RMS difference of optically estimated and true (modeled) direction width, σ_θ, at $f = 0.1$ Hz w.r.t modeled swell direction. Panels (b) and (d) show the same test results for $f = 0.3$ Hz. For both panels filled symbols indicate tests with the clear sky model and open symbols indicate the overcast sky model tests.

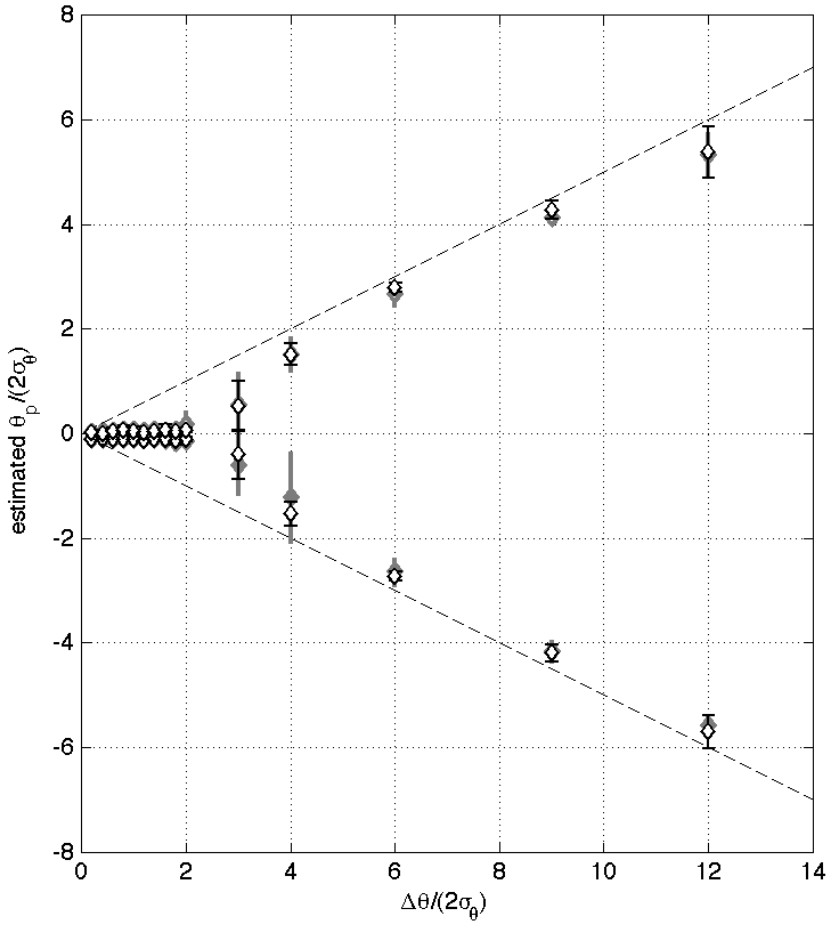

Figure 2.5 Average and standard deviation of identified directional peaks of synthetic bimodal spectra at $f = 0.1$ Hz versus modeled separation, $\Delta\theta$. Angles have been normalized by the total modeled directional width, $2\sigma_\theta$. The dashed line indicates theoretical perfect agreement.

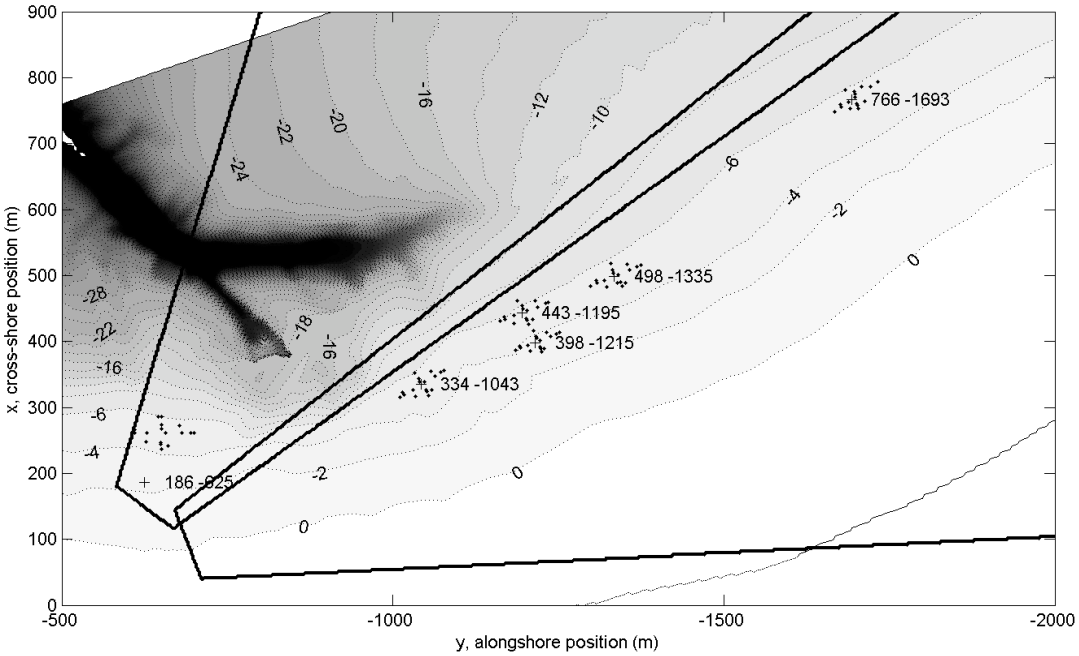

Figure 2.6 Map of the location of in situ PUV instrument positions (+), corresponding alpha arrays (·) plotted on a bathymetry contour map of the southern portion of the NCEX site. Thick lines show the fields of view of the two cameras used to record optical data for the ground truth analysis (section 4). Depths are relative to NGVD.

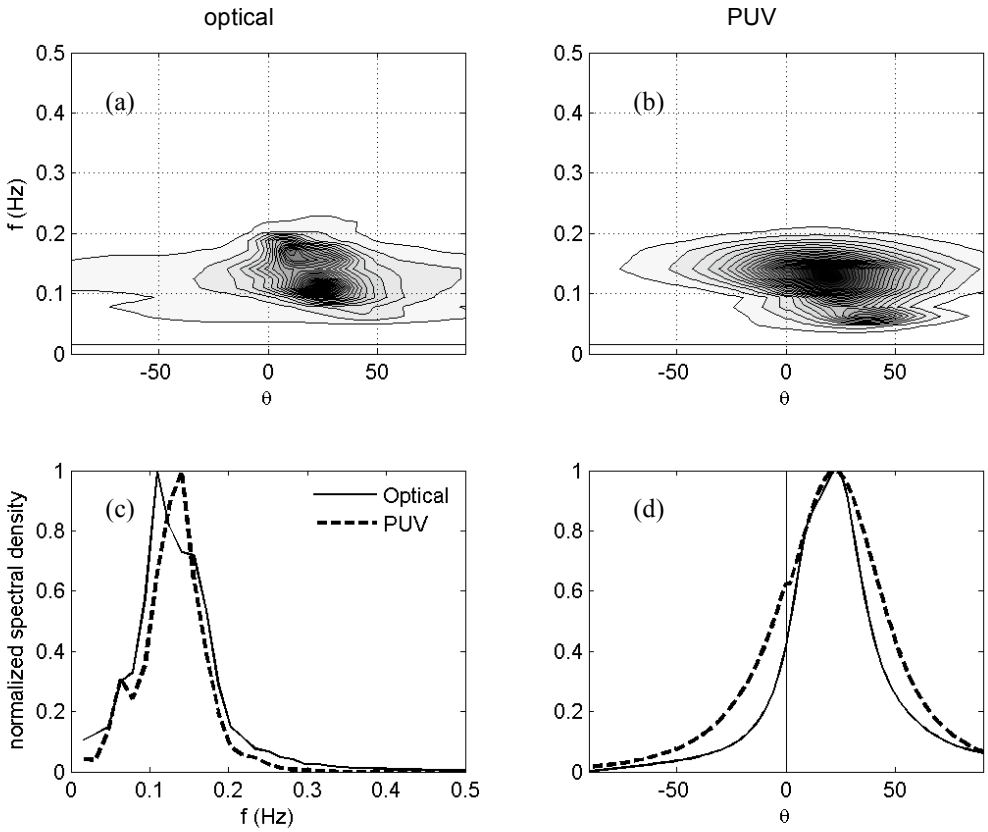

Figure 2.7 (a) Examples of optical and (b) in situ (PUV) spectra from 31 October, 0900 PST. Spectral densities have been normalized by peak values. (c) The integrated frequency and (d) directional distributions of spectral density are similar between both spectral estimates, including similar peak directions and frequencies. Quantitative comparisons between both estimates are detailed in section 4.

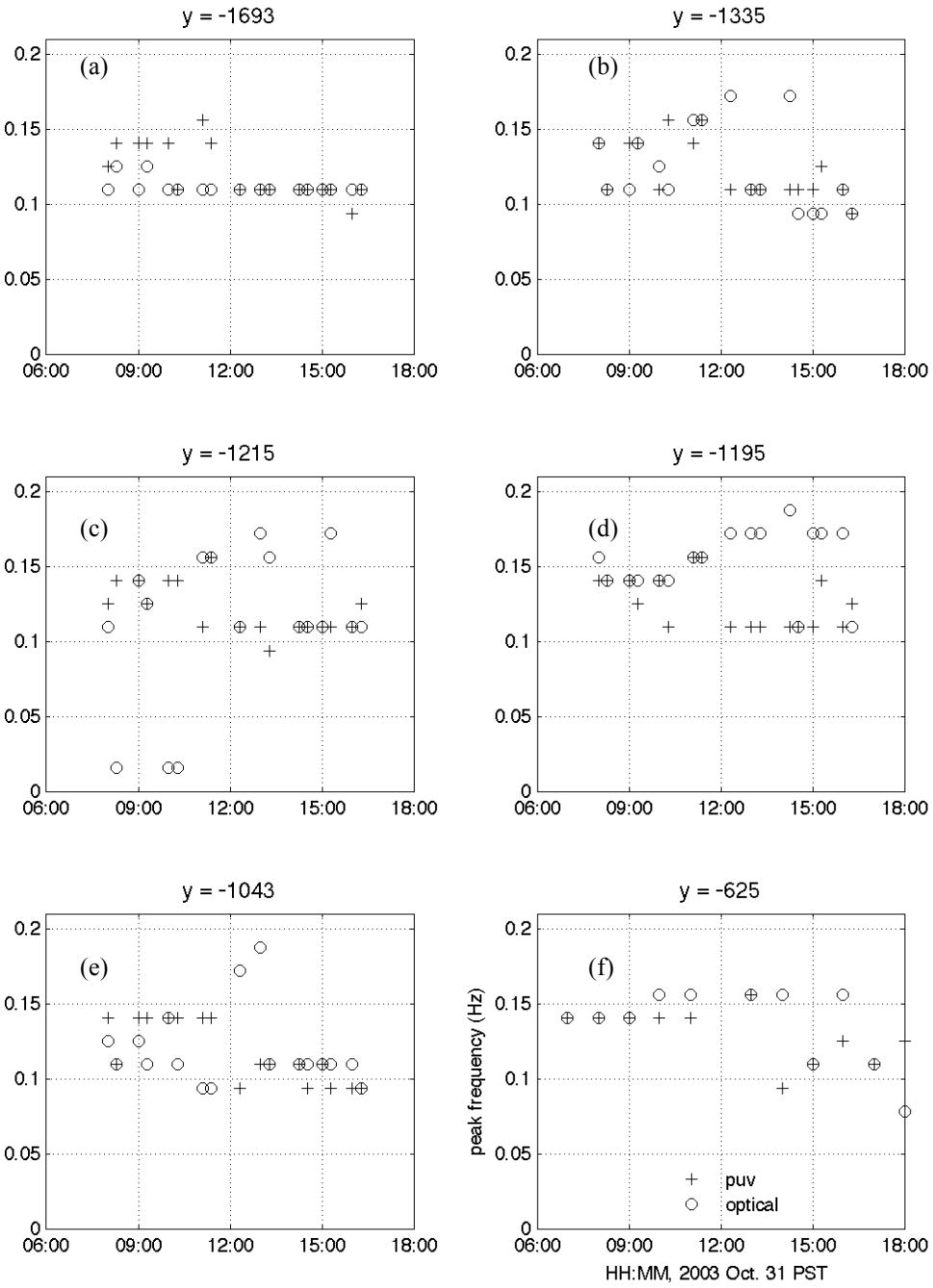

Figure 2.8. (a-f) Time series of the single peak frequency from the optical (o) and in situ (PUV) spectra (+) at each instrument. Alongshore position is indicated above each panel. Note the development of bimodal spectra after 0900 PST in most panels. The mean peak frequency from all PUV spectra is 0.123 Hz versus a mean of 0.125 Hz from the optical spectra.

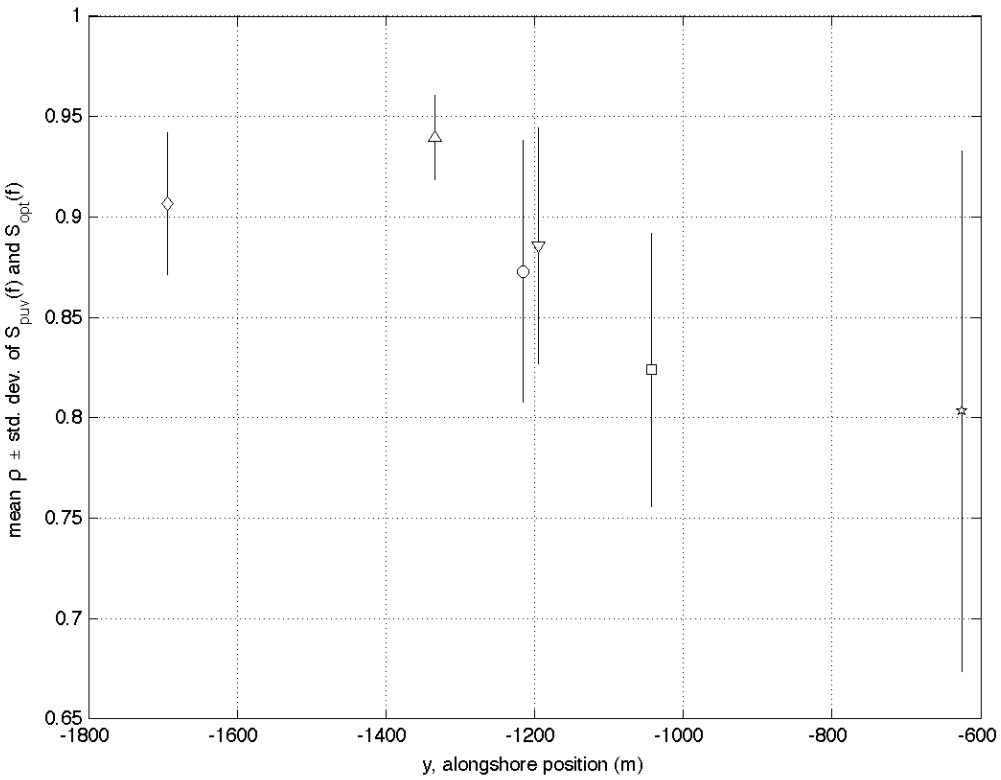

Figure 2.9 The average correlation (± one standard deviation) of the PUV and optical frequency spectra plotted versus alongshore position.

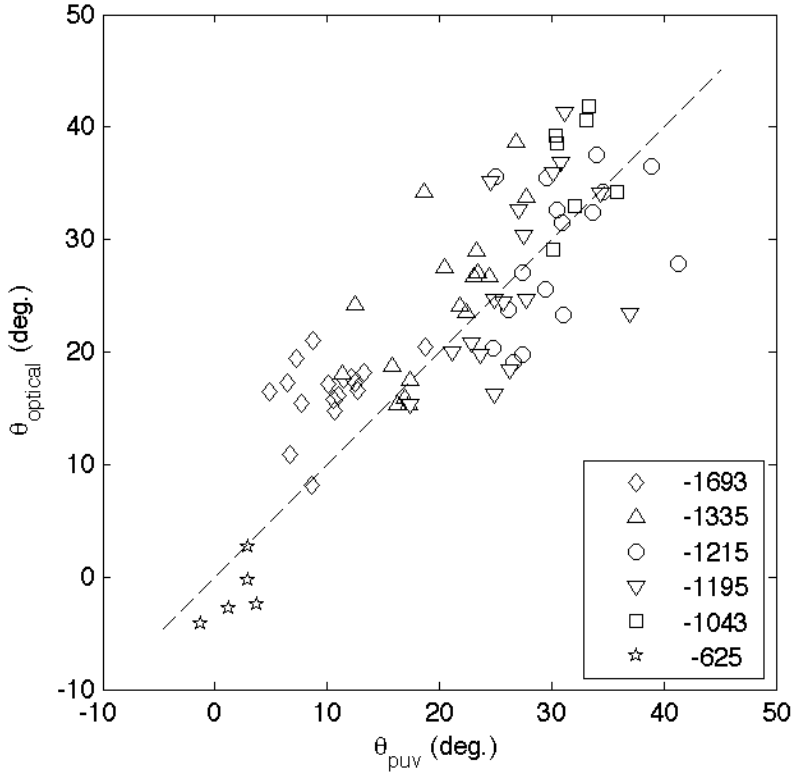

Figure 2.10 In situ (PUV) versus optical peak direction, θ_p, taken from the peak frequency in the PUV spectra. The theoretical one-to-one agreement is shown (dashed line). The RMS difference of the peak directions between both techniques is 6.4°.

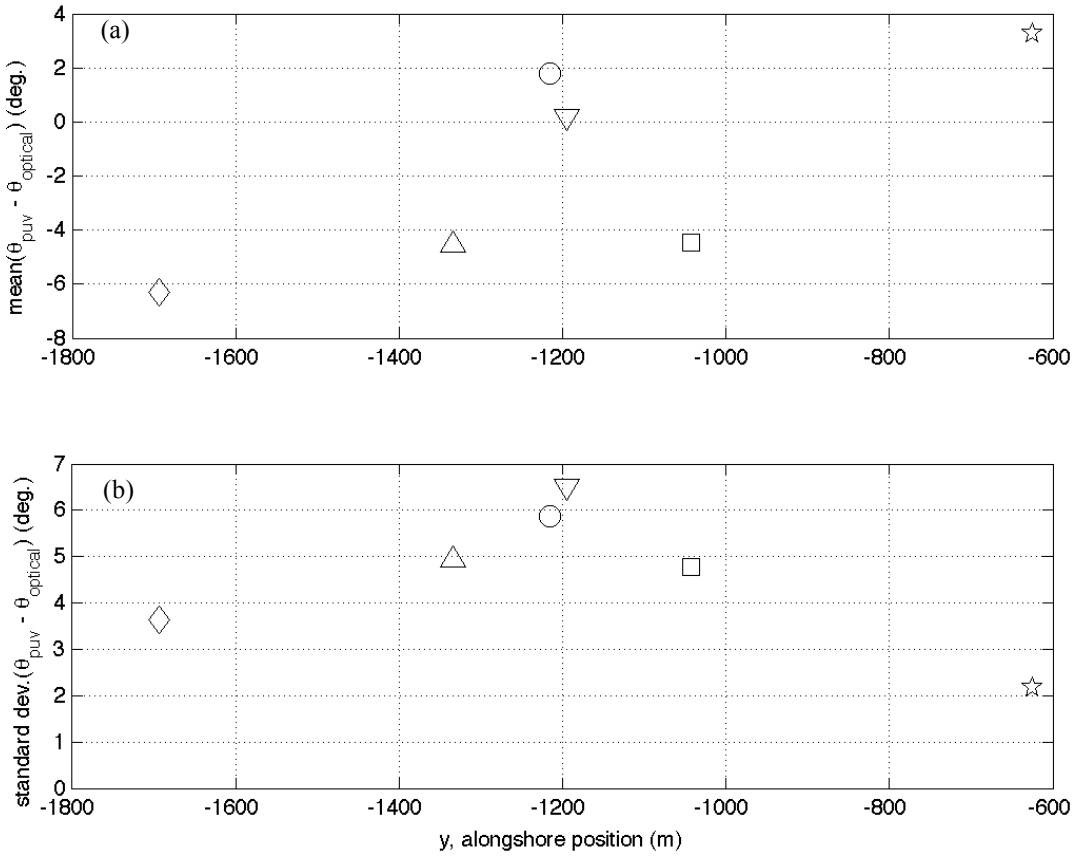

Figure 2.11 (a) Mean difference between peak PUV and optical wave directions measured at the peak PUV frequency. (b) Standard deviation of the difference between peak PUV and optical wave directions. The average standard deviation of the differences among all the instruments is 5°.

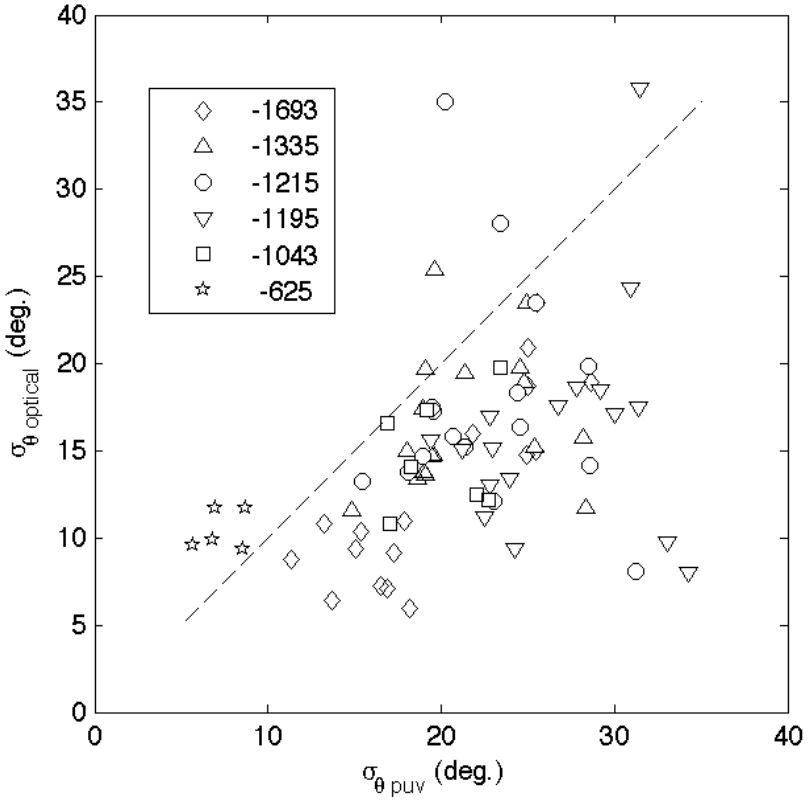

Figure 2.12 Optical and in situ (PUV) estimated mean half-standard width, σ_θ. The dashed line indicates theoretical one-to-one agreement. Points below the line indicate PUV directional spread wider than optical. Optical widths were on average 6° (or 12° full standard width) narrower than PUV spectra. Note the increased directional width of the optical estimates from y = -625m (stars) compared with the PUV spectra.

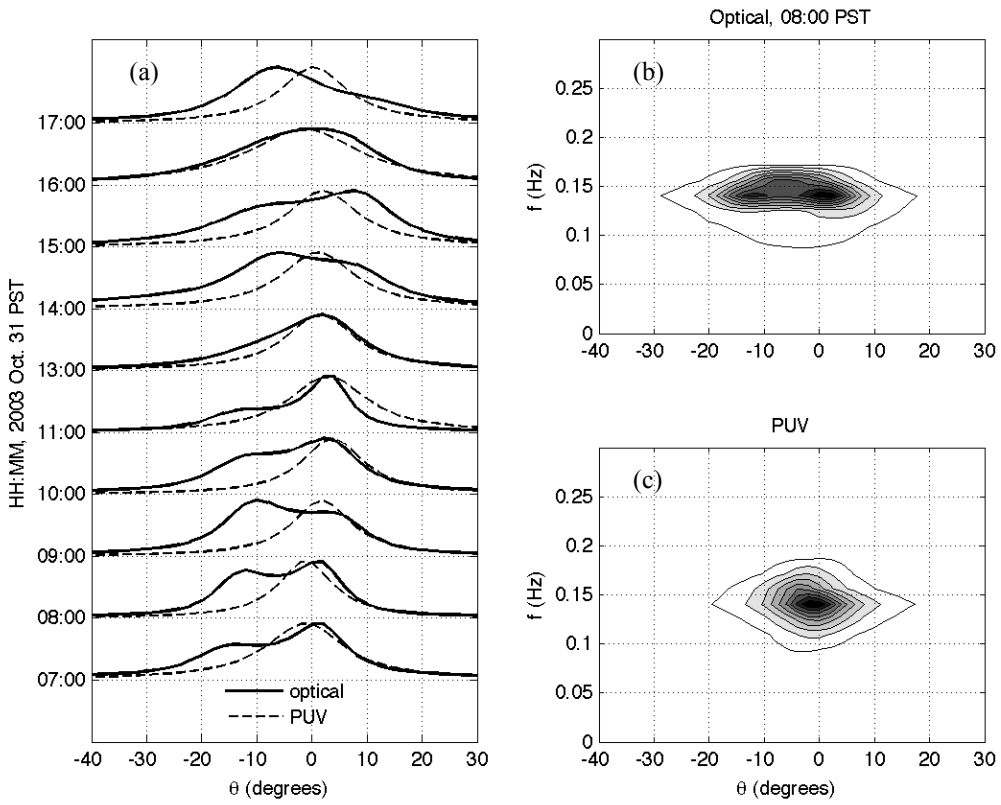

Figure 2.13 (a) Time series of directional distribution from a single frequency band (f = 0.14Hz) from optical (solid) and PUV (dashed) taken from the instrument at y = -625m. All spectral densities have been normalized by their peaks in this band. The bimodal distribution in the optical spectra is clear in most of the distributions and absent from the PUV spectra. Examples from 0800 PST where the bimodal distribution is clear in the optical spectrum, (b), and absent in the PUV spectrum, (c).

Chapter 3: Directional wave field response to large-scale bathymetry

3.1 Abstract

A technique to measure directional wave spectra from electro-optical cameras was used to collect measurements of the large scale (roughly 700m by 700m) wave field at the 2003 Nearshore Canyon Experiment in the nearshore vicinity of the Scripps Canyon. Peak directions were determined from the measured wave field by modeling the directional distributions as a Gaussian function. Maps of the peak direction on 31 October and 18 November showed the influence of the local bathymetry for lower frequencies (less than 0.1 Hz), and maps of the calculated divergence patterns revealed alternating bands of focusing and spreading roughly corresponding to 100-200m alongshore bathymetric variability at the onshore portion of the canyon. Higher frequency waves were only affected by relatively shallow bathymetry (less than 15m), outside of the influence of most of the deeper canyon features. The alongshore position of the divergence patterns at lower frequencies is similar to the pattern of frequently occurring rip currents described and modeled by *Long and Özkan-Haller* [2005], and supports their findings of offshore controls on rip currents. Bimodal wave directions at the peak frequencies for both cases (0.125 Hz and 0.172 Hz) were simultaneously observed over most of the wave field. The observed 20° separations between the peaks are consistent with effects of wave shadowing by the offshore Channel Islands, described in earlier measurements by Pawka [1983].

3.2 Introduction

Wind generated waves arriving from the sea are the primary forcing in the nearshore. The incident waves respond to the patterns of the nearshore bathymetry due to depth and frequency dependency of the wave phase speed. This focusing and defocusing of the wave field by refraction over variable bathymetry will result in spatial gradients of wave energy and direction and in turn determines the patterns

of nearshore circulation and sediment transport. Complete understanding and accurate modeling of this complex system of nearshore processes are the ultimate goals of nearshore science.

The shoaling wave field for the simplest case of monochromatic waves and planar alongshore bathymetry is thought to be modeled well using Snell's law and linear dispersion. For more general and usually complex bathymetry a two-horizontal dimensional numerical model is necessary. Of course, in nature waves occur over a broad and continuous range of frequencies and directions, represented in terms of a two-dimensional frequency-direction spectrum. Again, in a simple model for shoaling waves each direction and frequency component is typically treated independently and subject to Snell's law. However, nonlinear evolution of wave spectra are typically observed and have been predicted [*Freilich and Guza*, 1984] [*Freilich et al.*, 1990; *Elgar et al.*, 1993], due to the nonlinear interaction of resonant (and near resonant) frequencies, and linear superposition of individual frequency and direction components is likely to give erroneous results.

The objectives in this study are to quantify and map the directional spectral characteristics of the wave field at Black's Beach near La Jolla, California, measured during the 2003 Nearshore Canyon Experiment (NCEX). NCEX was conducted to study the effect of large scale complex bathymetry on waves and currents and eventually to assess the effect of bathymetric controls on sediment transport in the nearshore. Much of the previous knowledge and modeling efforts for nearshore physical processes have been based on experiments conducted at relatively alongshore uniform beaches, where most bathymetry variability was contained in the surf zone [*Plant et al.*, 1999]. The NCEX site was chosen for the large (kilometers) scale irregular shoreline and subtidal bathymetry that is dominated by the close proximity of the Scripps Canyon. The transformation of waves, in particular, over the canyon has been know for many years to result in alongshore gradients in wave height and direction [*Emery*, 1958] which ultimately control the large scale patterns of circulation [*Shepard et al.*, 1941] and sediment

transport [*Munk and Traylor*, 1947]. The details of the wave field transformation are only modeled at this point [*Long and Özkan-Haller*, 2005], and no appropriate measurements are available to rigorously test available models. In this paper, we analyze directional wave spectra measured at a dense regular sampling grid using a remote optical wave spectrum estimation technique (Chapter 2). The two cases examined were chosen to represent a range of wave conditions experienced during NCEX. The large bathymetric gradients in close proximity to the shoreline are expected to cause dramatic changes in the wave field over a few hundred meters, and these changes should be readily apparent in the observed wave spectra, and will be compared with the underlying bathymetry. The ultimate goal will be to compare the observed spectra with available state of the art wave models.

3.3 Wave spectra at NCEX

The NCEX field site is located just north of the Scripps Institute of Oceanography in La Jolla California. The beach here is sheltered from some of the large offshore swell arriving from the open ocean by the Channel Islands, a network of islands extending along the southern California bight [*Pawka*, 1983]. The bathymetry at the site is dominated by the Scripps canyon, the tip of which comes within 500m of the shoreline and represents depth changes in that vicinity of 50m over less than 200m horizontal distance. The shoreline and underlying bathymetry is curved in the vicinity of the canyon, affecting almost 1500 meters of the NCEX site coastline. The majority of the *in situ* instrumentation for NCEX was located in this region within 1000m of the shoreline. The local coordinate system used in this study was right handed with the positive x-axis pointing offshore and the negative y-axis (roughly alongshore) oriented 19° east of true north.

Wave spectral shape was estimated for locations outside of the surf zone using a remote optical sensing technique described in Chapter 2. The spectral estimation technique is based on measuring variations in reflected skylight from waves at a two-dimensional array of locations, and calculating the frequency-

direction energy distribution of the wave field. The wave field is visible at a sensor (camera) due to the modulation of the reflected skylight. The radiance signal received by the camera is dependent on the degree of reflectance of the sky dome radiance, a function of the slope of the sea-surface Inverting the process, optical physics were therefore used to determine a simple modulation transfer function to accurately estimate time series of sea surface slope from observed time series of radiance. From slopes, sea surface elevations were found by integration. Because the cameras used in this experiment are not calibrated the magnitude of wave spectral energy is not calculated. Instead, only the relative energies, or spectral shape, are estimated. The technique relies on mapping of image to real world coordinates, and it is performed with standard photogrammetric techniques [*Holland et al.*, 1997].

The two-dimensional sampling array for an optical wave meter, herein after referred to as an alpha array, is a rhomboid shaped array of 17 uniquely spaced pixel elements, with the major axis (alongshore parallel) to minor axis (cross-shore parallel) ratio of 2:1. The alpha array has dimensions 100m in the alongshore (y) and by 50m cross-shore (x). Though sampling theory dictates this array is capable of resolving at most 100m length waves, synthetic tests (Appendix A) show the array and processing can resolve waves up to an order of magnitude larger than the cross-shore dimension of the array. The novel approach to measuring the broad NCEX domain wave field presented here is to tile alpha arrays over the region of interest (Figure 3.1). This aggregate of optical wave meters, called a tessellation array, is efficient in design because neighboring alpha arrays share pixels elements in the vertices and edges of each alpha array resulting in roughly 30% fewer pixels sampled over the whole tessellation array. The tessellation array used at NCEX spanned a wedge of the wave field roughly 700m alongshore and 700m in the cross-shore. Only pixels with less than 5m along-range resolution were sampled. Image intensity data were sampled at 2 Hz for 1024s length time series from each pixel in the tessellation array.

The time series were processed into estimates of frequency, f, and direction, θ, spectral density distributions, $S(f,\theta)$, using the technique and parameters outlined in *Chickadel and Holman* [in preparation]. Spectral density was estimated over 360° and for frequencies from 0.05Hz to 0.33Hz. The mean direction and energy spread in each frequency band were estimated using a Gaussian model,

$$S(\theta) = A\exp\left[\frac{-(\theta-\theta_p)^2}{2\sigma_\theta}\right] + B\,, \qquad (1)$$

in a nonlinear least-squares fitting routine, where θ_P is the peak direction, σ_θ is the half spreading width, analogous to the standard deviation, and A and B are gain and offset coefficients. Only estimates of θ_P and σ_θ where model skill (r^2) was greater than 0.8 ($r > 0.9$) and the estimated 95% single-sided confidence interval were less than 10° were considered.

Two examples of the optically derived wave field during NCEX, 31 October 1900 GMT and 18 November 1600 GMT, are examined here. The spatially-averaged frequency spectra for the measurement period on each day (Figure 3.2) indicate peak wave periods of 6s on 31 October and 8s on 18 November, Figure 3.3 and Figure 3.4 show the peak wave direction, θ_p, for each case for example a high frequency ($f = 0.17$ Hz), middle frequency ($f = 0.12$ Hz), and low frequency bands. For the lowest frequency band a band-average map was computed due to the low relative spectral energy and the resulting higher noise levels of some of the peak direction estimates.

Clear differences are evident between representative frequencies for both examples, particularly in the lowest frequencies. In general, the higher frequency waves appear to be less affected by the canyon bathymetry, with increasing apparent refraction resulting in a complex directional wave field in the lower frequency bands. Examples of $S(f,\theta)$ from the wave field for both cases are shown in Figure 3.5 and 3.6, corresponding to the circled locations shown in Figure 3.3 and 3.4, respectively. On 31 October, the example direction spectra show increasing difference in peak direction between the higher frequencies ($f > 0.15$

Hz) and lower frequencies (f < 0.15 Hz) with increasing distance to the north (-y direction). The swell frequency directions align well with the local shore normal (evaluated at the contour z = 0), and higher frequencies are more uniform between the examples. For the water depths indicated in Figures 3.5 and 3.6 (between 10m and 15m) frequencies greater than 0.15 Hz are in intermediate or deep water while swell frequencies (for example f > 0.15 Hz) are in relatively shallow water, hence swell waves are more likely to be affected by depth induced refraction. Similar differences are found from the examples on 18 November, though directional distributions at lower frequencies, f < 0.15 Hz, are not aligned with the local shore normal, suggesting these waves are influenced by other bathymetry. These differences are summarized by the directional span of peak direction for each frequency band (Table 1). In both cases, the directional wave fields are more uniform at the higher frequencies (smaller span) and increase direction non-uniformity (larger span) with decreasing frequency.

Table 3.1 Total range of peak direction over the measured wave field at selected frequency bands

	0.172 Hz	0.125 Hz	0.0781-0.0625 Hz
31 October 1900 GMT	28°	41°	87°
18 November 1600 GMT	33°	49°	69°

Interesting examples of apparent bimodal directional distributions are shown Figure 3.5a and especially in Figure 3.6c. In both cases the frequency of the bimodal distributions is near the peak frequency (f = 0.172 Hz). The bimodal distribution at 0.172 Hz was found again by fitting a Gaussian distribution function, a modified version of (1)

$$S(\theta) = A\left(\exp\left[\frac{-(\theta - (\theta_p - \Delta\theta))^2}{2\sigma_\theta} \right] + \exp\left[\frac{-(\theta - (\theta_p + \Delta\theta))^2}{2\sigma_\theta} \right] \right) + B \quad (2)$$

where $\Delta\theta$ is the half separation width around the central direction, θ_p. To simplify the analysis the model assumes equal energy, A, and standard width, σ_θ, for each peak. Figure 3.7 illustrates the ubiquity of bimodal directions at 0.172 Hz for 31 October and 18 November. For all cases, the model skill (r^2) was greater than 0.8, the 95% confidence interval. The average directional separation between peaks, $2\Delta\theta$, is 21° and 20° for 31 October and 18 November respectively. Interaction with bathymetry features is unlikely to cause bimodal distributions that occur simultaneously over the wide field sampled here. Instead, shadowing of the incident wind wave field by the offshore Channel Islands is the most likely cause, as was shown by *Pawka* [1983]. The 20° peak separation is consistent with the similar angular shadow caused by San Clemente and San Nicolas islands, though Pawka notes that local winds may mask the wave blocking signal. On 31 October 2003 the winds were generally less than 4 m/s and from the west and south west (roughly from the positive x direction), and on 18 November 2003 the winds were less than 2 m/s and blowing offshore most of the day.

3.4 Wave divergence

Maps of the directional wave field (Figure 3.5 and 3.6) suggest areas of convergence and divergence, and are expected to be associated with strong bathymetric features. Wave convergence (focusing) and spreading (divergence) lead to local amplification and reduction of wave energy density and flux, and can force mean flows by causing local pressure gradients. Unfortunately, the optical wave spectral estimation technique used here cannot be used to find increases in wave height from one location to the next. Instead a proxy, wave direction divergence, was computed for each frequency of interest in both cases examined above. A regular grid of the wave direction was interpolated using a LOESS interpolation scheme [*Plant et al.*, 2002] on a grid with 10m spacing in x and y and

with smoothing scales of 125m in both directions. The divergence, δ, of the peak wave direction field, $\theta_p(x,y)$, at any frequency is,

$$\delta(\theta_p) = \frac{\partial \cos\theta_p}{\partial x} + \frac{\partial \sin\theta_p}{\partial y}, \quad (3)$$

where the x and y notation have been dropped. Positives δ values indicate spreading, and negative values indicate focusing of the wave field.

The wave field divergence maps on 31 October (Figure 3.8) show startling differences between frequencies. At a high frequency (f = 0.17 Hz), the wave field is nearly uniform with slight divergence near the shoreline, though no patterns are discernable. At a middle frequency (f = 0.13 Hz) moderately more structure in the wave field is evident, and a small area of significant focusing and spreading of the wave field is seen near x = 350, y = -1050, apparently associated with the local shoal in the vicinity. In the swell frequencies (0.078 > f > 0.063 Hz), the focusing patterns appear to be more regular. Closer to shore (<20m depth), strongly alternating bands of converging and diverging wave directions are seen in Figure 3.8c, and roughly correspond to shoals and channels associated with the head of the canyon, which are of similar scale. Two main divergent bands, however, originate over bathymetry were there are no obvious bathymetric features of similar scale (approximately 100-150m) to cause the divergence patterns. Bathymetry features associated with the offshore extension of the canyon, and out of the range of the wave directional spectra measured here, may contribute to the observed divergence.

A very similar scenario existed on 18 November (Figure 3.9a-3.9b) with noticeable focusing and spreading associated with shallow bathymetry features (< 15m depth) and otherwise negligible wave divergence over most of the observed wave field for high frequencies (f > 0.13 Hz). In the lowest frequency band (0.078 > f > 0.063 Hz) similar alternating regions of focusing and de-focusing are observed (Figure 3.9c) and are associated with shoals and channels at the head of the canyon, though the position of focusing and spreading are roughly reversed from 31 October, and the divergence patterns do not extend as far seawards.

3.5 Discussion

Effects due to wave refraction over the complex bathymetry of the nearshore canyons offshore of La Jolla CA has been previously predicted [*Munk and Traylor*, 1947], though dense and wide simultaneous observation of directional spectra have not been previously measured. Synoptic measurements presented here clearly illustrate the effects of a complex bathymetric feature such as Scripps canyon on the incident wave field. In particular, the variation of observed refraction patterns with frequency is dramatic. These observations support the findings by *Long and Özkan-Haller* [2005], who show through spectral wave modeling that only longer period swell ($f > 0.1$ Hz) are refracted enough by the O(100m) undulations in the canyon walls to cause noticeable increase of wave height near the shore. Long and Özkan-Haller also show that the particular pattern of rip current circulation occurring periodically during the Nearshore Canyon Experiment is due to this canyon-caused refraction pattern, and is again consistent with the divergence patterns measured here. Bimodal directional distributions seen in certain frequencies and appear to be due to island shadowing, suggest that the directional resolution is adequate to distinguish 20° peak separations, a resolution not achievable with slope arrays, pitch-and-roll or point pressure-velocity derived directional spectra [e.g. *Oltman-Shay and Guza*, 1984].

These optical wave direction spectra measurements have important implications for wave and circulation modeling. The primary guidance suggested by the observations here is that care should be taken when modeling the transformation of the wave field over complex bathymetry. Ideally a spectral wave model should be used to accurately represent the wave field due to the frequency dependence of the bathymetry induced refraction, and thus the outcome of the wave-driven forcing in the nearshore. Also, as was seen here, with the observed wave shadowing by offshore islands, fine directional resolution may also be important for initiating wave models as again, details of the resulting wave forcing in and near the surf zone may be altered because of it. Though it was beyond of the

scope of this paper, the next step will be to test spectral wave models using optically measured directional spectra, and to force circulation models using the optical measured wave field.

3.6 Conclusions

A new optical method has allowed the first ever detailed glimpses of the large scale, O(100m-1000m), directional wave field and the refractive response of a natural wave field to complex bathymetry. Examples of the wave field during the 2003 Nearshore Canyon Experiment illustrate frequency dependence of the wave field directional transformation including focusing and de-focusing by local bathymetry features. However, only lower frequency waves, less than 0.1 Hz, are noticeably affected by the bathymetry deeper than 20m, while higher frequency waves respond to more shallow bathymetry close to the shoreline and out of the majority of the influence of the canyon. Divergence maps calculated at select frequencies aided in interpretation of the wave fields, and showed alternating bands of divergence and convergence approximately 100-200m in length in the alongshore direction, consistent with local bathymetry features and a previous wave model simulations by *Long and Özkan-Haller* [2005]. The divergence bands, which force frequent rip currents, therefore can determine the character of the nearshore circulation. Bimodal directional spectra in the peak incident frequency (0.172 Hz) were ubiquitous in the examples shown. The bimodal directional distributions have characteristics similar to the directional spectra measured by *Pawka* [1983], who showed them to be due to shadowing by the offshore Channel Islands. An extension of this work will be to force circulation models using the optically measured wave field, in addition to testing wave model performance in complex bathymetry cases.

3.7 References

Chickadel, C.C., and R.A. Holman (in preparation), Optical estimation of nearshore directional wave spectra, *Journal of Geophysical Research*.

Elgar, S., R.T. Guza, and M.H. Freilich (1993), Observations of nonlinear interactions in directionally spread shoaling surface gravity waves, *Journal of Geophysical Research*, *98* (C11), 20,299-20,305.

Emery, K.O. (1958), Wave patterns off Southern California, *Journal of Marine Research*, *17*, 133-140.

Freilich, M.H., and R.T. Guza (1984), Nonlinear effects on shoaling surface gravity waves, *Philosophical Transactions of the Royal Society Series A*, *311*, 1-41.

Freilich, M.H., R.T. Guza, and S.L. Elgar (1990), Observations of nonlinear effects in directional spectra of shoaling gravity waves, *Journal of Geophysical Research*, *95* (C6), 9,645-9,656.

Holland, K.T., R.A. Holman, T.C. Lippmann, J. Stanley, and N. Plant (1997), Practical use of video imagery in nearshore oceanographic field studies, *IEEE Journal of Ocean Engineering*, *22* (1).

Long, J.W., and H.T. Özkan-Haller (2005), Offshore controls on nearshore rip currents, *Journal of Geophysical Research*, *110* (C12007).

Munk, W.H., and M.A. Traylor (1947), Refraction of ocean waves: a process linking underwater topography to beach erosion, *Journal of Geology*, *55*, 1-26.

Oltman-Shay, J.M., and R.T. Guza (1984), A data-adaptive ocean wave directional-spectrum estimator for pitch and roll type measurements, *Journal of Physical Oceanography*, *14*, 1800-1810.

Pawka, S. (1983), Island shadows in wave directional spectra, *Journal of Geophysical Research*, *88* (C4), 2579-2591.

Plant, N.G., R.A. Holman, and M.H. Freilich (1999), A simple model for interannual sand bar behavior, *Journal of Geophysical Research*, *104* (C7), 15755-15776.

Plant, N.G., K.T. Holland, and J.A. Puleo (2002), Analysis of the scale of errors in nearshore bathymetric data, *Marine Geology*, *191* (1), 71-86.

Shepard, F.P., K.O. Emery, and E.C. La Fond (1941), Rip currents: a process of geological importance, *Journal of Geology*, *49*, 337-369.

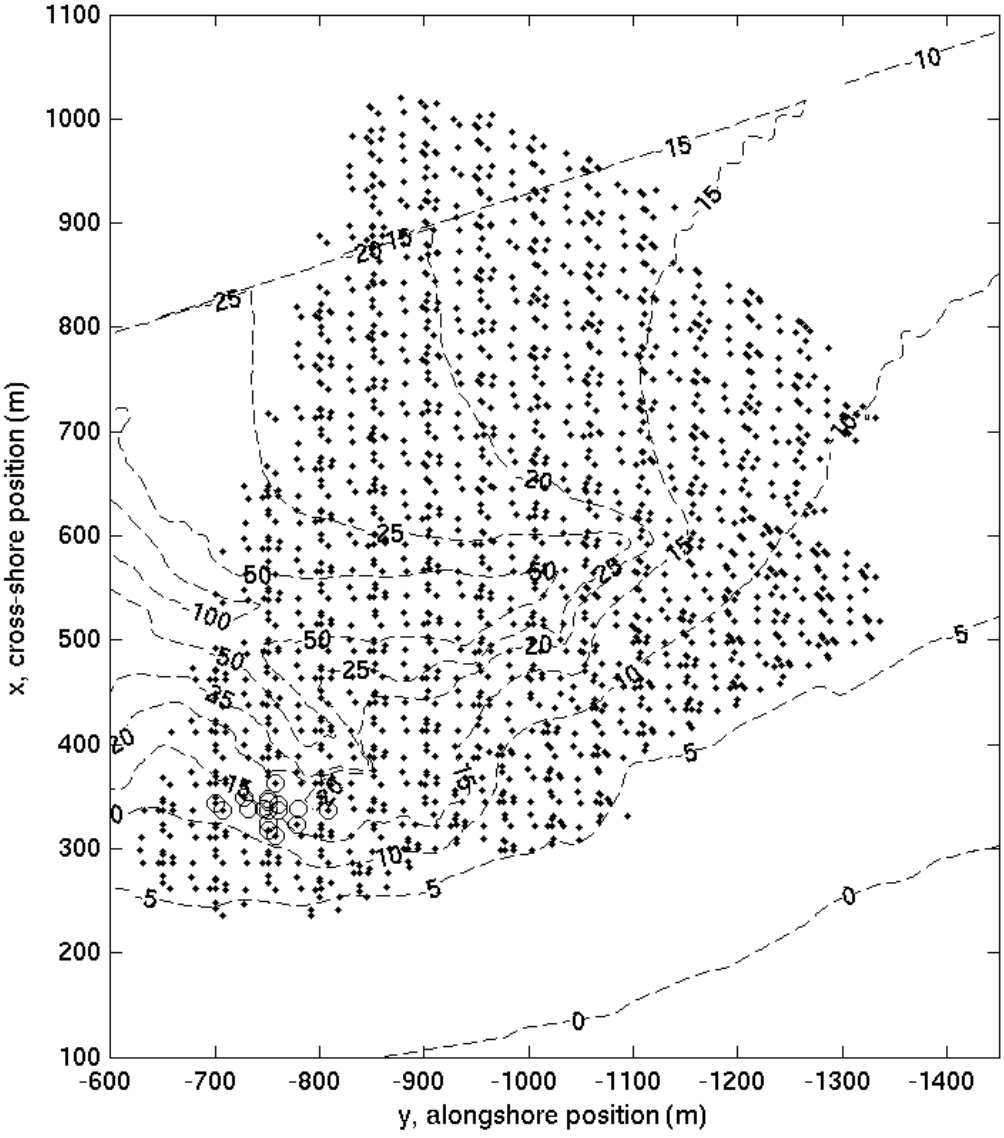

Figure 3.1 The tessellation array (points) used to measure the directional wave field at in the vicinity of the Scripps Canyon during the Nearshore Canyon Experiment, on 31 October 2003. An example single directional wave array (alpha array) is shown (circles). The bathymetry of the canyon is shown in meters below NGVD.

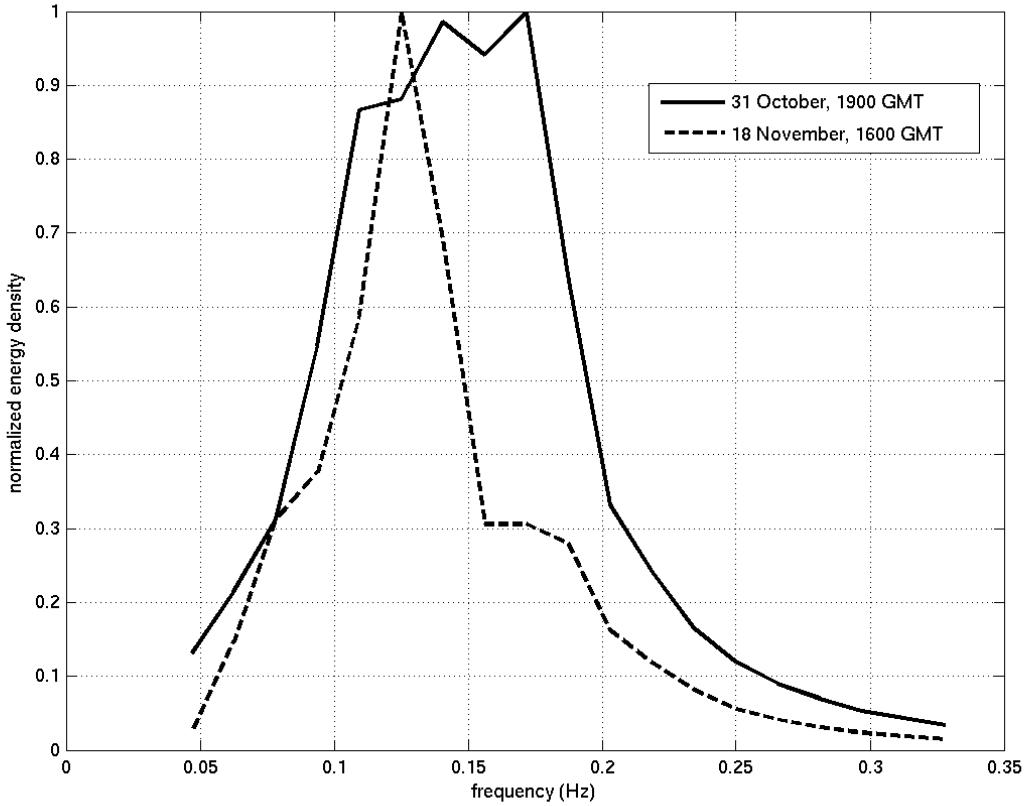

Figure 3.2 The average normalized frequency spectra from the tessellation array on 31 October and 18 November.

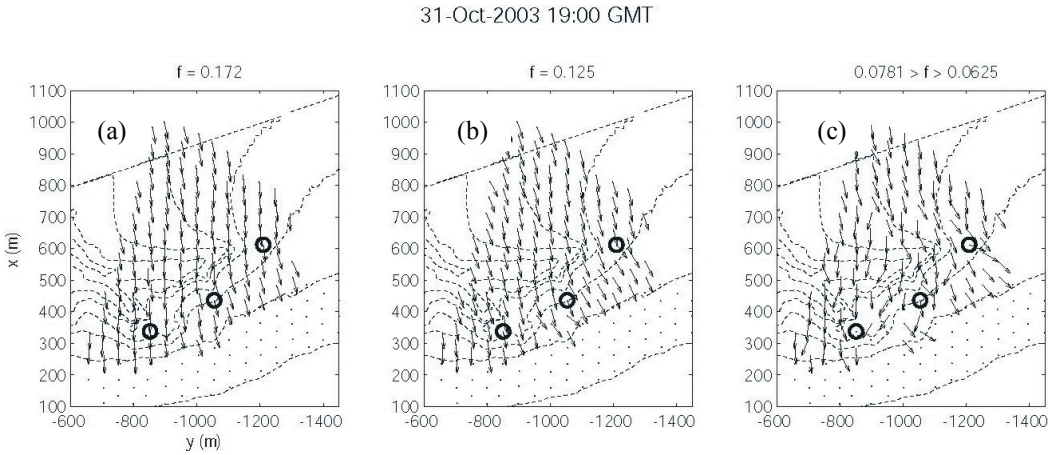

Figure 3.3 Peak wave direction fields on 31 October 1900 GMT for a selection of three frequencies, (a) 0.172 Hz, (b) 0.125 Hz and the average peak direction over the band from 0.0781 Hz to 0.0625 Hz. The bathymetry is shown at intervals of 5m (as in Figure 1) from 0m to 100m. Circles indicate locations of the frequency directional spectra shown in Figure 3.5.

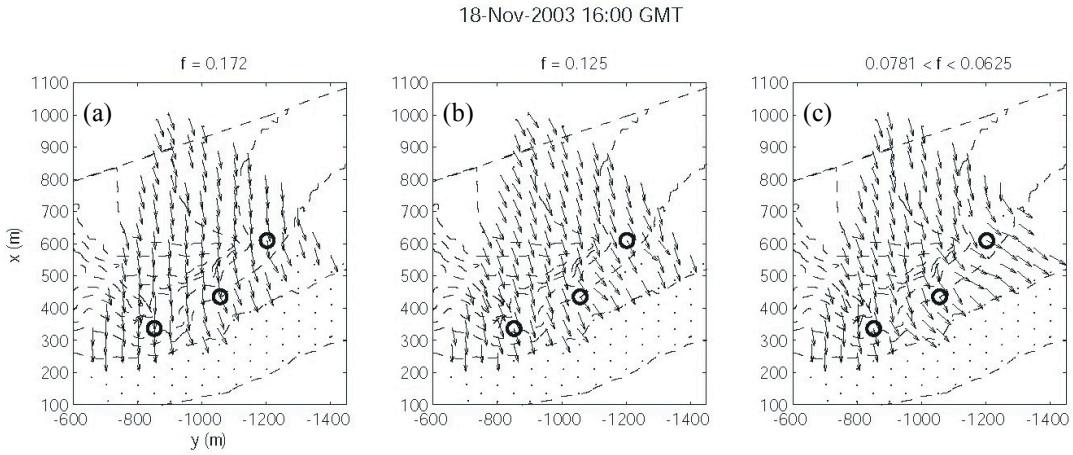

Figure 3.4 Peak wave direction fields on 18 November 1600 GMT for a selection of three frequencies, (a) 0.172 Hz, (b) 0.125 Hz and (c) the average peak direction over the band from 0.0781 Hz to 0.0625 Hz. The bathymetry is shown at interval of 5m (as in Figure 1) from 0m to 100m. Circles indicate locations of the frequency directional spectra shown in Figure 3.6.

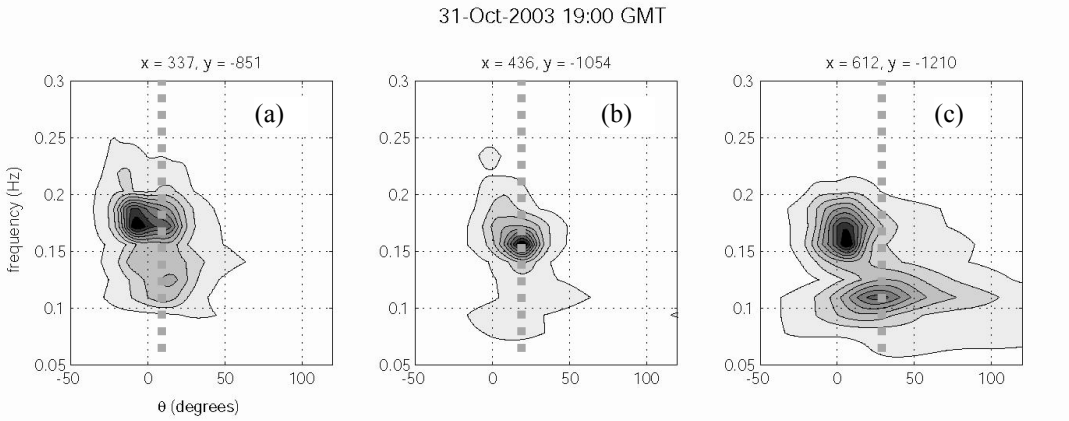

Figure 3.5 Individual frequency-directional spectra, from the locations indicated in Figure 3.3, plotted from south (a) to north (c). The x,y locations are shown above each panel. Local shore normal (relative to the 0m contour) is indicated by the dashed vertical line.

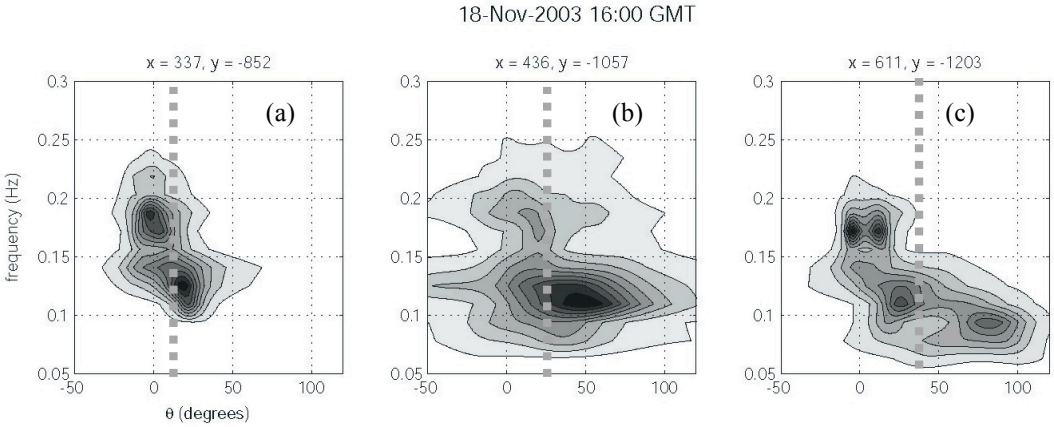

Figure 3.6 Individual frequency-directional spectra, from the locations indicated in Figure 3.4, plotted from south (a) to north (c). The *x*,*y* locations are shown above each panel. Local shore normal (relative to the 0m contour) is indicated by the dashed vertical line. An easily distinguishable bimodal directional distribution is shown in (c).

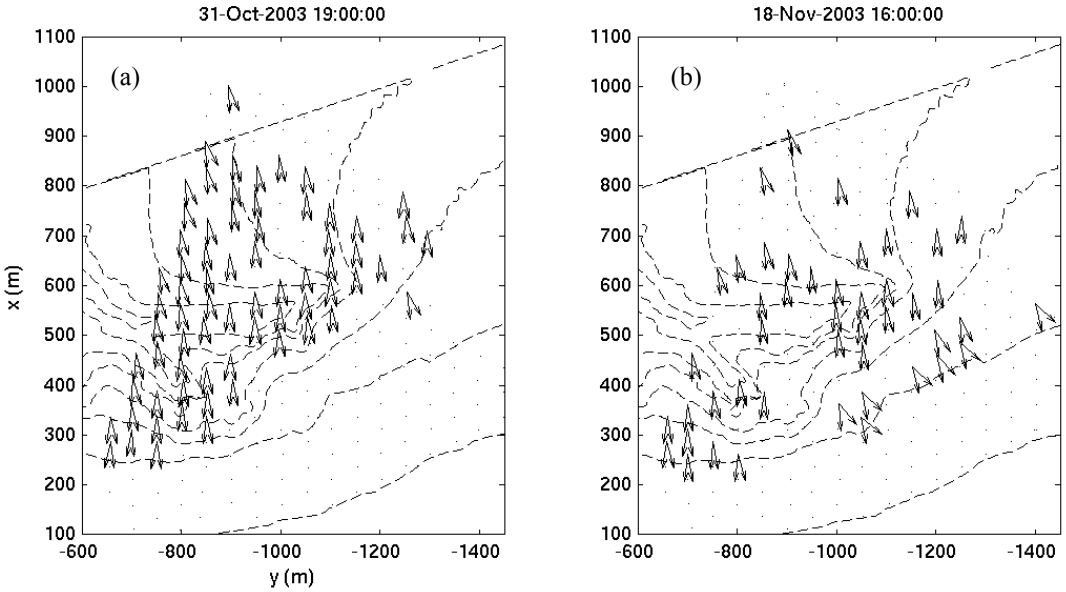

Figure 3.7 Maps of the fitted bimodal peak directions at 0.172 Hz on (a) 31 October and (b) 18 November. Wave direction vectors are shown only if the fitted bimodal Gaussian model was significantly different from a unimodal model (see section 3.3.3).

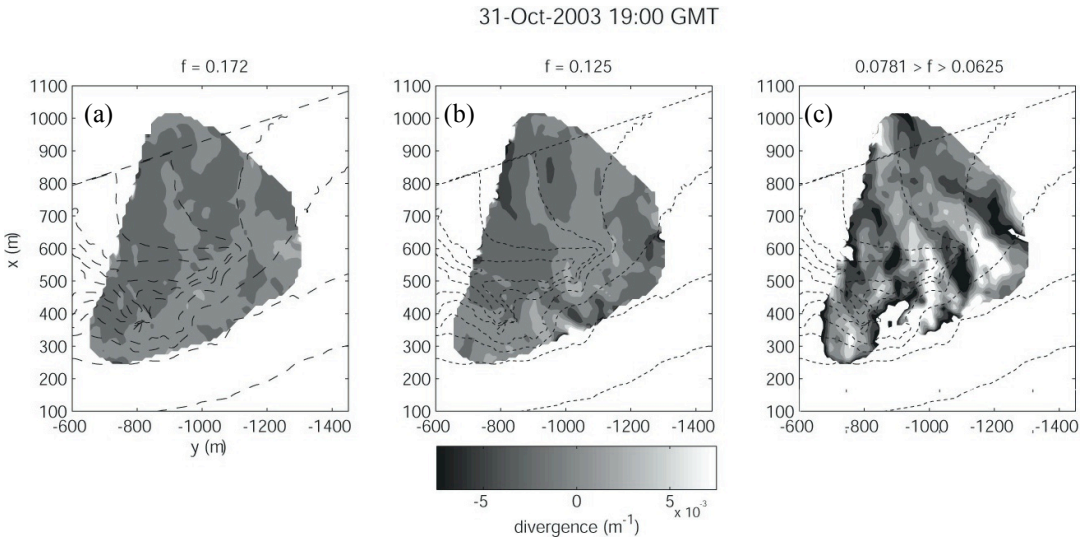

Figure 3.8 Divergence maps of the observed wave field on 31 October 2003 1900 GMT for the frequencies, (a) 0.17 Hz, (b) 0.13 Hz and (c) over the band 0.078-0.063 Hz. The 5m spaced depth contours (dashed) are shown for reference. In each map wave focusing is negative (darker) and wave spreading is a positive (lighter) value.

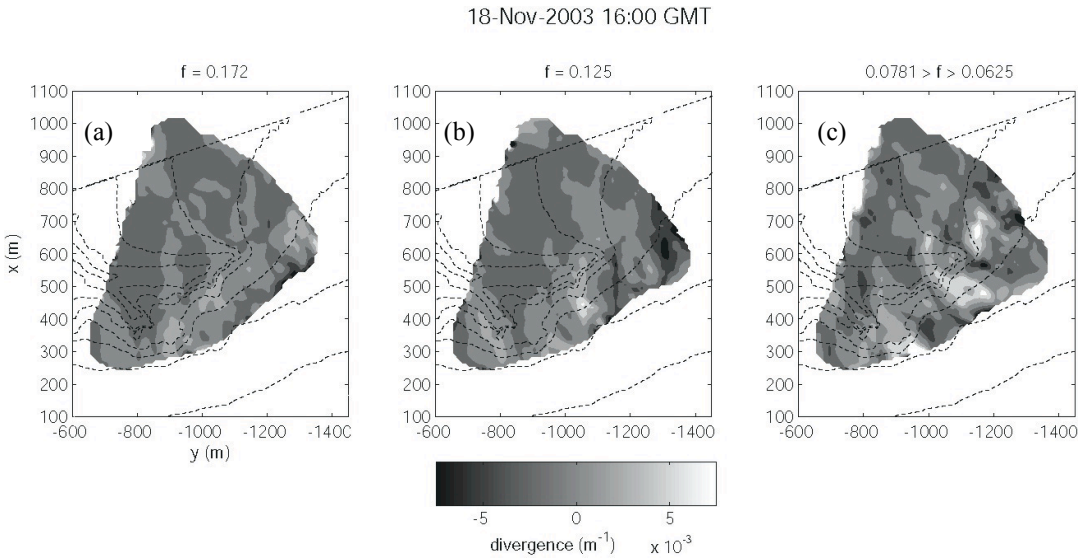

Figure 3.9 Divergence maps of the observed wave field on 18 November 2003 1600 GMT for three frequency bands, (a) 0.17 Hz, (b) 0.13 Hz and (c) 0.078-0.063 Hz. The 5m spaced depth contours (dashed) are shown for reference. In each map wave focusing is negative (darker) and wave spreading is a positive (lighter) value. Weak divergence patterns in the lowest frequencies (c) are contrasted with the strong focusing patterns on 31 October (Figure 3.8c).

Chapter 4: Alongshore variability of longshore currents at a barred beach

4.1 Abstract

Mean surface longshore currents were measured twice daily for 14 months at Duck NC from a two-dimensional array of 28 optical current meters, over a range of wave and bathymetric conditions. Two criteria were used to judge whether currents were alongshore-variable: observation of significant alongshore non-uniformity in current strength, or observation of the location of maximum current shoreward of the region of visible wave breaking over the sand bar (assumed indicative of significant alongshore pressure gradients). Of the 218 runs with sufficient data return, conditions for longshore uniformity failed 71% of the time, in contrast to previously-documented observations of a strong predominance of alongshore-uniform dynamics at the same site. A proxy for bathymetric alongshore variability, based on alongshore-variability of the inner bar position and measured from visible wave breaking patterns, was found to be only a weak (but statistically significant) predictor of non-alongshore-uniform currents. A simple point model for the mid-surf zone longshore current performed surprising well (r^2=0.57; rms error 38 cm/s). Rip currents, computed from divergences of longshore currents, were found to occur at offshore deviations in optically-derived bar crest locations.

4.2 Introduction

One long-term goal of nearshore processes research has been the development of a sufficient understanding of nearshore physics to allow predictions of beach erosion and shoreline movement over the large spatial scales and long time periods required for coastal zone management. Erosion and accretion of shorelines are primarily a result of gradients in longshore sediment transport, and since sediment transport is, in turn, driven by longshore currents, there is a practical

interest in the efficient estimation and prediction of longshore currents over appropriate spatial and temporal scales.

A variety of longshore current models are in use, typically based on various simplifications of the dynamic balance between wave radiation stress gradients [*Longuet-Higgins and Stewart*, 1964], alongshore pressure gradients, wind stress, bottom friction and mixing. These models can be classified according to the domain spanned, from point models of current magnitude and direction to those that predict a depth-averaged, cross-shore profile (one horizontal dimension, or 1HD), a depth-averaged two-dimensional field (2HD), and finally a fully three-dimensional description (3D) of mean flows. While 2HD and 3D models provide visually realistic results and can be used for general bathymetries, they remain more complicated to set up and run and require extensive and accurate bathymetric survey data since they are sensitive to bottom boundary conditions [*Long and Özkan-Haller*, 2005]. Such data are seldom available, making everyday application of these more complicated models unlikely. In contrast, point and 1HD models are more easily implemented, requiring only wave height, wave angle and (for 1HD models) an estimate of the cross-shore bathymetry. The simpler logistics of these more approximate point models – and to a lesser degree 1HD models – makes them very attractive, so determination of their accuracy for "typical beaches" becomes important.

The most common point model for longshore velocity, by *Komar and Inman* [1970], assumes an alongshore-uniform planar beach profile and simply balances wave forcing with bottom friction to yield a single value, considered representative of a peak velocity that would be observed near a mid-surf zone location. The Komar and Inman formula for the "mid-surf zone" longshore current,

$$V_{mid} = 1.0\sqrt{gH_{bs}}\sin\alpha_b\cos\alpha_b \qquad (1)$$

requires only an estimate of significant breaking wave height, H_{bs}, and breaking wave angle, α_b. Comparisons of (1) with laboratory and field tests indicate good

agreement [*Komar and Oltman-Shay*, 1990], though the comparison data set of longshore currents was sparse compared to what is now available.

1HD models [e.g. *Bowen*, 1969; *Longuet-Higgins*, 1970] compute cross-shore profiles of the depth-averaged longshore current under the assumption of alongshore uniform bathymetry, hence neglecting the role of longshore pressure gradients. These models agree well with longshore current observations from simple planar beaches if the horizontal spread of forcing due to random waves is incorporated [*Thornton and Guza*, 1986]. However, observations at barred beaches often show unexpected model-data mismatches where the cross-shore location of the peak longshore current, expected to coincide with maximum wave forcing over the bar, is significantly shoreward of the modeled maxima [*Church and Thornton*, 1993; *Smith et al.*, 1993]. It has been suggested that this shoreward shift of the peak current location could be due to the role of wave rollers, the volume of turbulence seen on the front face of spilling breakers, in delaying momentum transfer from the coherent wave motions to the mean currents [e.g. *Svendsen*, 1984b; *Svendsen*, 1984a; *Reniers and Battjes*, 1997; *Ruessink et al.*, 2001; *Feddersen et al.*, 2004]. A second plausible explanation, the effect of alongshore pressure gradients arising due to alongshore bathymetric variability, has received much less study owing to the difficulty and cost of making the appropriate measurements in large-scale field experiments. Yet the effect of pressure gradients is thought to be significant even under conditions of mild alongshore bathymetric variation [*Putrevu et al.*, 1995; *Haller et al.*, 2002].

Several recent studies have tested 1HD models against extensive datasets. *Ruessink et al.* [2001] examined data from major field experiments on two barred beaches (1000 hours of observations from Duck94 at Duck, NC and 500 hours from the 1998 Coast3D experiment at Egmond, The Netherlands). The data were collected mainly during periods of alongshore-uniform bathymetry and good overall agreement was found between measured and modeled longshore current profiles. However, Ruessink and coauthors did find a decrease in model accuracy

during periods of increased alongshore bathymetric variability, measured using their χ^2 statistic estimated from extensive 2D bathymetric survey data and defined as the area average of $\left[\left(h(x,y)-\overline{h}(x)\right)/\overline{h}(x)\right]^2$, where $\overline{h}(x)$ is the alongshore average depth profile. Assuming a χ^2 threshold of 0.02, they determined that 1HD models were accurate for 70% of the data from Duck94 and 60% from Coast3D.

Feddersen and Guza [2003] examined four months of data from the 1997 SandyDuck experiment, the most densely-sampled nearshore experiment in history. Based on careful analysis of 5 cross-shore arrays spanning 200m in the longshore, they concluded that alongshore non-uniformity was only detectible in the innermost of their five cross-shore locations, and that rip currents were observed only once, based on rip current detection criteria outlined in *Feddersen and Guza* [2003]. Thus, they concluded that a 1D alongshore momentum balance was a good representation of the dynamics and could safely be used during the experiment.

While the above papers conclude that 1HD models are adequate for most purposes, it must be noted that the data on which they are based are not ideal for this test, despite the fact that these arrays were among the most extensive ever fielded. For SandyDuck, typically only the innermost line of 5 sensors was in the surf zone (taken here as $x \leq 200$m in the FRF coordinate system, see section 2.1 for a complete description of the FRF coordinate system). Alongshore sampling was not a major part of the Duck94 design and, for Coast3D, was sparse compared to important circulation phenomena such as rip currents.

In this paper, we analyze a relatively dense 28-element array of longshore current measurements, using a recently-developed Optical Current Meter (OCM) method for longshore current estimation [*Chickadel et al.*, 2003]. While these data are of lower accuracy than *in situ* sensors and do not work under all conditions, two-dimensional spatial sampling can be achieved over long periods of time. In contrast to the SandyDuck array, the majority of the OCMs used were within the area of active breaking (20 of 28 instruments) during most conditions.

Our objectives are to investigate the dynamics and alongshore uniformity statistics of longshore currents based on a 14-month data set of optical current measurements from Duck NC. For much of this experiment, longshore current spatial patterns were complex, suggesting that 1D dynamic assumptions of alongshore uniformity were not satisfied and alongshore pressure gradients were significant. Two criteria will be used to detect the failure of 1HD dynamics; observation of the location of maximum current well shoreward of the cross-shore position of maximum wave forcing (section 3.2) or observation of significant alongshore variability in the longshore currents (section 3.3). In section 3.4 a simple optical proxy for predicting 1HD failure will be investigated. One-dimensional profile models will not be tested directly, because bathymetry data were not regularly sampled or were otherwise not available. However, the accuracy of the *Komar and Inman* [1970] mid-surf longshore velocity model will be examined over the observed range of conditions (section 4). This is followed by discussion (section 5) and conclusions (section 6).

4.3 Optical and in situ measurements

4.3.1 Field Site: Duck NC

Measurements of currents and waves were taken at the US Army Corps of Engineers Field Research Facility (FRF) at Duck, NC, where the beach is usually barred but can exhibit a range of alongshore variable morphologies including rip current channels and rhythmic sand bars [*Lippmann and Holman*, 1990; *Plant et al.*, 1999; *Alexander and Holman*, 2004]. The average wave height at Duck is about 1m, with larger waves in the winter as a result of storms from the northeast, and occasionally in the summer and fall due to the passage of infrequent hurricanes. The FRF coordinate system is right-handed with the positive x-axis pointing offshore, the y-axis parallel to the alongshore direction and z vertical upward. The shoreline is typically near x = 100m, perpendicular to a large pier located at y = 510m.

Wave statistics during this experiment, including peak direction, α, significant wave height, H_s, and peak period, T_p, were calculated from an array of 15 pressure sensors in 8m water depth (called the "8 meter array") roughly 800m from shore [*Long and Oltman-Shay*, 1991]. Wave statistics were interpolated to the times of current meter observations with a LOESS interpolation scheme [*Plant et al.*, 2002] with a smoothing window length of 9 hours. Gaps in the 8 meter array data were filled with observations from an offshore Waverider buoy located in 18m water depth, shoaled to 8m depth using Snell's law, assuming straight and parallel contours. Directions are represented with respect to the FRF coordinate system; positive (negative) angles indicate waves arriving from the north (south) of shore-normal.

Figure 4.1 summarizes wave and longshore current conditions during the experiment. Significant wave height ranged from 0.2m to 4.3m, α varied between -60 and 66 degrees from normal and the maximum alongshore-mean longshore current (explained in section 3.1) varied between -1.7 m/s (flow to the south) and +1.4 m/s.

4.3.2 Roller dissipation proxy

Dissipation patterns were estimated using ten-minute time-exposure images (e.g. Figure 4.2a), one of a suite of products routinely used in optical monitoring of morphologic development in the nearshore [*Lippmann and Holman*, 1989]. Observed intensity patterns in these images are the integrated result of active wave breaking over bars and shoals, residual bubbles and foam left after the passage of breakers, and a darker background scene. *Aarninkhof and Ruessink* [2004] determined that the excess brightness of intensity bands over offshore sand bars was best related to the dissipation of wave rollers. While residual foam may dilute this pattern, it is assumed that the location and cross-shore extent of the pattern should provide a reliable proxy for the location and spatial extent of roller dissipation [*van Enckevort and Ruessink*, 2001; *Aarninkhof and Ruessink*, 2004], with the most probable error being that the peak in roller dissipation identified in

time-exposure images may actually be slightly shoreward of the true peak due to the expected shoreward advection of residual foam. The procedure to quantify these variables is described, following *Alexander and Holman* [2004] and *Aarninkhof and Ruessink* [2004]. Note that this technique does not attempt to quantify the magnitudes of roller dissipation.

Cross-shore transects of image intensity $I_R(x, y')$, at particular longshore locations y', were extracted from the suite of collected images using standard photogrammetry procedures [*Holland et al.*, 1997]. For each longshore location, the image intensity profile, $I_R(x)$ is modeled as the superposition of a linear ramp and three Gaussian bumps,

$$I_R(x) = Ax + B + \sum_{j=1}^{3} A_R(j) \exp\left\{ \frac{-(x - \mu_R(j))^2}{2\sigma_R^2(j)} \right\}, \qquad (2)$$

where A is the gradient in the background illumination above a base intensity B, A_R is the amplitude, μ_R the center, and σ_R is the width of each Gaussian hump. The three Gaussians, j = 1, 2 and 3, are used to model the position of the shore break, inner bar and outer bar respectively by constraining the mean positions, $\mu_R(j)$, to be < 140m, between 140m and 275m, and > 275m, respectively. The model was applied to observed time averaged intensity profiles, $\bar{I}(x)$, (e.g. Figure 4.2a, b) at a total of 17 cross-shore profiles, spaced every 30m alongshore from y = 520m to 1000m, using a nonlinear least squares fitting routine. Image intensities were longshore-averaged within each 30m bin. Ninety-five percent confidence intervals were estimated using the residuals to the model-data fit [*Bates and Watts*, 1988].

Data were dropped from further consideration if they failed one or more quality control conditions. Locations of dissipation centers $\mu_R(j)$ and dissipation widths $\sigma_R(j)$ with 95% confidence intervals greater than ±10m were removed. Similarly, broad, high intensity patches in the image due to sun glare occasionally mimicked broad breaking regions offshore. Erroneous estimates of μ_R based on these glare patterns were removed by requiring $A_R(j) \geq 0.25B$, or that the intensity

magnitude of offshore roller dissipation was at least 25% of the base image intensity. Finally, derived statistics from an image (described below) were considered acceptable only if at least 12 of the 17 transects yielded acceptable estimates. A total of 303 of the 817 possible observations passed all three criteria.

Several morphodynamic variables were computed from model parameters. The quantity $\mu_R(1) + \sigma_R(1)$ was tested and found to be a visually-acceptable proxy for shoreline position, $x_s(y)$. The center position of roller dissipation at the inner bar, x_R, is taken as $\mu_R(2)$ and the width of breaking at the inner bar is taken as $2\delta_R$, where δ_R is defined as the value of $\sigma_R(2)$ from equation (2). The time series of alongshore-mean shoreline position $\overline{x_S}$, alongshore-averaged inner bar position $\overline{x_R}$, alongshore standard deviation of the inner bar position σ_{x_R}, and the alongshore-averaged width of breaking over the bar, $\overline{\delta_R}$, are summarized in Figures 4.3a and 4.3b.

The average position of the dissipation at the inner bar demonstrated a roughly seasonal pattern (Figure 4.3a), migrating offshore during December 2003 and January 2004 and then slowly shoreward until August 2004 and offshore again until the end of sampling in December 2004. During February to November 2004 the bar developed increased alongshore variability within the measurement array, represented by increased σ_{x_R} (Figure 4.3a). A non-dimensional proxy, γ_B, was calculated to quantify alongshore bathymetry variability (Figure 4.3c), based on the ratio of alongshore standard deviation of the inner bar position to alongshore mean bar width

$$\gamma_B = \frac{\sigma_{x_R}}{\overline{\delta_R}}. \qquad (3)$$

It should be noted that γ_B is not intended to be a strict proxy for previous measures such as χ^2, used by *Ruessink et al.* [2001] and shown for comparison in Figure 4.3c. The latter is an area average of fractional depth change, so emphasizes shallow depths and is only indirectly related to the more dynamically important forcing

terms. The metric introduced here is chosen and tested because it can be optically derived, and because it appears to be a direct measure of significant alongshore variation of forcing. The metric γ_B is expected to be sensitive to instances when the influence of bathymetry on the alongshore structure of the current is overtaken by large wave forcing.

Alongshore variability, as indicated by γ_B, increased from about 0.3 at the start of the experiment in November 2003 to a maximum of 1.5 in April 2004 and remained scattered with only a few significant events until the end of the experiment in December 2004. The modal value for γ_B, determined from an empirical histogram (Figure 4.3d), is between 0.3 and 0.4. In section 3, γ_B is compared to statistical measures of the alongshore variability of the longshore current field.

4.3.3 Longshore currents

Longshore currents were measured from a 2D horizontal array of 28 optical current meters (OCMs). The current meter array (Figure 4.4) consisted of two cross-shore transects of eight instruments each spanning 175m cross-shore and separated 140m in the alongshore and three alongshore arrays of six instruments each, sharing six OCMs with the cross-shore arrays, spanning 230m alongshore and 50m cross-shore. The average alongshore image resolution for all OCMs is 0.3 m/pixel, with a worst case resolution of 0.5 m/pixel. The optical current meter technique is described fully in *Chickadel et al.* [2003] and entails estimating longshore currents from video observations of alongshore-advected residual surface foam by frequency-wavenumber analysis. Typical root-mean-square differences between mean currents from *in situ* electromagnetic current meters and OCMs are 10 cm/s [*Chickadel et al.*, 2003]. For this experiment, currents were measured twice daily for 1024 s, beginning 6 November, 2003 and ending 31 December, 2004. A 32 second analysis window with 50 percent overlap was used to estimate a time series with a nominal length of 63 points, although final lengths were often

shorter after quality control screening as described in *Chickadel et al.* [2003]. For example, longshore current estimates based on sub-critical foam tracer contrast or estimates with 95% confidence ranges greater than ±10 cm/s were removed. Mean currents were calculated from the remaining time series and corrected for estimated apparent velocity due to image misregistration errors [*Chickadel et al.*, 2003], a calculation which requires estimates of water depth, mean wave height, wave period and wave angle at the points in the optical array. Wave height at each current meter was not measured, but was estimated based on a saturated breaking wave height profile, $H_b(x)$, using

$$H_b(x) = \gamma h(x), \tag{4}$$

where $\gamma = 0.32$ is the ratio of root-mean-square breaking wave height to water depth [*Sallenger and Holman*, 1985]. Approximate water depth, *h(x)*, was taken from a two part linear approximation of the 16 year mean profile for Duck [*Plant et al.*, 1999] and corrected for local tide, measured at the pier end. The mean magnitude of the correction was small, 0.07m/s, and the resulting currents were not sensitive to errors in the above assumptions. Mean current estimates which had less than five valid measurements in a single time series (of a possible total of 63), estimated misregistration error magnitudes greater than 25 cm/s, or corrected magnitudes greater than 2 m/s were removed leaving 6958 total individual mean current estimates over 410 days, or 30% of the total possible observations.

4.4 Longshore current analysis

In this section the spatial variability of the measured alongshore currents is examined and compared to the assumptions of 1HD dynamics. Two criteria for failure of these assumptions are investigated; a) observation of the cross-shore location of peak velocity shoreward of the region of forcing, taken as the region of roller dissipation, and b) observation of significant alongshore variability of the observed currents. It is assumed that either condition will be the result of alongshore-variable bathymetry and the associated development of local alongshore

pressure gradients [*Putrevu et al.*, 1995; *Reniers et al.*, 1995; *Sancho et al.*, 1995; *Slinn et al.*, 2000].

4.4.1 Alongshore-mean profiles

Alongshore-averaged longshore current profiles were computed and their bulk statistics calculated. Figure 4.5a shows that for the majority of the time the strongest and most variable currents were located between the 14 month-averaged cross-shore bar location and the shoreline, with weaker currents offshore of the mean bar position. The observed extremes of $\overline{V}(x)$ were -1.7 m/s and 1.4 m/s measured at x = 170m and x = 195m, respectively. There was a slight negative (southward flow) bias in the total mean longshore currents over the 14 month experiment, although the bias was only significantly different from a mean of 0.0 m/s for the region 120m $\leq x \leq$ 195m (at a 95% confidence level [*Bethea et al.*, 1995]). Average current profiles for wave directions from the north ($\alpha>0°$) and south ($\alpha<0°$) are very similar in shape, though the mean currents for $\alpha>0°$ were twice as large compared to when $\alpha<0°$ (Figure 4.5b).

It is assumed that displacement of the location of current maximum landward, away from roller forcing, can only be due to alongshore pressure gradients. Thus, the degree of mismatch between the locations of visible roller dissipation and of the observed longshore current maxima $\overline{V_m}$ was examined as a proxy test for the validity of assumptions of alongshore-uniform bathymetry and 1HD forcing. To limit the influence of dynamics that might be occurring seaward of the inner bar or near the shoreline, allowable cross-shore positions of the maximum alongshore velocity, $x_{\overline{V_m}}$, were limited to between the shoreline position, $\overline{x_S}$, and the offshore limit of breaking over the inner bar, $\overline{x_R} + \overline{\delta_R}$. To reduce the influence of sparse measurements and small currents, only observations for which at least 2 OCMs were valid at each cross-shore position, whose maximum magnitude was greater than 20 cm/s and for which valid currents were

measured over the bar and trough simultaneously were considered. A total of 165 observations passed these criteria.

The time series of $x_{\overline{V_m}}$ (Figure 4.6a) appears to roughly track the location of maximum breaking over the inner bar for the first two and last four months of the experiment but is clearly landward of the active forcing region for much of the winter of 2004. Figure 4.6b shows the same relationship in terms of the normalized peak current position, $x'_{\overline{V_m}}$, given by

$$x'_{\overline{V_m}} = \frac{(x_{\overline{V_m}} - \overline{x_R})}{\overline{\delta_R}}. \qquad (5)$$

Shoreward bias of the longshore current maximum ($x'_{\overline{V_m}}$<-1) was strongest in 2004 between mid-January and April and later again between September and November. In total, 84 of the 165 observations (51%) show longshore current maxima shoreward of visual wave breaking, at the inner bar (Figure 4.6c). Due to the uneven cross-shore density of the array, the cross-shore profile of the longshore current may exhibit shoreward bias during January to March 2004, when the inner bar moved 75m offshore. For clarification, instances when the most dense part of the OCM array was sampling over the inner bar (i.e. $\overline{x_R} - \overline{\delta_R}$ <195m) are highlighted by circles in Figure 4.6c. This reduced set of observations (120 out of 165) retained the general trend of all the points. A full discussion is continued in section 4.4.4.

4.4.2 Alongshore non-uniformity

A second symptom of the failure of 1HD dynamics is the observation of significant alongshore variability in measured currents. The alongshore mean ($\overline{V}$) and standard deviation (σ_V) of alongshore currents were computed for each of the three alongshore OCM arrays within the surf zone (i.e. for currents between 145m $\leq x \leq$ 195m). A bulk measure of the standard deviation normalized by the absolute mean alongshore velocity, was calculated by a cross-shore average of these values,

$$\overline{\sigma_V / |\overline{V}|} = \frac{\sum_N \sigma_V}{\sum_N |\overline{V}|}, \qquad (6)$$

where N is the number of alongshore transects included in the averaging. A threshold value of 0.25 was chosen as a criterion for alongshore non-uniformity.

Values computed using equation (6) could be biased by the impact of low mean velocities or noisy estimates of standard deviation. To limit the impact of noise from sparse measurements and small velocity magnitudes, values from a longshore transect were included in the averaging only if three or more of the six OCMs in the transect yielded measurements and only if the alongshore-mean value exceeded 20 cm/s ($|\overline{V}_m| > 20$cm/s). A total of 262 observations passed these criteria. Since OCM estimates have a demonstrated measurement error of 10 cm/s [*Chickadel et al.*, 2003], some level of variability due only to instrument noise, σ_{crit}, is expected. The 95% critical noise threshold, σ_{crit}, was calculated as

$$\sigma_{crit} = \left(\frac{\sigma_n^2 \chi^2_{m-1,1-\beta}}{m-1} \right)^{\frac{1}{2}} \qquad (7)$$

where $\chi^2_{m-1,1-\beta}$ is the value of the chi-squared distribution with m-1 degrees of freedom and probability level 1-β. Here, m is the total number of active current meters in the sub-array and $\beta = 0.05$. Observed values of $\overline{\sigma_V}$ less than σ_{crit} were considered to be not significantly different from alongshore uniform. Of the data presented here, 139 (52%) had currents with alongshore variability greater than σ_{crit}.

Scaled alongshore variability (Figure 4.7a) showed a dynamic range of more than an order of magnitude (less than 10% to over 100% alongshore variation of $|\overline{V}|$) over the length of the experiment. A histogram and calculated cumulative probability density of $\overline{\sigma_V / |\overline{V}|}$ (Figure 4.7b) indicates that surf zone currents were

significantly alongshore-variable during much of the experiment, with $\overline{\sigma_V / |\overline{V}|} >$ 0.25(0.5) for 60 (29)% of the observations. A plot of $\overline{\sigma_V / |\overline{V}|}$ versus $|\overline{V}|$ (Figure 4.7c) shows the largest values of $\overline{\sigma_V / |\overline{V}|}$ occur at the smallest alongshore averaged current magnitudes, similar to the observations of *Feddersen and Guza* [2003]. A total of 61 (23%) of the observations passed the combined thresholds for two-dimensional flow conditions, defined here as $\overline{\sigma_V} > \sigma_{crit}$ and $\overline{\sigma_V / |\overline{V}|} > 0.25$.

4.4.3 Combined Results for 1HD Failure

The two criteria for 1HD failure, discussed above, are

$$x'_{\overline{V_m}} < -1 \tag{8a}$$

and

$$\overline{\sigma_V / |\overline{V}|} > 0.25 \quad \cap \quad \overline{\sigma_V} > \sigma_{crit} . \tag{8b}$$

The threshold values chosen are arbitrary, but reasonable. Based on these criteria, it was found that 71% of the data runs (154 out of 218) violate either or both of these assumptions of 1HD dynamics. Of 86 runs when both measures were evaluated, 37 (43%) failed both criteria. This is considerably different from the conclusions of *Ruessink et al.* [2001] and *Feddersen and Guza* [2003] that 1HD dynamics were broadly valid, and may reflect both the increased density of surf zone sampling in this experiment compared to the *in situ* arrays in the previous studies and the wider range of conditions over the 14 months of sampling.

4.4.4 A Proxy for determination of two-dimensionality

As mentioned previously, *Ruessink et al.* [2001] introduced a χ^2 statistical measure of longshore bathymetric variability and investigated the dependence of 1HD model error on the value of χ^2. While this is a relevant measure, the normalization by the mean profile depths emphasizes alongshore variability in shallow water regions, and the measure does not take wave forcing into direct

consideration. Moreover, it is only in rare circumstances that such extensive bathymetry data are available to carry out this calculation (of course, the existence of this data would allow full area models of 2HD dynamics to be found anyway, without need for any assumptions about longshore-uniformity). Even at the Field Research Facility, arguably the most active nearshore field research site in the world, only nine surveys were carried out during the 14-month duration of this experiment. Thus, there is a practical interest in developing an optical proxy to determine the likely validity of 1HD predictions. Here, we test the merit of γ_B as such a proxy.

Comparisons of $x'_{\overline{V_m}}$ with alongshore-bathymetric variability, γ_B, show a marginally significant relationship ($r^2 = 0.04$; Figure 4.8a). Removal of data runs for which wave dissipation over the bar is seaward of the most dense part of OCM array ($\overline{x_R} - \overline{\delta_R}$ >195m) reduced the data set from 165 to 120 points and yielded improved, but still unimpressive, correlation statistics ($r^2 = 0.14$). The majority of points removed occurred between mid-January to mid-March 2004. Comparisons of $x'_{\overline{V_m}}$ with wave direction (not shown) demonstrate no convincing or significant relationship.

The comparison of $\overline{\sigma_V / |\overline{V}|}$ with γ_B is shown in Figure 4.8b. While the relationship is quite scattered, increased $\overline{\sigma_V / |\overline{V}|}$ is associated with larger values of γ_B, ($r^2 = 0.07$, technically significant at the 95% confidence level). For comparison, there is no convincing relationship between α and $\overline{\sigma_V / |\overline{V}|}$, though more complex circulation is expected when waves are closer to normal incidence. A significant relationship exists between a proxy for the alongshore component of wave energy, $H_s^2 |\sin(\alpha)|$, and $\overline{\sigma_V / |\overline{V}|}$ ($r^2 = 0.11$) with $\overline{\sigma_V / |\overline{V}|}$ decreasing with larger values of $H_s^2 |\sin(\alpha)|$, indicating the increased alongshore uniformity of currents

with larger waves (i.e. storms force strong longshore currents). This is consistent with the observations in Figure 4.7c.

While performance of γ_B as a predictor of 1HD failure is weak, its simplicity would make it an attractive proxy that we should further explore. The probability for 1HD failure (equations 8a, b) was calculated from the observations for a range of values of γ_B from 0.1 to 1.3 at intervals of 0.2. Ninety-five percent confidence intervals were computed based on the central limit theorem [*Bethea et al.*, 1995]. For conditions for which γ_B is known, the probability of 1HD failure was calculated (Figure 4.9). For example, for $0<\gamma_B < 0.2$ ($0.2< \gamma_B <0.4$), 75% (56%) of the observed currents should satisfy (i.e. should not violate) a simple 1D model during this experiment. Alternately, a single criterion can be established as a rule of thumb, for example, based on the 50% probability of 1HD failure which maps to $\gamma_B = 0.42$ by Figure 4.9. Thus, values less than this are more than 50% likely to be consistent with 1HD dynamics.

4.5 Mid-surf model comparisons

While profile models provide a detailed prediction of longshore current structure, point models [i.e. *Komar and Inman*, 1970] are easily implemented and are commonplace in engineering applications. Yet the accuracy of these models has not been well tested for the often-variable bathymetry of natural field sites. Here, the Komar and Inman model, equation (1), is tested against measured maximum alongshore-mean currents in this experiment.

Breaking wave height, H_b, and breaking wave angle α_b, both required in (1), are determined by shoaling waves measured at the 8m array to an approximate breaking depth using Snell's Law and assuming conservation of wave energy flux up to breaking [*Dean and Dalrymple*, 1984]. Linear wave theory, straight and parallel contours and depth-limited breaking (equation 4) are assumed. Thus,

$$H_b = H_{rms}^{4/5}\left(\sqrt{\frac{\gamma}{g}}\frac{Cn\cos\alpha}{\cos\alpha_b}\right)^{2/5} \qquad (9a)$$

and

$$\alpha_b = \sin^{-1}\left(\frac{\sin\alpha}{C}\sqrt{\frac{gH_b}{\gamma}}\right), \qquad (9b)$$

where C and n are the phase speed and the group to phase speed ratio, respectively, evaluated at 8m water depth for the measured peak wave period, T_p. Root-mean-square wave height at the 8m array was estimated using $H_{rms} = 0.706H_s$ [*Dean and Dalrymple*, 1984]. Equations (9a) and (9b) were solved iteratively, until the maximum change in α_b was less than 0.1° and H_b changed less than 0.1m.

The comparison of V_{mid} with the observed alongshore-averaged current maximum, $\overline{V_m}$ (Figure 4.10a) demonstrates that V_{mid} is a fair predictor of $\overline{V_m}$ (r^2 = 0.57; rms difference 0.38 m/s). It may seem paradoxical that the observations described earlier suggest that longshore gradients are commonly important to nearshore flows at this site (2HD dynamics are required) yet the simplest point model of Komar and Inman [1970] does a relatively good job predicting peak mean flows. In fact, the observations for this comparison (Figure 4.10a) were based on the peak current not from individual measurements, but instead from the alongshore-mean longshore currents. Thus, values tested were averages from a domain that spanned up to 250m (depending on the number of valid sensors), so longshore gradients were largely averaged out and the simple dynamic balance proposed by *Komar and Inman* [1970] is again valid. For comparison, if all measured values of the peak mean current at all six longshore positions were included in the regression, the r^2 drops to 0.46 and the rms difference increases to 0.43m/s (Figure 4.10b).

4.6 Discussion

Both *Ruessink et al*. [2001] and *Feddersen and Guza* [2003] tested the performance of 1HD models of longshore currents under varying degrees of longshore bathymetric variability. Both papers concluded that 1HD models were valid for most tested conditions. Results presented here, classified according to

two objective criteria, show a much higher rate of 1HD failure (71% of 218 data runs). The sources of these discrepancies deserve discussion and could potentially include the nature of the measurement methods, differences in sampling strategies in space or time, or true variations in beach behavior between the data sets. Each is considered in turn.

Electromagnetic current meters, the primary instrument for the above studies, have been a staple of *in situ* nearshore sampling for three decades. After extensive testing, *Guza et al.* [1988] showed that a properly installed and maintained sensor had small errors, approximately 3 cm/s in bias and 5% in gain (at the 95% confidence level). In the paper describing the OCM technique, *Chickadel et al.* [2003] showed an rms error of 10 cm/s, based on extensive comparison against electromagnetic current meters (under the conservative assumption that the *in situ* sensors were perfect and that all of the discrepancy was associated with the OCM method). To allow for the larger error of the OCM method, a quality control criterion was implemented that limits consideration to only those velocities greater than 20 cm/s. Similarly, measures of the alongshore standard deviation of currents are compared against expected values due to measurement noise to determine if they are significantly different than zero.

OCM data are, by definition, measures of the flow at the water's surface while *in situ* sensors must be continuously covered by water to be valid, so are collected at some depth below the surface. Thus, any vertical shear will yield discrepancies. Similarly, OCM measurements are likely to be more affected by wind stress, a further possible source of shear. Both issues were discussed in the original work by *Chickadel et al.* [2003] and it is important to note that the 10 cm/s confidence interval includes these effects. Moreover, with the exception of section 4 (testing point models of current strength), the present paper is based not on the magnitudes of the observed currents, but instead on their spatial structure (longshore standard deviation and cross-shore location of the peak current) and the likelihood of observed variability to be above expected measurement noise.

Presumably, these quantities are more robust to the above instrumentation issues than would be the actual current strengths.

Finally, OCM sampling is not continuous in time. Since the method relies on foam tracking, values are only returned when foam contrast is detected (so mild conditions are not well sampled). For the purposes of this paper, data must be valid over a large area so that the longshore and cross-shore spatial structure of the currents can be adequately described. A consequence is that only a fraction of the possible data (between 165 and 272 of 817 runs, depending on the test) is considered acceptable. Nevertheless, these results span a large data set by most standards, having been collected over 14 months and over a wide range of conditions.

Perhaps the largest difference between the data presented here and the two previous studies lies in the density of measurements within the surf zone. Animations of hourly time exposure images from the SandyDuck field experiment (available through anonymous ftp at ftp://cil-ftp.coas.oregonstate.edu/pub/outgoing/cchickad/SandyDuckMovie.mov) show that the surf zone was narrow, typically contained in the region $x < 200$m. Only 5 of the 30 *in situ* sensors were located in this region, compared to the current study where 20 of the 28 OCM sensors were located shoreward of the surf zone. The images also show that the sand bar morphology during both the SandyDuck experiment and the period under examination here was commonly alongshore variable and, at times, quite complex. Thus, the concentration of OCM instruments close to shore make this array better able to resolve the day-to-day structure of the surf zone. In contrast, the SandyDuck measurements were weighted further offshore and could only resolve the surf zone in detail during very large wave events when morphologies and dynamics are commonly observed to become longshore uniform [*Lippmann and Holman*, 1990].

The χ^2 statistical measure of longshore bathymetric variability introduced by *Ruessink et al.* [2001] shows power for predicting 1HD failure but requires the availability of dense bathymetric data. The metric discussed in this paper, γ_B, is

quite different in that it is an optically-based measure (so is easily available) and that it is a proxy measure of the longshore variability in roller dissipation, the primary forcing for nearshore flows [*Aarninkhof and Ruessink*, 2004]. Furthermore, normalization in γ_B by $\overline{\delta_R}$ makes this measure independent of depth or distance from the shoreline. Examples of time-averaged dissipation patterns and the corresponding values of γ_B (Figure 4.11) provide empirical evidence of the good performance of the metric. In practice (section 3.4 and Figure 4.9), however, we find only a very weak linear relationship between longshore current spatial variability and γ_B, similar to the evidence provided by *Ruessink et al*. [2001].

Anomalies in time exposure images such as alongshore gaps in breaking or strong variations in breaking location have often been hypothesized to be signatures of rip currents, although little direct evidence has been presented to support this claim. However, data on the convergence of longshore flows can be used to test this idea. Time-averaged cross-shore velocity U_c can be calculated at discreet locations within the OCM alongshore sub-array assuming steady state flow, no cross-shore flow at the shoreline and conservation of mass

$$U_c = \frac{1}{h}\int_{x_0}^{x} \frac{-\partial Vh}{\partial y}\,dx \qquad (10)$$

where x_0 is the cross-shore location of the most onshore OCM in the array. Circulation vectors are estimated by interpolating V and U_c to common grid locations. For lack of appropriate measurements of water depth, h is assumed to be the 16-year average alongshore-uniform profile (section 2.3). For one data run of particularly complex morphology, 17 April, 2004, a CRAB survey was available and the calculation could be carried out using the full bathymetry. Comparison of the cross-shore currents calculated with the full bathymetry and those found for the long-term averaged profile showed an rms difference of only 0.04 m/s, so the lack of accurate bathymetry appears to have little effect on the computed cross-shore flows.

Figure 4.11 shows eight examples of uniform and complex circulation throughout the experiment. Rip currents in these examples occurred near offshore deviations in the bar position (inferred from visual breaking patterns) when alongshore non-uniformity was large ($\gamma_B > 0.5$), consistent with the common interpretation of Argus images and with the idea of bathymetric controls on rip current locations. These first-ever observations provide evidence that local non-uniformities in the time-averaged wave-breaking pattern (i.e. local deviations in the bar, dark channels through the surf zone, and streak lines of foam outside of the surf zone) are actually visual evidence of rip currents.

Compared with the statistics presented in most of this paper, the good agreement of the Komar and Inman longshore current model with alongshore-averaged maximum currents is striking. It is clear that significant alongshore-averaging (in this case, over 250m) minimizes the effect of local alongshore-nonuniform forcing, thus any bathymetry influence, and the remaining forces, alongshore radiation stress and bottom friction, balance each other. This reduction of the momentum equation to a 1D balance, for alongshore averaged currents, has a host of benefits, particularly to the engineering and management end user. Primarily, the use of a simple sediment transport model [e.g. *Komar and Inman*, 1970] holds promise for accurately and easily predicting larger scale (>O(100m)) alongshore sediment transport patterns using only wave height and angle information. Gains from a more complex 1HD or higher order model comes at the cost of having to collect extensive wave and bathymetry measurements.

4.7 Conclusions

Fourteen months of optically-derived alongshore current measurements were recorded from a 28-element two-dimensional array at Duck, NC, in order to test the validity of one-dimensional (1HD) forcing assumptions of longshore currents. Since bathymetry data were not available, currents were not directly compared to models. Instead, determination of failure of 1HD dynamics was based

on two criteria: a) observation of significant longshore variability of longshore currents ($\overline{\sigma_V / |\overline{V}|} > 0.25$ and $\overline{\sigma_V} > \sigma_{crit}$, where $\overline{\sigma_V}$ and $\overline{V}$ are the longshore standard deviation and longshore mean of the longshore current, and σ_{crit} is the maximum value of $\overline{\sigma_V}$ considered to be due to measurement noise alone), and b) observation of a significant shoreward lag between the location of the maximum current and the location of active roller dissipation. In contrast to previous papers, observations presented here suggest 1HD model assumptions were found to be valid only 29% of the time (64 cases out of 218). An optically-derived scaling proxy for alongshore bathymetric variability, γ_B, was found to be only weakly correlated to the statistics of IHD dynamics failure. For specific values, the probably of 1HD dynamics success can be predicted from a graph, but for a general case, for γ_B values less than 0.42, 1HD dynamics are more than 50% likely to be appropriate. A simple point model of mid-surf longshore currents due to *Komar and Inman*, [1970] was found to reasonably predict the maximum alongshore-averaged longshore current ($r^2 = 0.57$, rms error = 0.38 m/s). Cross-shore flows, calculated from longshore current divergence, showed the common occurrence of complex circulation patterns and demonstrated that anomalies in optical proxies for bar position such as gaps or offshore bulges in breaking patterns are associated with rip currents.

4.8 References

Aarninkhof, S.G.J., and B.G. Ruessink (2004), Video observations and model predictions of depth-induced wave dissipation, IEEE Transactions on Geoscience and Remote Sensing, 42 (11), 2612-2622.

Alexander, P.S., and R.A. Holman (2004), Quantitative analysis of nearshore morphological variability based on video imaging, Marine Geology, 208 (1), 101-111.

Bates, D., M, and D.G. Watts, Nonlinear Regression Analysis and Its Applications, John Wiley & Sons, New York, 1988.

Bethea, R.M., B.S. Duran, and T.L. Boullion, Statistical methods for engineers and scientists, 652 pp., Marcel Dekker Inc., New York, 1995.

Bowen, A.J. (1969), The generation of longshore currents on a plane beach, Journal of Marine Research, 27, 206-215.

Chickadel, C.C., R.A. Holman, and M.F. Freilich (2003), An optical technique for the measurement of longshore currents, Journal of Geophysical Research, 108 (C11), 3364.

Church, J.C., and E.B. Thornton (1993), Effects of breaking wave induced turbulence within a longshore current model, Coastal Engineering, 20, 1-28.

Dean, R.G., and R.A. Dalrymple, Water wave mechanics for scientists and engineers, 353 pp., Prentice-Hall Inc., Englewood Cliffs, NJ, 1984.

Feddersen, F., and R.T. Guza (2003), Observations of nearshore circulation: Alongshore uniformity, Journal of Geophysical Research, 108 (C1), 3006.

Feddersen, F., R.T. Guza, and S. Elgar (2004), Inverse modeling of one-dimensional setup and alongshore current in the nearshore, Journal of Physical Oceanography, 43 (4), 920-933.

Guza, R.T., M.C. Clifton, and F. Rezvani (1988), Field intercomparisons of electromagnetic current meters, Journal of Geophysical Research, 93 (C8), 9302–9314.

Haller, M.C., R.A. Dalrymple, and I.A. Svendsen (2002), Experimental study of nearshore dynamics on a barred beach with rip channels, J. Geophys. Res., 107 (C6), doi:10.1029/2001JC000955.

Holland, K.T., R.A. Holman, T.C. Lippmann, J. Stanley, and N. Plant (1997), Practical use of video imagery in nearshore oceanographic field studies, IEEE Journal of Ocean Engineering, 22 (1).

Komar, P.D., and D.L. Inman (1970), Longshore sand transport on beaches, Journal of Geophysical Research, 75, 5914-5927.

Komar, P.D., and J. Oltman-Shay, Nearshore Currents, in Handbook on Coastal and Ocean Engineering, edited by J.B. Herbich, pp. 651-680, Gulf Publishing Co., Houston, TX, 1990.

Lippmann, T.C., and R.A. Holman (1989), Quantification of sand bar morphology: A video technique based on wave dissipation, Journal of Geophysical Research, 94 (C1), 995-1011.

Lippmann, T.C., and R.A. Holman (1990), The spatial and temporal variability of sand bar morphology, Journal of Geophysical Research, 95 (C7), 11,575-11,590.

Long, C.E., and J.M. Oltman-Shay, (1991), Directional characteristics of waves in shallow water, Coastal Eng. Res. Cent., Field Res. Facil., U. S. Army Eng. Waterw. Exp. Sta., Vicksburg, Miss.

Long, J.W., and H.T. Özkan-Haller (2005), Offshore controls on nearshore rip currents, Journal of Geophysical Research, 110 (C12007).

Longuet-Higgins, M.S., and R.W. Stewart (1964), Radiation stresses in water waves; a physical discussion, with applications, Deep-Sea Research, 11, 529-562.

Longuet-Higgins, M.S. (1970), Longshore currents generated by obliquely incident sea waves, 2, Journal of Geophysical Research, 75, 6790-6801.

Plant, N.G., R.A. Holman, and M.H. Freilich (1999), A simple model for interannual sand bar behavior, Journal of Geophysical Research, 104 (C7), 15755-15776.

Plant, N.G., K.T. Holland, and J.A. Puleo (2002), Analysis of the scale of errors in nearshore bathymetric data, Marine Geology, 191 (1), 71-86.

Putrevu, U., J. Oltman-Shay, and I.A. Svendsen (1995), Effect of alongshore nonuniformities on longshore current predictions, Journal of Geophysical Research, 100 (C8), 16119-16130.

Reniers, A.J.H.M., E.B. Thornton, and T.C. Lippmann, (1995), Longshore currents over barred beaches, in Coastal Dynamics '95, pp. 413-424, Am. Soc. of Civ. Eng., New York.

Reniers, A.J.H.M., and J.A. Battjes (1997), A laboratory study of longshore currents over barred and non-barred beaches, Coastal Engineering, 30 (1), 1-21.

Ruessink, B.G., J.R. Miles, F. Feddersen, R.T. Guza, and S. Elgar (2001), Modeling the alongshore current on barred beaches, Journal of Geophysical Research, 106 (C10), 22451-22464.

Sallenger, A.H., Jr., and R.A. Holman, Wave-energy saturation on a natural beach of variable slope, in Journal of Geophysical Research, pp. 11,939-11,945, 1985.

Sancho, F.E., I.A. Svendsen, A.R.V. Dongeren, and U. Putrevu, (1995), Longshore nonuniformities of nearshore currents, in Coastal Dynamics '95, pp. 425-436, Am. Soc. of Civ. Eng., New York.

Slinn, D.N., J.S. Allen, and R.A. Holman (2000), Alongshore currents over variable beach topography, Journal of Geophysical Research, 105 (C7), 16971-16998.

Smith, J.M., M. Larson, and N.C. Kraus (1993), Longshore current on a barred beach: Field measurements and calculation, Journal of Geophysical Research, 98 (C12), 22,717-22,731.

Svendsen, I.A. (1984a), Mass flux and undertow in a surf zone, Coastal Engineering, 8, 347-365.

Svendsen, I.A. (1984b), Wave heights and set-up in a surf zone, Coastal Engineering, 8, 303-329.

Thornton, E.B., and R.T. Guza (1986), Surf zone longshore currents and random waves: Field data and models, Journal of Physical Oceanography, 16 (7), 1165-1178.

van Enckevort, I.M.J., and B.G. Ruessink (2001), Effect of hydrodynamics and bathymetry of video estimates of nearshore sand bar position, Journal of Geophysical Research, 106 (C8), 16,969 - 16,979.

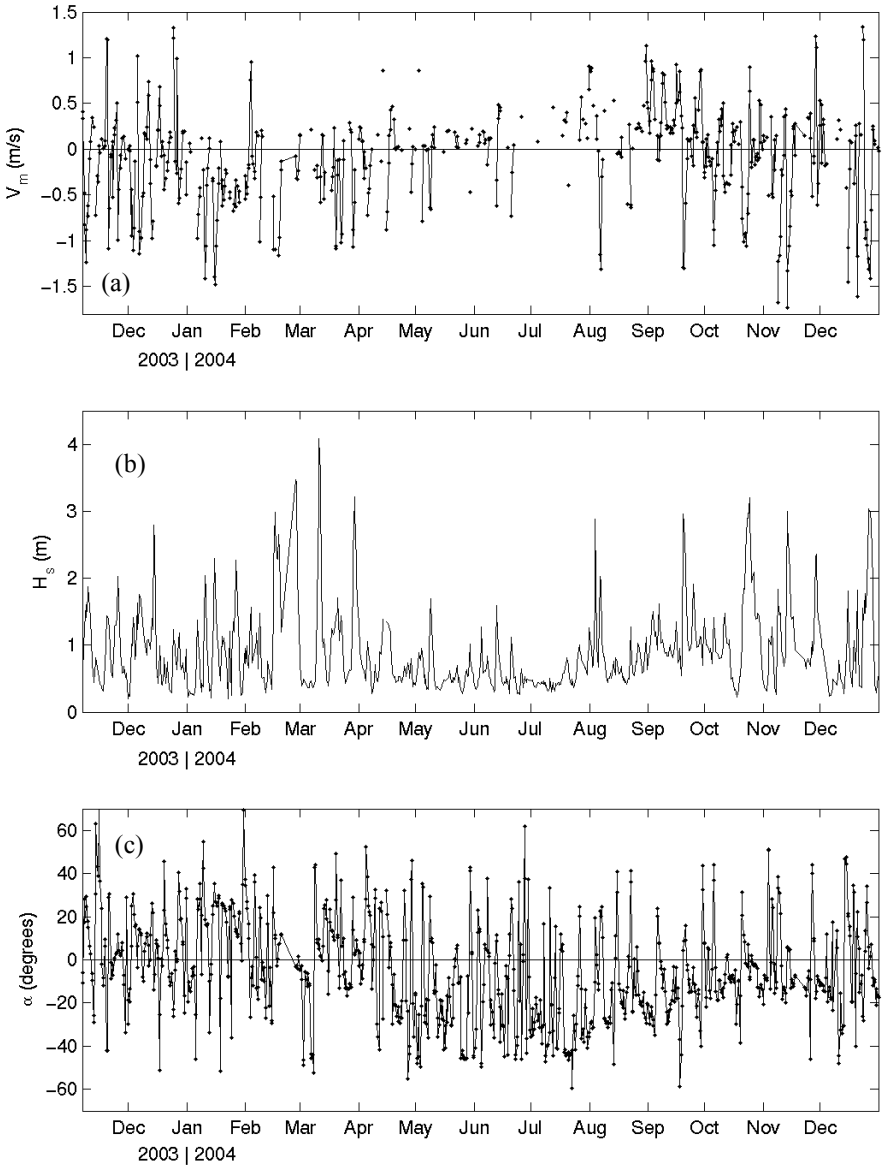

Figure 4.1 (a) Maximum observed longshore currents (discussed in section 4.3.1-2) indicated by the dots connected by lines for contiguous observations, (b) significant wave height and (c) peak wave direction during the 14 month experiment measured at the 8m array, where positive directions indicate waves coming from north of shore normal.

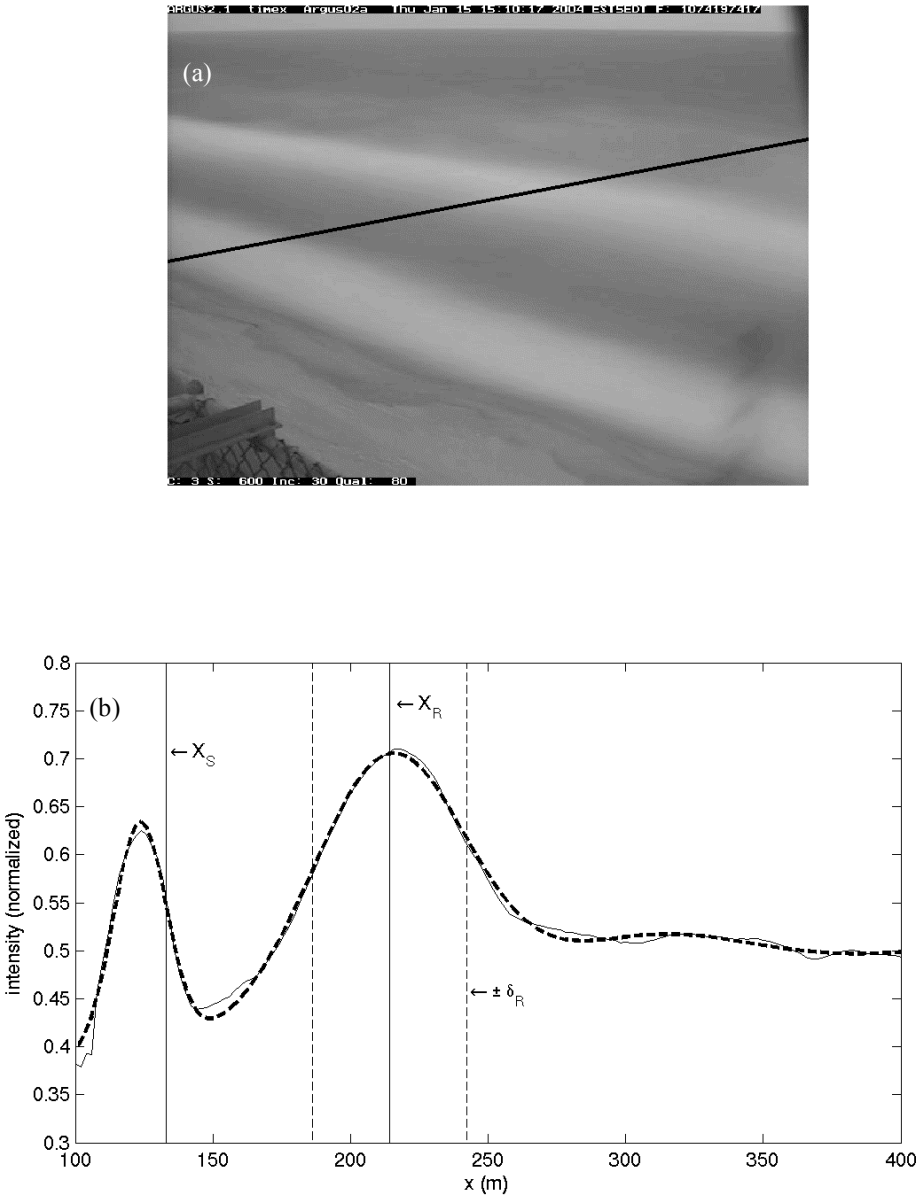

Figure 4.2 (a) A 10-minute time-averaged image looking northeast at the beach at Duck. Bright areas indicate regions of preferential breaking at the shoreline and over a sand bar. The line indicates where a cross-shore transect of image intensity was sampled. (b) The roller dissipation model (bold dashed line) fit to the intensity profile (thin line) sampled from the image in (a). The modeled locations of the extent and position of the breaking over the bar, and the shoreline are indicated.

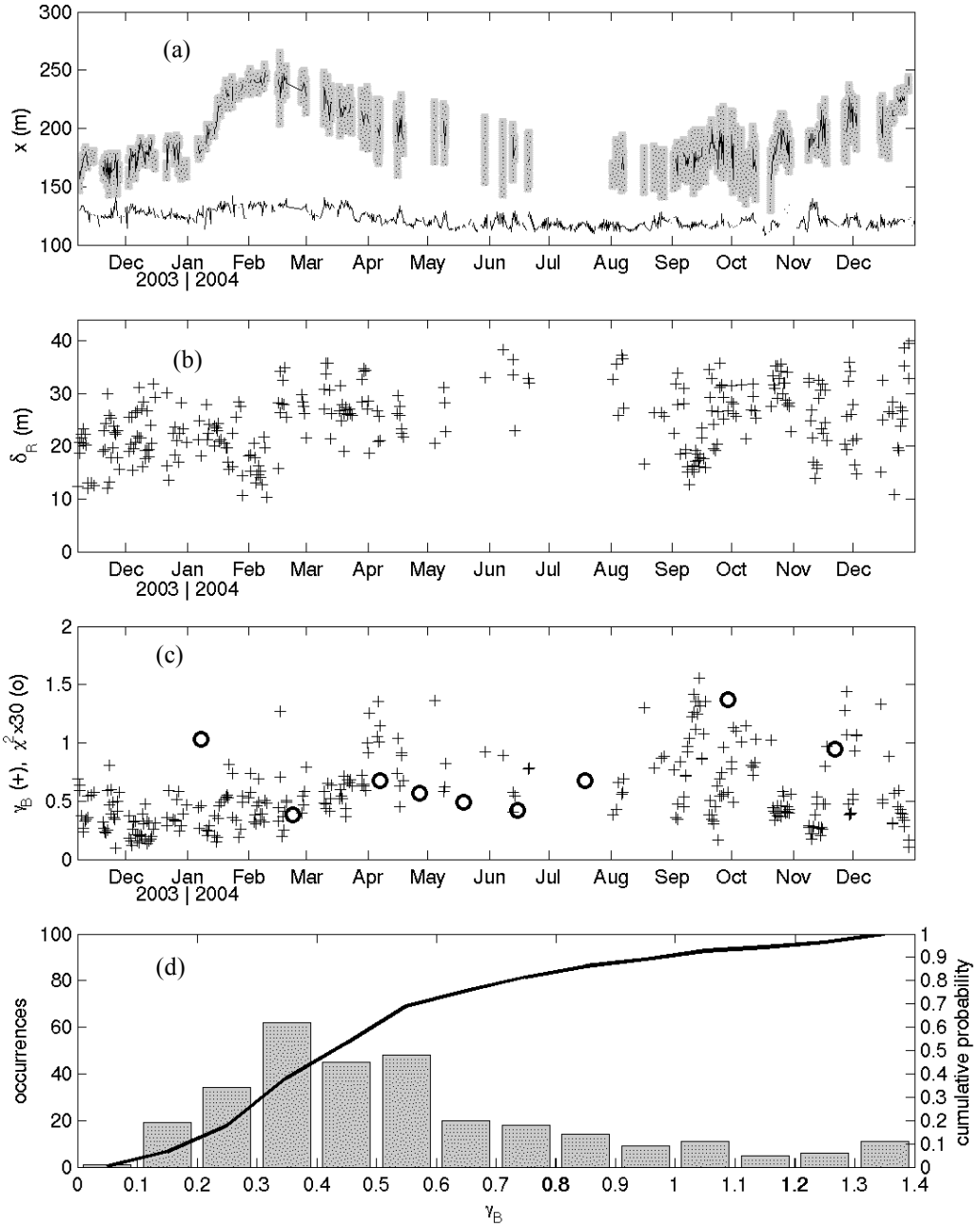

Figure 4.3 (a) Timeline of the alongshore mean shoreline position (line), mean bar location and ±one standard deviation of position (line with gray bars, respectively). (b) Timeline of the alongshore average half-width of breaking over the bar, δ_R. (c) Timeline of the proxy γ_B (pluses, section 2.2) of alongshore variable bathymetry, and the alongshore bathymetry variability metric, χ^2 (circles, section 1), derived from periodic bathymetry surveys. (d) The cumulative distribution (line) and histogram (bars) of γ_B.

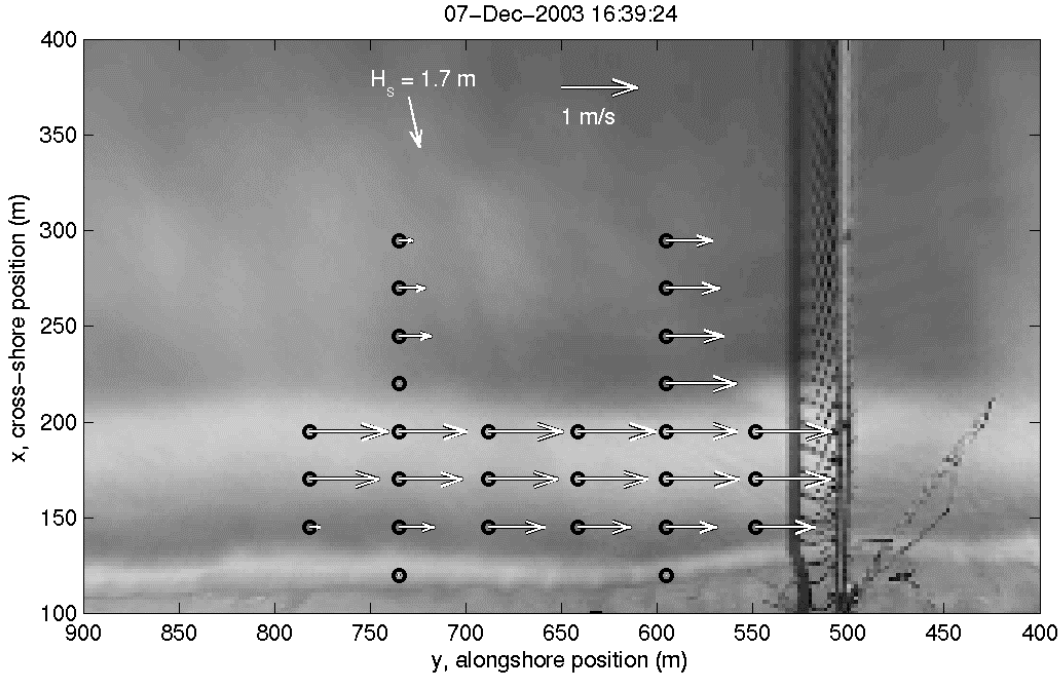

Figure 4.4 OCM array (centers at the circles) displayed on a rectified time exposure image. Alongshore current vectors, wave direction and wave height for an example day are also shown. The FRF pier and its shadow are unmistakable in the image at y = 510m. The deck of the pier is skewed from the real world position due to perspective distortion.

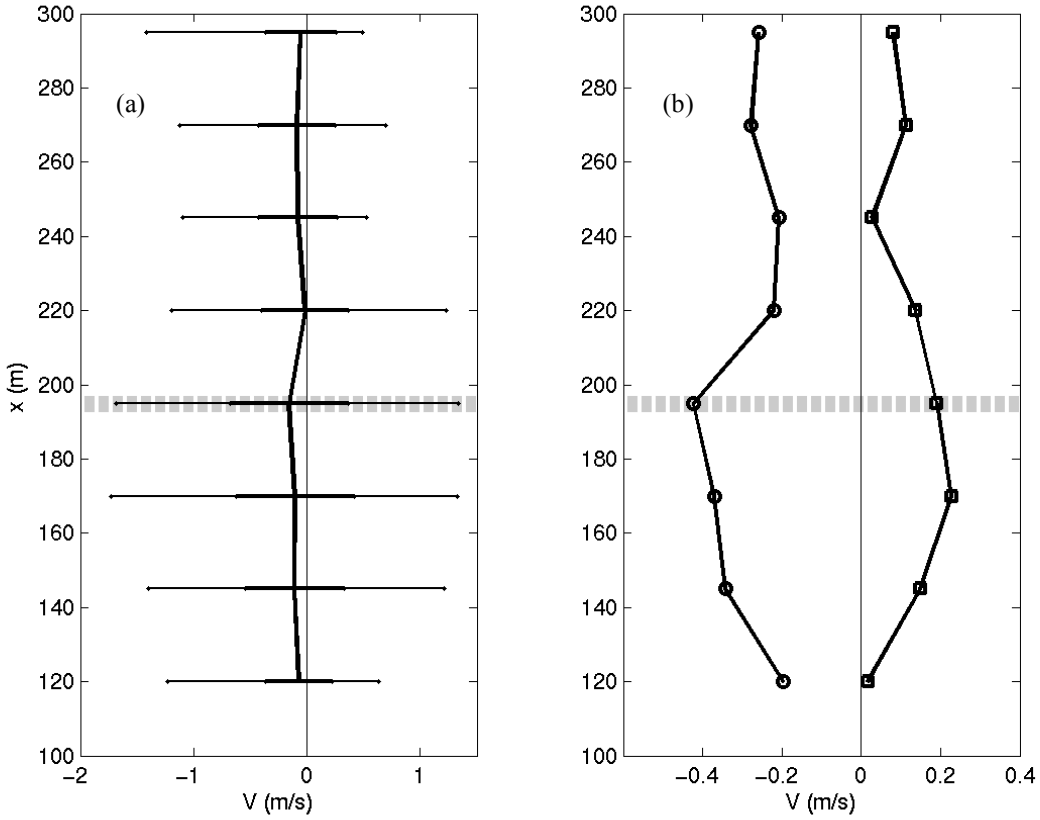

Figure 4.5 (a) Statistics of the alongshore averaged current during the experiment including: mean (thick line), standard deviation (thick horizontal lines) and extremes (thin horizontal lines). (b) Average longshore current profiles for instances of wave directions from the north (circles) and south (squares). The time averaged alongshore-mean bar position is shown as the horizontal dashed gray line in both plots.

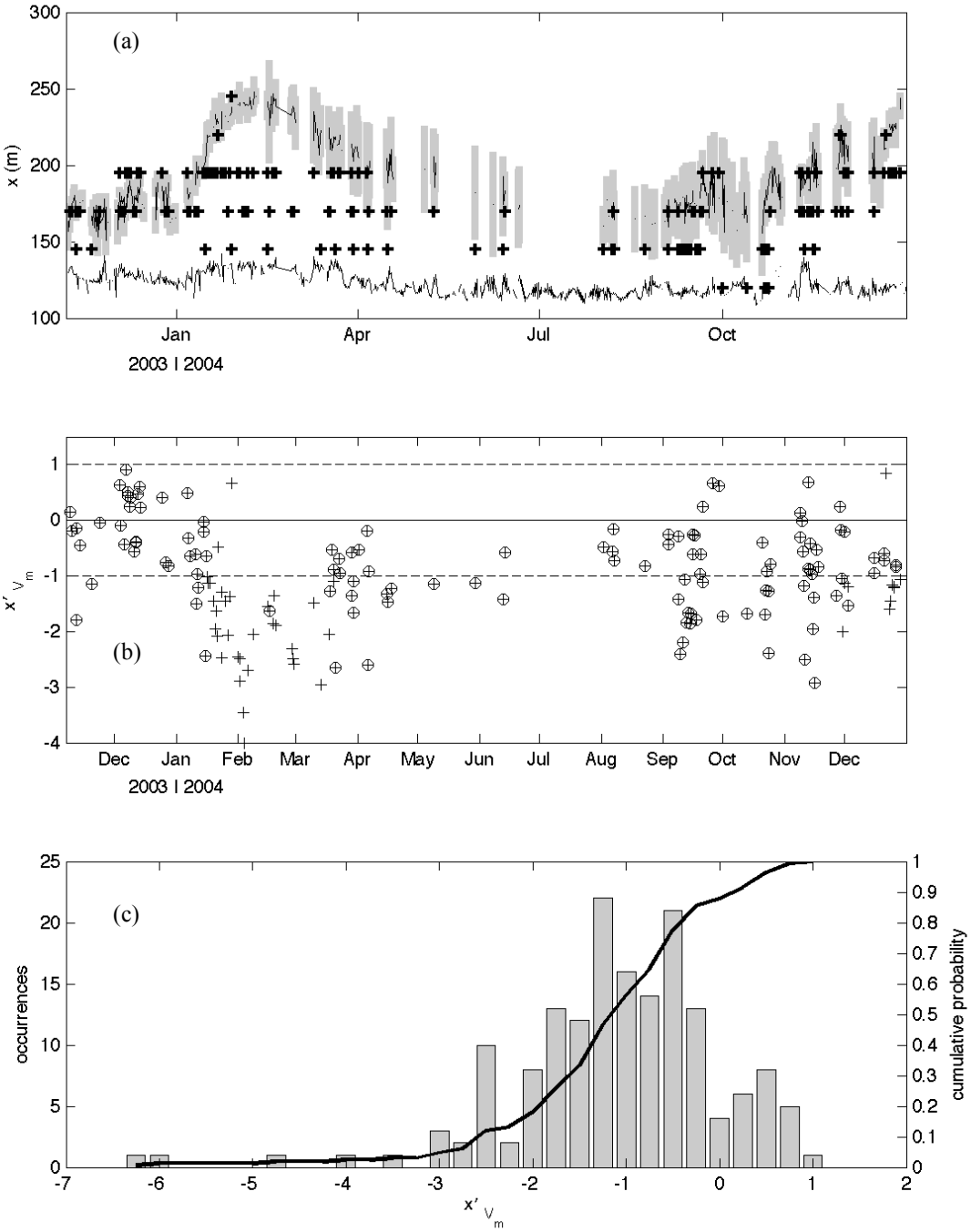

Figure 4.6 (a) Sandbar and shoreline positions, identical to Figure 4.3a, with cross-shore locations of maximum current plotted (+). (b) Scaled longshore current maxima positions. Circled points indicate instances of the shoreward edge of the bar dissipation inshore of x =195m (see section 4.3.1). (c) Histogram and cumulative probability distribution of normalized Vm positions.

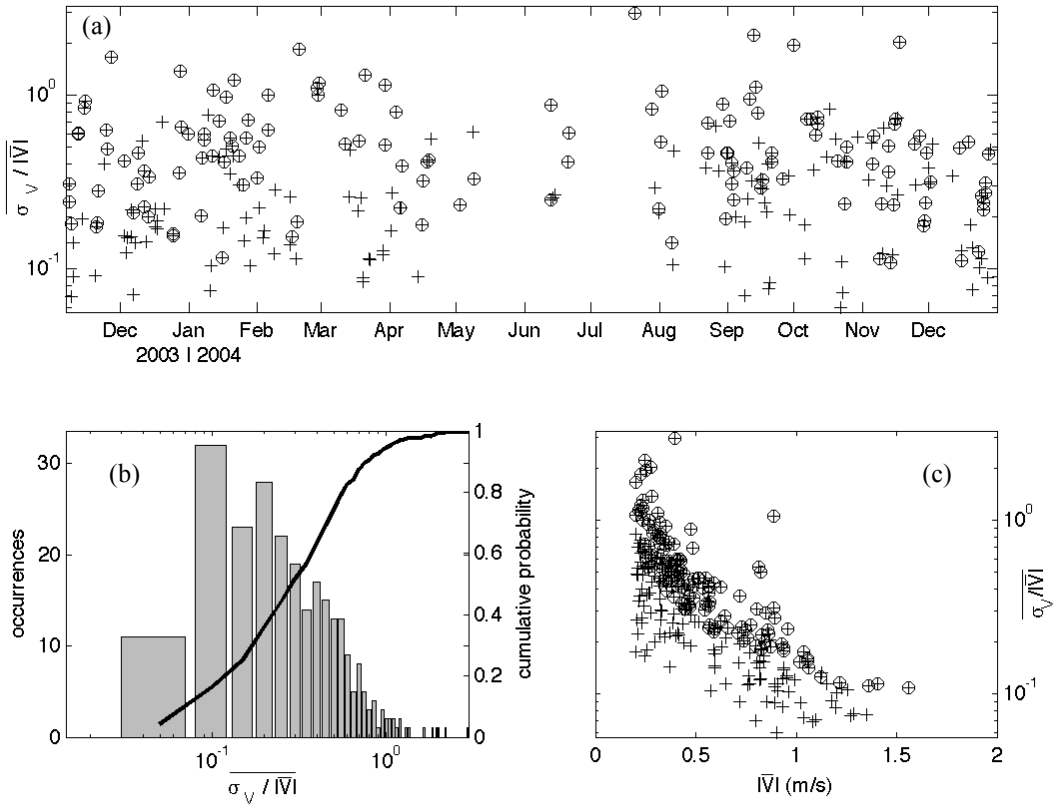

Figure 4.7 (*a*) Time series of alongshore current variability $\overline{\sigma_V / |\overline{V}|}$ (+) with values greater than expected noise indicated by circles. (*b*) Histogram (line) and cumulative probability distribution (bars) of alongshore current variability observed from November 2003 to December 2004. (*c*) $\overline{\sigma_V / |\overline{V}|}$ plotted against the alongshore average current magnitude $|\overline{V}|$. Circled points indicate $\overline{\sigma_V / |\overline{V}|}$ greater than expected noise in the measurements (as in *a*, see section 4.3.2).

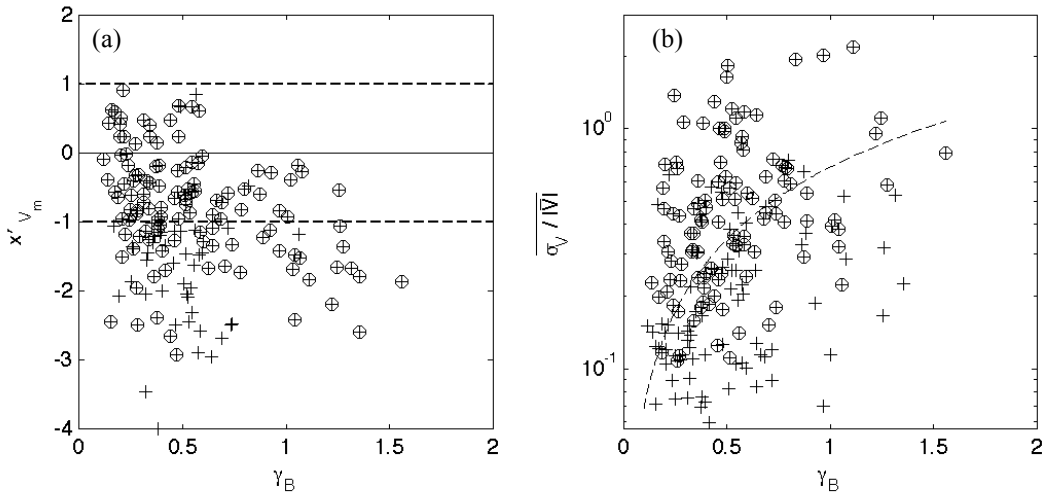

Figure 4.8 (*a*) Scaled longshore current maxima positions versus γ_B. Dashed lines are identical to those shown Figure 4.6b. Circled points indicate instances of the shoreward edge of the bar dissipation inshore of x =195m (see section 4.3.1). (*b*) Semi-log plot of longshore current variability versus γ_B. Circled values indicate measurements greater than expected instrument noise, and the dashed line is a linear regression through all points, forced through the origin (see section 4.3.2).

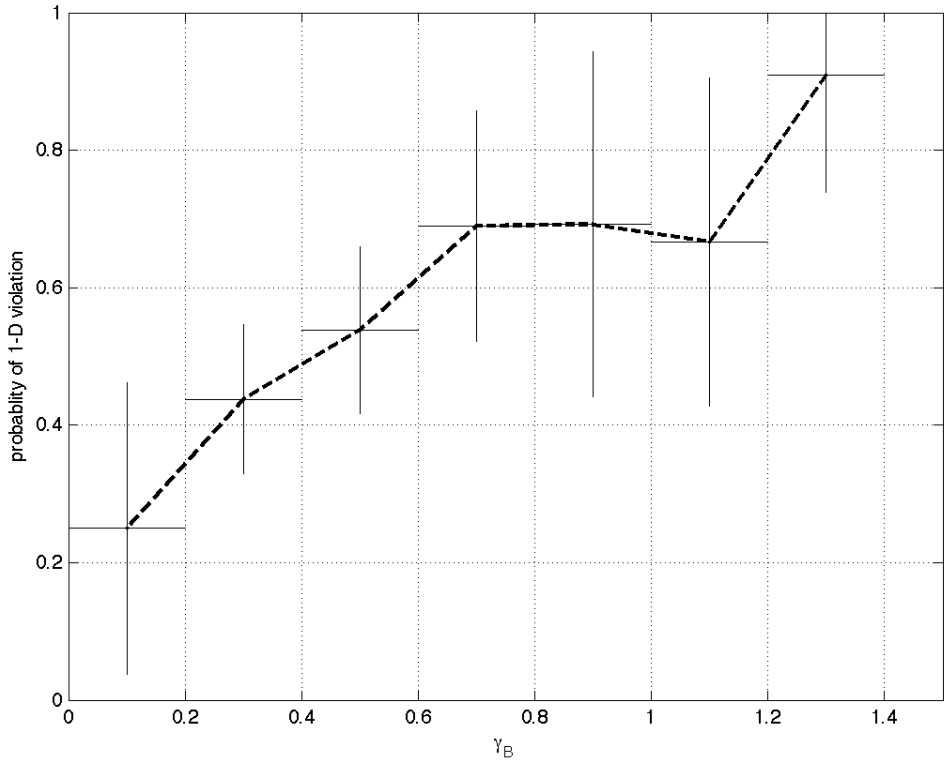

Figure 4.9 The calculated likelihood of violation of 1D assumptions based on observations of increased alongshore current variability and observations of longshore current maxima shoreward of visible breaking (dashed line; see section 4.3.4 for an explanation), with 95% confidence intervals (vertical lines), and bin widths (horizontal lines) indicated.

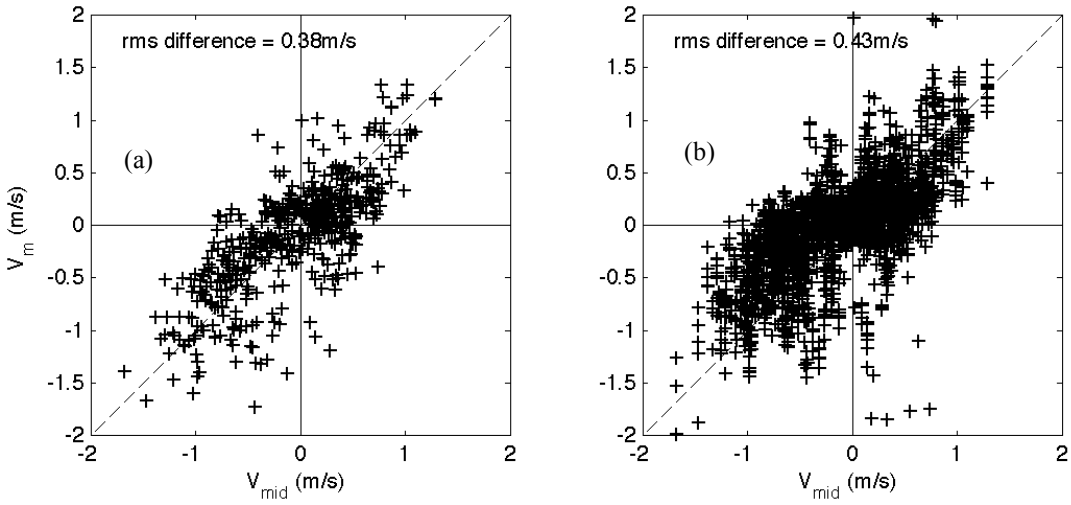

Figure 4.10 (*a*) A regression of the predicted "mid-surf" longshore current, $V_{mid,}$ with the maximum value of alongshore averaged current profile, V_m. (*b*) A regression of the observed longshore current maxima at each alongshore position in current meter array shows increased scatter. The root-mean-square difference between measured and modeled currents is indicated for both cases.

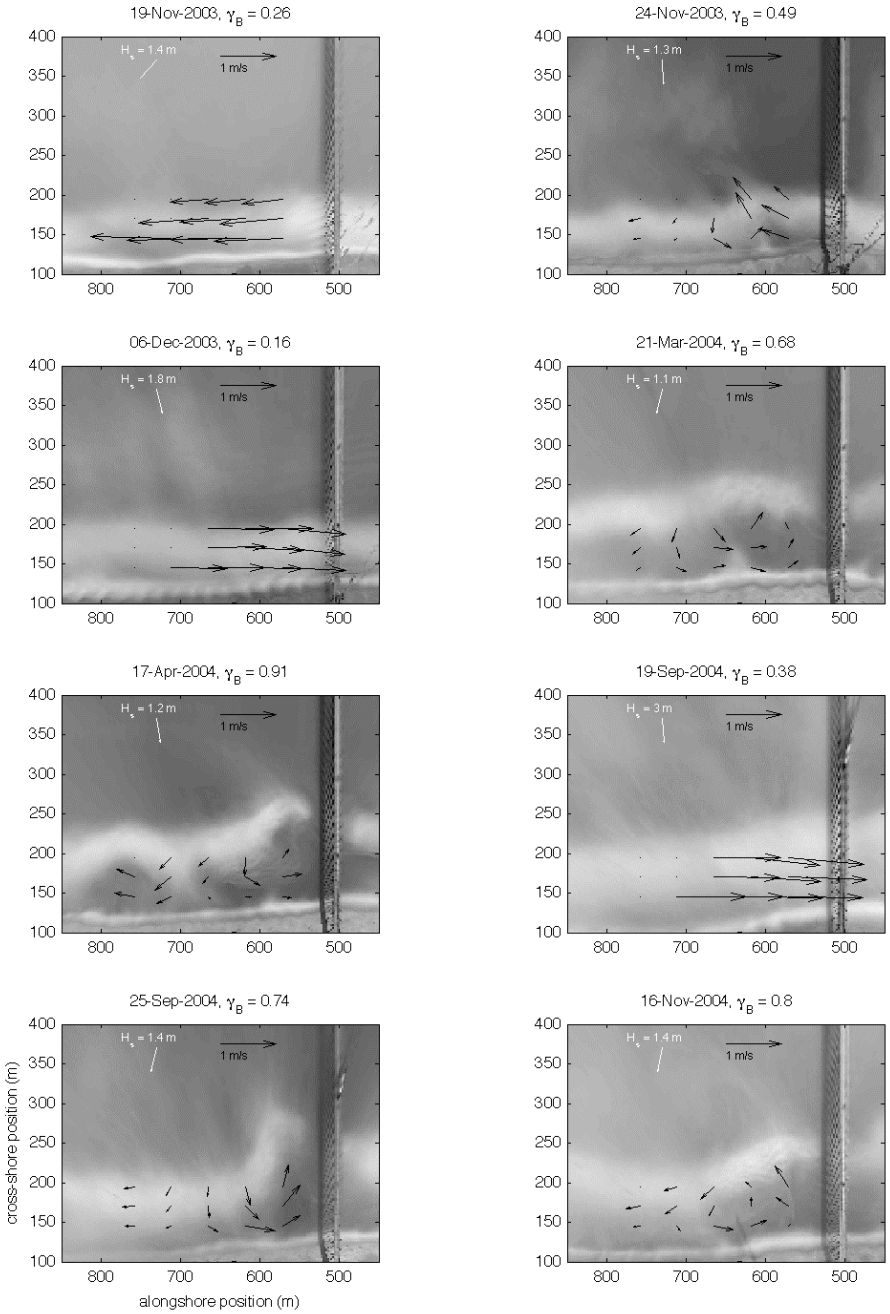

Figure 4.11 Eight examples of complex and alongshore-uniform circulation (black arrows) and rip currents identified from the calculated 2D current field (see section 4.4) shown with their respective time averaged intensity images. Wave direction and significant wave height are indicated in each panel in white, and the date and bathymetry uniformity statistic, γ_B, is indicated above each example. Significant offshore flow is located at offshore deviations in bar location and corresponds to higher values of γ_B (i.e. increased bathymetric variability).

Chapter 5: Conclusions

Waves and currents force sediment transport and cause the inevitable erosion and accretion of the beach face. The resulting fluctuation of the shoreline is a primary concern for resource managers, and the ability to plan for shoreline change will become more important as the economic, environmental and societal demands on beaches, coasts and the nearshore systems of the world increase. Management decisions, therefore, ultimately hinge on the predictive understanding of the fluid-sediment system. The dynamics driving waves and currents are thought to be well understood, yet simpler models, generally those that assume simple (alongshore uniform) bathymetry and linearized force balances, are not applicable for all conditions. More comprehensive models for waves and currents over complex bathymetry exist, yet assessment of these models has proven difficult because of the lack of appropriate data to test them.

Optical remote sensing, as an inexpensive and accessible tool, has been used increasingly in the nearshore for the last two decades. The energetic nearshore environment practically limits the duration and number of *in situ* measurements that can be made, but optical remote sensing can provide both wide and dense spatial sampling (centimeters to kilometers) for a range of time scales (seconds to years). Waves and currents have visible signatures that can be exploited to make quantitative measurements unobtainable by *in situ* instruments. This dissertation has presented successful optically based measurement methods and important observations addressing the general character of waves and currents over spatially variably bathymetry in the nearshore.

The optical wave spectral estimation technique is robust and can provide simple and reliable estimations of nearshore wave direction and frequency spectral shape for unbroken waves. Synthetic tests showed the technique was able to accurately estimate the true directional shape, peak directions, and even resolve

closely spaced bimodal directional distributions. Results were practically independent of the optical sky dome radiance model used, suggesting a wide range of sky conditions which the method may be applied.

Ground truth tests using *in situ* (PUV) and optical data measured during the 2003 Nearshore Canyon Experiment show good agreement. Correlations of the frequency spectra were high, with an average peak frequency difference of only 0.002 Hz. The peak optical and PUV direction, at the peak frequency bands, showed close agreement, with only 5° standard deviation. Directional spreading widths for PUV spectra were 52% wider than optical spectra, and allowed for the observation of bimodal direction spectra (with peak separations of ~15°) at the southern end of the NCEX study site in the optical data. The bimodal pattern was not apparent in the PUV derived spectra.

By applying a grid of tessellated optical alpha arrays, first ever measurements of the large scale, O(100m-1000m), directional wave field offered synoptic views of directional changes over complex bathymetry. Examples of the wave field during the 2003 Nearshore Canyon Experiment show frequency dependence of the directional spectra including focusing and de-focusing by local bathymetry features. However, only lower frequency waves, less than 0.1 Hz, are noticeably affected by the deeper offshore bathymetry, and higher frequency waves appear to respond more to shallow bathymetry away from the influence of the canyon. Calculated divergence maps showed alternating bands of divergence and convergence approximately 100-200m in length in the alongshore direction. The divergence bands, which force frequent rip currents, therefore determine the character of the nearshore circulation. Bimodal directional spectra, described earlier, were also ubiquitous in the wave field.

Finally, a long-term study of the spatial variability of longshore currents over variable and often complex surf zone bathymetry was conducted at Duck NC. The purpose was to test the validity of one-dimensional (1HD) forcing assumptions of longshore currents. Longshore currents were recorded from a 28-element, two-

dimensional array of optical current meters. Since bathymetry data were not available, currents were not directly compared to models. Instead, determination of failure of 1HD dynamics was based on a measure of the longshore variability of longshore currents, and the degree of shoreward lag between the location of the maximum current and the location of the peak in wave forcing. In contrast to previous papers, observations presented here suggest 1HD model assumptions were found to be valid only 29% of the time. An optically-derived scaling proxy for alongshore bathymetric variability was found to be only weakly correlated to the statistics of IHD dynamics failure. A simple point model for mid-surf longshore currents due to wave forcing alone was found to reasonably predict the maximum alongshore-averaged longshore current (rms error of 0.38 m/s). Cross-shore flows, calculated from longshore current divergence, showed the common occurrence of complex circulation patterns and demonstrated that anomalies in optical proxies for bar position such as gaps or offshore bulges in breaking patterns are associated with rip currents.

An important future extension of the results of optically measured waves and currents will be to test and verify wave and circulation models over general bathymetry. Several modes of incorporation of optical data can be imagined, but comparison of modeled output waves and currents with optically derived observations is a first step. With the large potential volume of remotely sensed and modeled data some reduced set of representative variables to compare will have to be explored. For example, comparisons of wave spectra on a one-by-one basis are not useful when there may be a few hundred observations. Similarly, with longshore current measurements, products such as temporal means and variability are more likely to be compared. Additionally, optically measured longshore currents represent surface velocities, whereas models may only predict depth averaged quantities or may be otherwise limited in their vertical resolution, thus comparisons will have to be made carefully. The most exciting future application of optically measured waves and currents will be assimilation in to large-scale

process models. Newly emerging community models for nearshore physical processes, which includes the ultimate end product of sediment transport and beach morphology change, could benefit from assimilation. In this approach, regularly measured waves and currents would provide small corrections to the models, in the same way that meteorological stations scattered across the world aid in near-term weather predictions.

Bibliography

Aarninkhof, S., and R.A. Holman (1999), Monitoring the nearshore with video, *Backscatter*, *10* (2), 8-11.

Aarninkhof, S.G.J., and B.G. Ruessink (2004), Video observations and model predictions of depth-induced wave dissipation, *IEEE Transactions on Geoscience and Remote Sensing*, *42* (11), 2612-2622.

Aarninkhof, S.G.J., B.G. Ruessink, and J.A. Roelvink, (2005), Nearshore subtidal bathymetry from time-exposure video images, in *Journal of Geophysical Research*.

Alexander, P.S., and R.A. Holman (2004), Quantitative analysis of nearshore morphological variability based on video imaging, *Marine Geology*, *208* (1), 101-111.

Bates, D., M, and D.G. Watts, *Nonlinear Regression Analysis and Its Applications*, John Wiley & Sons, New York, 1988.

Bethea, R.M., B.S. Duran, and T.L. Boullion, *Statistical methods for engineers and scientists*, 652 pp., Marcel Dekker Inc., New York, 1995.

Bowen, A.J. (1969), The generation of longshore currents on a plane beach, *Journal of Marine Research*, *27*, 206-215.

Capon, J., R.J. Greenfield, and R.J. Kolker (1967), Multidimensional maximum-likelihood processing of a large apeture seismic array, *Proceedings of the IEEE*, *55*, 192-211.

Capon, J. (1969), High-resolution frequency-wavenumber spectrum analysis, *Proceedings of the IEEE*, *57*, 1408-1418.

Chapman, R.D. (1981), Visibility of rms slope variations on the sea surface, *Applied Optics*, *21* (11), 1959-1966.

Chapman, R.D., and G.B. Irani (1981), Errors in estimating slope spectra from wave images, *Applied Optics*, *20* (20), 3645-3652.

Chickadel, C.C., R.A. Holman, and M.F. Freilich (2003), An optical technique for the measurement of longshore currents, *Journal of Geophysical Research*, *108* (C11), 3364.

Chickadel, C.C., and R.A. Holman (in preparation), Optical estimation of nearshore directional wave spectra, *Journal of Geophysical Research*.

Church, J.C., and E.B. Thornton (1993), Effects of breaking wave induced turbulence within a longshore current model, *Coastal Engineering*, *20*, 1-28.

Cox, C., and W. Munk (1954), The measurement of the roughness of the sea surface from photographs of the sun's glitter, *Journal of the Optical Society of America*, *44*, 838-850.

Davis, R.E., and L.A. Regier (1977), Methods for estimating directional wave spectra from multi-element arrays, *Journal of Marine Research*, *5* (3), 453-477.

Dean, R.G., and R.A. Dalrymple, *Water wave mechanics for scientists and engineers*, 353 pp., Prentice-Hall Inc., Englewood Cliffs, NJ, 1984.

Dugan, J.P., G.J. Fetzer, J. Bowden, G.J. Farruggia, J.Z. Williams, C.C. Piotrowski, K. Vierra, D. Campion, and D.N. Sitter (2001a), Airborne optical system for remote sensing of ocean waves, *Journal of Atmospheric and Oceanic Technology*, *18* (7), 1267-1276.

Dugan, J.P., C.C. Piotrowski, and J.Z. Williams (2001b), Water depth and surface current retrevials from airborne optical measurements of surface gravity wave dispersion, *Journal of Geophysical Research*, *106* (C8), 16903-16915.

Elgar, S., R.T. Guza, and M.H. Freilich (1993), Observations of nonlinear interactions in directionally spread shoaling surface gravity waves, *Journal of Geophysical Research*, *98* (C11), 20,299-20,305.

Emery, K.O. (1958), Wave patterns off Southern California, *Journal of Marine Research*, *17*, 133-140.

Feddersen, F., and R.T. Guza (2003), Observations of nearshore circulation: Alongshore uniformity, *Journal of Geophysical Research*, *108* (C1), 3006.

Feddersen, F., R.T. Guza, and S. Elgar (2004), Inverse modeling of one-dimensional setup and alongshore current in the nearshore, *Journal of Physical Oceanography*, *43* (4), 920-933.

Freilich, M.H., and R.T. Guza (1984), Nonlinear effects on shoaling surface gravity waves, *Philosophical Transactions of the Royal Society Series A*, *311*, 1-41.

Freilich, M.H., R.T. Guza, and S.L. Elgar (1990), Observations of nonlinear effects in directional spectra of shoaling gravity waves, *Journal of Geophysical Research*, *95* (C6), 9,645-9,656.

Gotwols, B.L., and G.B. Irani (1980), Optical determination of the phase velocity of short gravity waves, *Journal of Geophysical Research*, *85* (C7), 3964-3970.

Gotwols, B.L., and G.B. Irani (1982), Charged-coupled device camera system for remotely measuring the dynamics of ocean waves, *Applied Optics*, *21* (5), 851-860.

Guza, R.T., M.C. Clifton, and F. Rezvani (1988), Field intercomparisons of electromagnetic current meters, *Journal of Geophysical Research*, *93* (C8), 9302–9314.

Haller, M.C., R.A. Dalrymple, and I.A. Svendsen (2002), Experimental study of nearshore dynamics on a barred beach with rip channels, *J. Geophys. Res.*, *107* (C6), doi:10.1029/2001JC000955.

Holland, K.T., and R.A. Holman (1993), The statistical distribution of swash maxima on natural beaches, *Journal of Geophysical Research*, *98* (C6), 10,271-10,278.

Holland, K.T., and R.A. Holman (1997), Video estimation of foreshore topography using trinocular stereo, *Journal of Coastal Research*, *13* (1).

Holland, K.T., R.A. Holman, T.C. Lippmann, J. Stanley, and N. Plant (1997), Practical use of video imagery in nearshore oceanographic field studies, *IEEE Journal of Ocean Engineering*, *22* (1).

Holland, K.T., J.A. Puleo, and T.N. Kooney (2001), Quantification of swash flows using video-based particle image velocimetry, *Coastal Engineering*, *44*, 65-77.

Holland, K.T., J.A. Puleo, N.G. Plant, and J.M. Kaihatu, (2002), Littoral Environmental Nowcasting System (LENS), in *IEEE Oceans Conference*, pp. 1234-1240.

Holman, R.A., and R.T. Guza (1984), Measuring run-up on a natural beach, *Coastal Engineering*, *8*, 129-140.

Holman, R.A., T.C. Lippmann, P.V. O'Neill, and K. Hathaway (1991), Video estimation of subaerial beach profiles, *Marine Geology*, *97*, 225-231.

Holman, R.A., J. A.H. Sallenger, T.C. Lippmann, and J.W. Haines (1993), The application of video image processing to the study of nearshore processes, *Oceanography*, *6* (3), 78-85.

Holman, R.A., and J. Stanley (2007), The history and technical capabilities of Argus, *Coastal Engineering*, *54* (6-7), 477-491.

Hopkinson, R.G. (1954), Measurements of sky luminance distribution at Stockholm, *Journal of the Optical Society of America*, *44* (6), 455-459.

Johnson, D., (2002), DIWASP, a directional wave spectra toolbox for MATLAB®: User Manual, Center for Water Research, University of Western Australia.

Kasevich, R.S. (1975), Directional wave spectra from daylight scattereing, *Journal of Geophysical Research*, *80* (33), 4535-4541.

Komar, P.D., and D.L. Inman (1970), Longshore sand transport on beaches, *Journal of Geophysical Research*, *75*, 5914-5927.

Komar, P.D., and J. Oltman-Shay, Nearshore Currents, in *Handbook on Coastal and Ocean Engineering*, edited by J.B. Herbich, pp. 651-680, Gulf Publishing Co., Houston, TX, 1990.

Lippmann, T.C., and R.A. Holman (1989), Quantification of sand bar morphology: A video technique based on wave dissipation, *Journal of Geophysical Research*, *94* (C1), 995-1011.

Lippmann, T.C., and R.A. Holman (1990), The spatial and temporal variability of sand bar morphology, *Journal of Geophysical Research*, *95* (C7), 11,575-11,590.

Long, C.E., and J.M. Oltman-Shay, (1991), Directional characteristics of waves in shallow water, Coastal Eng. Res. Cent., Field Res. Facil., U. S. Army Eng. Waterw. Exp. Sta., Vicksburg, Miss.

Long, J.W., and H.T. Özkan-Haller (2005), Offshore controls on nearshore rip currents, *Journal of Geophysical Research*, *110* (C12007).

Longuet-Higgins, M.S., D.E. Cartwright, and N.D. Smith, (1963), Observations of the directional spectrum of sea waves using the motions of a floating buoy, in *Proceedings of the Conference of Ocean Wave Spectra*, pp. 111-132, Prentice Hall.

Longuet-Higgins, M.S., and R.W. Stewart (1964), Radiation stresses in water waves; a physical discussion, with applications, *Deep-Sea Research*, *11*, 529-562.

Longuet-Higgins, M.S. (1970), Longshore currents generated by obliquely incident sea waves, 2, *Journal of Geophysical Research*, *75*, 6790-6801.

Lubard, S.C., J.E. Krimmel, L.R. Thebaud, D.D. Evans, and O.H. Shemdin (1980), Optical image and laser slope meter intercomparisons of high frequency waves, *Journal of Geophysical Research*, *85* (c9), 4996-5002.

Marquardt, D.W. (1963), An Algorithm for Least-Squares Estimation of Nonlinear Parameters, *Journal of the Society for Industrial and Applied Math*, *11* (2), 431-441.

Mei, C.C., *The Applied Dynamics of Ocean Surface Waves*, 740 pp., John Wiley & Sons, New York, N.Y., 1983.

Monaldo, F.M., and R.S. Kasevich (1981a), Daylight imagery of ocean surfce waves for wave spectra, *Journal of Physical Oceanography*, *11*, 272-283.

Monaldo, F.M., and R.S. Kasevich (1981b), Measurement of short-wave modulation using fine time-series optical spectra, *Journal of Physical Oceanography*, *11*, 1034-1036.

Moon, P., and D.E. Spencer (1942), Illumination from a non-uniform sky, *Trans. Illum. Eng. Soc. (NY)*, *37*, 707–726.

Munk, W.H., and M.A. Traylor (1947), Refraction of ocean waves: a process linking underwater topography to beach erosion, *Journal of Geology*, *55*, 1-26.

Oltman-Shay, J.M., and R.T. Guza (1984), A data-adaptive ocean wave directional-spectrum estimator for pitch and roll type measurements, *Journal of Physical Oceanography*, *14*, 1800-1810.

Pawka, S., Wave directional characteristics on a partially sheltered coast, Ph.D. dissertation thesis, Scripps Inst. of Oceanography, University of California, San Diego, 1982.

Pawka, S. (1983), Island shadows in wave directional spectra, *Journal of Geophysical Research*, *88* (C4), 2579-2591.

Percival, D.B., and A.T. Walden, *Spectral analysis for physical applications: multitaper and conventional univariate techniques*, 583 pp., Cambridge University Press, New York, 1993.

Plant, N.G., R.A. Holman, and M.H. Freilich (1999), A simple model for interannual sand bar behavior, *Journal of Geophysical Research*, *104* (C7), 15755-15776.

Plant, N.G., K.T. Holland, and J.A. Puleo (2002), Analysis of the scale of errors in nearshore bathymetric data, *Marine Geology*, *191* (1), 71-86.

Putrevu, U., J. Oltman-Shay, and I.A. Svendsen (1995), Effect of alongshore nonuniformities on longshore current predictions, *Journal of Geophysical Research*, *100* (C8), 16119-16130.

Regier, L.A., and R.E. Davis (1977), Observations of the power and directional spectrum of ocean waves, *Journal of Marine Research*, *35* (3), 433–452.

Reniers, A.J.H.M., E.B. Thornton, and T.C. Lippmann, (1995), Longshore currents over barred beaches, in *Coastal Dynamics '95*, pp. 413-424, Am. Soc. of Civ. Eng., New York.

Reniers, A.J.H.M., and J.A. Battjes (1997), A laboratory study of longshore currents over barred and non-barred beaches, *Coastal Engineering*, *30* (1), 1-21.

Ruessink, B.G., J.R. Miles, F. Feddersen, R.T. Guza, and S. Elgar (2001), Modeling the alongshore current on barred beaches, *Journal of Geophysical Research*, *106* (C10), 22451-22464.

Sallenger, A.H., Jr., and R.A. Holman, Wave-energy saturation on a natural beach of variable slope, in *Journal of Geophysical Research*, pp. 11,939-11,945, 1985.

Sancho, F.E., I.A. Svendsen, A.R.V. Dongeren, and U. Putrevu, (1995), Longshore nonuniformities of nearshore currents, in *Coastal Dynamics '95*, pp. 425-436, Am. Soc. of Civ. Eng., New York.

Shepard, F.P., K.O. Emery, and E.C. La Fond (1941), Rip currents: a process of geological importance, *Journal of Geology*, *49*, 337-369.

Slinn, D.N., J.S. Allen, and R.A. Holman (2000), Alongshore currents over variable beach topography, *Journal of Geophysical Research*, *105* (C7), 16971-16998.

Smith, J.M., M. Larson, and N.C. Kraus (1993), Longshore current on a barred beach: Field measurements and calculation, *Journal of Geophysical Research*, *98* (C12), 22,717-22,731.

Stilwell, D. (1969), Directional energy spectra of the sea from photographs, *Journal of Geophysical Research*, *74* (8), 1974-1986.

Stilwell, D., and R.O. Pilon (1974), Directional spectra of surface waves from photographs, *Journal of Geophysical Research*, *79* (9), 1277-1284.

Stockdon, H.F., and R.A. Holman (2000), Estimation of wave phase speed and nearshore bathymetry from video imagery, *Journal of Geophysical Research*, *105* (C9), 22,015-22,033.

Svendsen, I.A. (1984a), Wave heights and set-up in a surf zone, *Coastal Engineering*, *8*, 303-329.

Svendsen, I.A. (1984b), Mass flux and undertow in a surf zone, *Coastal Engineering*, *8*, 347-365.

Thomson, J., S. Elgar, T.H.C. Herbers, and B. Raubenheimer (in press), Refraction and reflection on infragravity waves near submarine canyons, *Journal of Geophysical Research*.

Thornton, E.B., and R.T. Guza (1986), Surf zone longshore currents and random waves: Field data and models, *Journal of Physical Oceanography*, *16* (7), 1165-1178.

van Enckevort, I.M.J., and B.G. Ruessink (2001), Effect of hydrodynamics and bathymetry of video estimates of nearshore sand bar position, *Journal of Geophysical Research*, *106* (C8), 16,969 - 16,979.

Walker, R.E., *Marine light field statistics*, 675 pp., John Wiley and Sons, Inc., New York, 1994.

APPENDIX

Appendix: Alpha array directional resolution tests for synthetic sea surface elevation variations

The fidelity of frequency-direction spectral estimation is a function of both design of the alpha array MLE processing, and the input data, and therefore cannot be specified in general. Synthetic tests to assess the sensitivity and associated error of the MLE processing for the Alpha array, using simulated seas surface elevation variation alone, and not optical simulations, were computed while varying the directional spread and signal-to-noise ratios and while allowing uni-modal and bi-modal distributions. Expected wavenumber (hence frequency) sensitivities to alpha array design details were also examined. Wave spectra were designed as Gaussian directional distributions, with a noise floor, at each frequency

$$S(\theta) = A\exp\left[\frac{-(\theta-\theta_p)^2}{2\sigma_\theta}\right] + A_n \tag{A1}$$

where A is the power density amplitude at the peak, θ_p is the wave direction at peak amplitude, σ_θ is the standard directional width, and A_n is the constant background noise amplitude. The relative contribution of background noise is expressed as the noise-to-signal ratio (NSR), equal to A_n/A. Simulations were run for an alpha array designed for a 5.5s period wave in constant water depth of 5m. The resulting maximum cross-shore and alongshore dimensions of the test array are 34m and 68m, respectively. Times series of sea surface elevation of 1024s with sampling rate of 2Hz were simulated at each instrument. Complex Fourier coefficients were constructed with squared amplitudes according to (A1) with random phases assigned at each frequency, and for wave directions from 90 to -90 degrees at 1 degree bins. Wavelengths at each frequency were calculated using linear wave theory. The complex frequency-direction spectrum was inverse Fourier transformed with respect to frequency and integrated with respect to wave direction. This is repeated for each instrument in the array. MLE frequency-wavenumber-direction spectral estimates were calculated as outlined in section 3.1,

with a window length of 64s (128 points), and integrated with respect to direction. The performance of the MLE method, was assessed by comparing the optical estimate, $\hat{S}$, to the true directional spectrum, S, at any frequency using the normalized square error (NSE)

$$NSE = \frac{\sum_{i=1}^{N}\left[\hat{S}(\theta_i) - S(\theta_i)\right]^2}{\sum_{i=1}^{N} S^2(\theta_i)}, \qquad \text{(A2)}$$

where N is the number of directional estimates at any frequency.

The bias of frequency was examined using unimodal spectra with $\theta_p = 0°$ and varying levels of NSR (0.01 to 0.5) and σ_θ (5 to 90 degrees), for a total of 90 different spectra. Twenty-five realizations of each spectrum were processed and averaged to reduce noise of small sample statistics. Figure A1a shows the average and standard deviation of the NSE for each wavenumber (wavenumbers were calculated with linear wave theory at 5m water depth and displayed relative to the Nyquist wavenumber of the array, k_{nyq}, to generalize results) over the range of tests, and demonstrates the generally low NSE (< 0.3) for wavenumbers smaller than the expected Nyquist wavenumber, and particularly low NSE (< 0.1) for wavelengths less than about $k/k_{nyq} < 0.1$. The noticeable maximum in NSE for wavenumbers where $k/k_{nyq} > 0.1$ could be due to preferential sampling of longer wavelengths in the alpha array. Figure A1b shows the dependence of NSE on increased background noise (NSR). On average NSE increases slightly with increasing NSR, from about 0.1 to less than 0.2. Estimated full directional widths from MLE spectra, agree well for $2\sigma_\theta$ less than 70° from array normal (Figure A1c).

MLE spectra were tested for peak direction identification for bimodal directional distributions. Test spectra were created with equal magnitude peaks with separations, $\Delta\theta$, of 10 to 120 degrees, by 10 degree steps, and with σ_θ of 5, 10 and 20 degrees. Again, 25 realizations of each test spectrum were processed and averaged. Figure A2a shows the identified direction peak location normalized by

total peak width, $2\sigma_\theta$. The identified MLE peaks are least accurate (denoted by overlapping or near-overlapping of standard error bars around mean locations) when $\Delta\theta \leq 2\sigma_\theta$, which is predictable, because the sum of two Gaussian distributions with equal amplitude, standard deviation, and peak separations less than 2σ do not have two distinct peaks. General fidelity of the MLE spectra for bimodal distributions is acceptable with NSE less than about 0.15 for all $\Delta\theta$ and σ_θ choices (Figure A2b).

The final synthetic data test examines the consequences of differences in actual pixel sample locations compared to design locations. These discrepancies would be associated with limitations in pixel resolution, not with errors associated, for example, with image photogrammetry. Directional bimodal spectra with $\Delta\theta$ = 60°, σ_θ = 10°, NSR = 0.1 were simulated for alpha arrays such that the position of the i^{th} element in the modified array (x_i', y_i') is the original position of the array element (x_i,y_i) with the addition of a randomly oriented vector for each element,

$$x_i' = x_i + \varepsilon_x l_x \cos(\varphi_i), \quad y_i' = y_i + \varepsilon_x l_x \sin(\varphi_i), \tag{A3}$$

where ε_x is a fraction of the total cross-shore dimension, l_x, of the basic alpha array, and φ_i is a random angle between 0 and 2π radians. Twenty-five realizations for each selection of ε_x = 0.05, 0.1, 0.2, and 0.5 were simulated and MLE spectra estimated. The results (Figure A3) show that the average NSE < 0.1 for the range of ε_x. Given that a choice of ε_x = 0.5 results in a ~15m shift in each element of the array, it is clear that a nearly random array of points with appropriate total horizontal span can produce accurate spectral estimations. This provides authority for the use of any "instruments-of-opportunity", or in the case for this paper, pixels-of-opportunity.

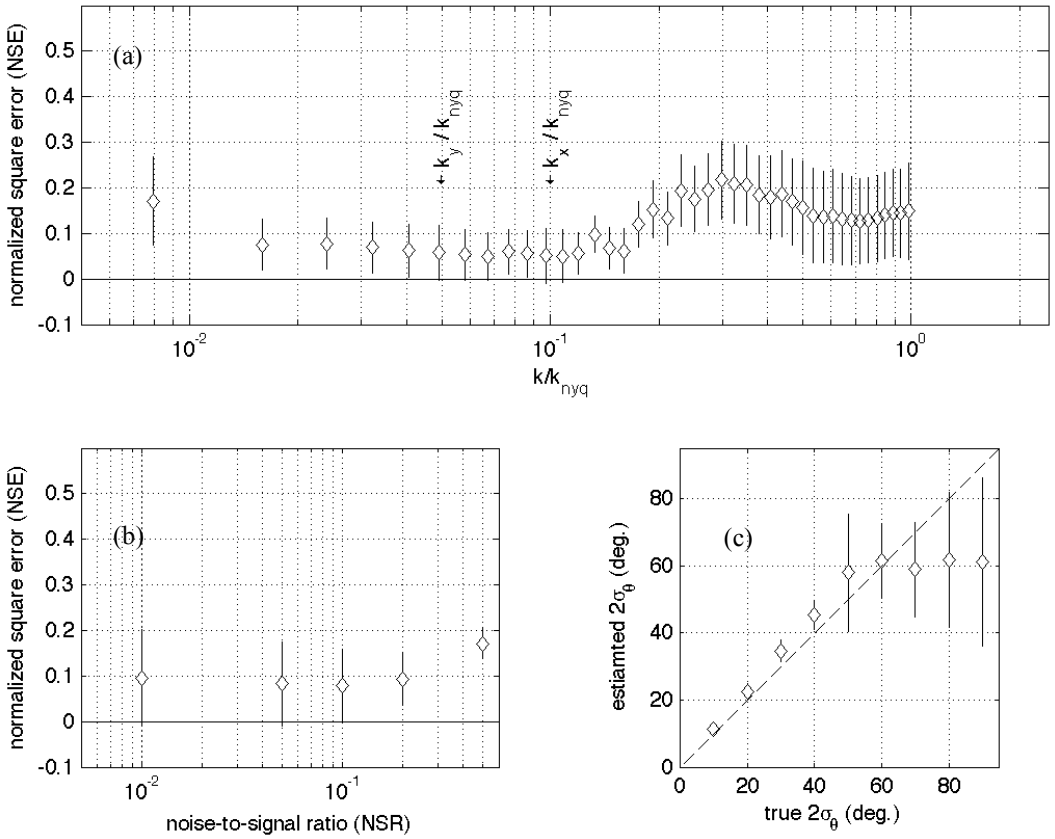

Figure A1. (a) Normalized square error (NSE) of MLE spectral distributions versus relative wavenumber for an alpha array. (b) NSE for MLE spectra versus varying noise-to-signal levels. (c) Full standard widths ($2\sigma_\theta$) of MLE spectra versus true standard widths; a theoretical one-to-one correspondence is shown (dashed line). Results in all panels are shown as mean (symbols) and standard deviations (vertical lines) for all unimodal synthetic tests.

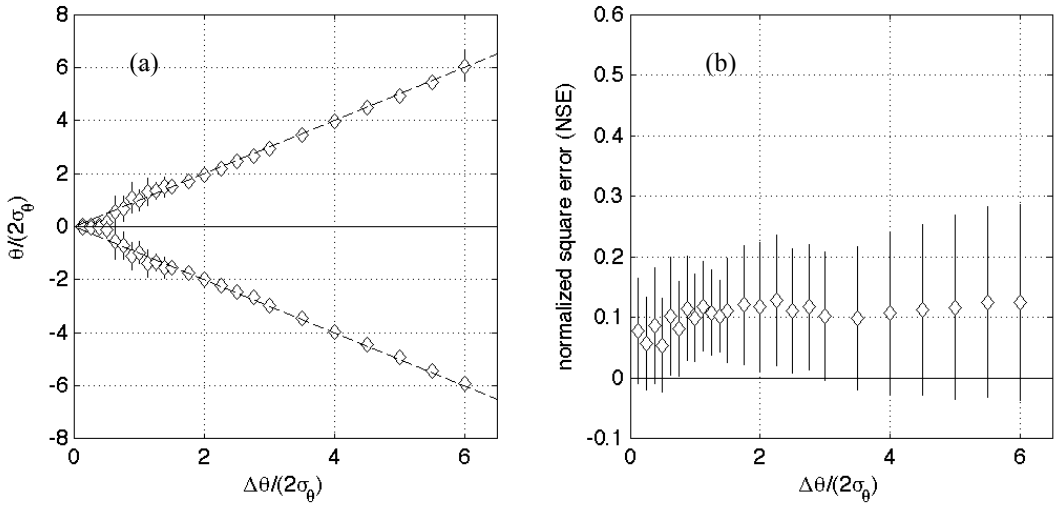

Figure A2. (a) Measured mean (symbols) and standard deviations (vertical lines) of MLE peak locations for all bimodal directional distributions tests (see Appendix A), versus true peak separation, $\Delta\theta$. Units have been normalized by peak FSW ($2\sigma_\theta$), and dashed lines indicate where perfect agreement lies. (b) NSE of directional distributions versus normalized peak separation.

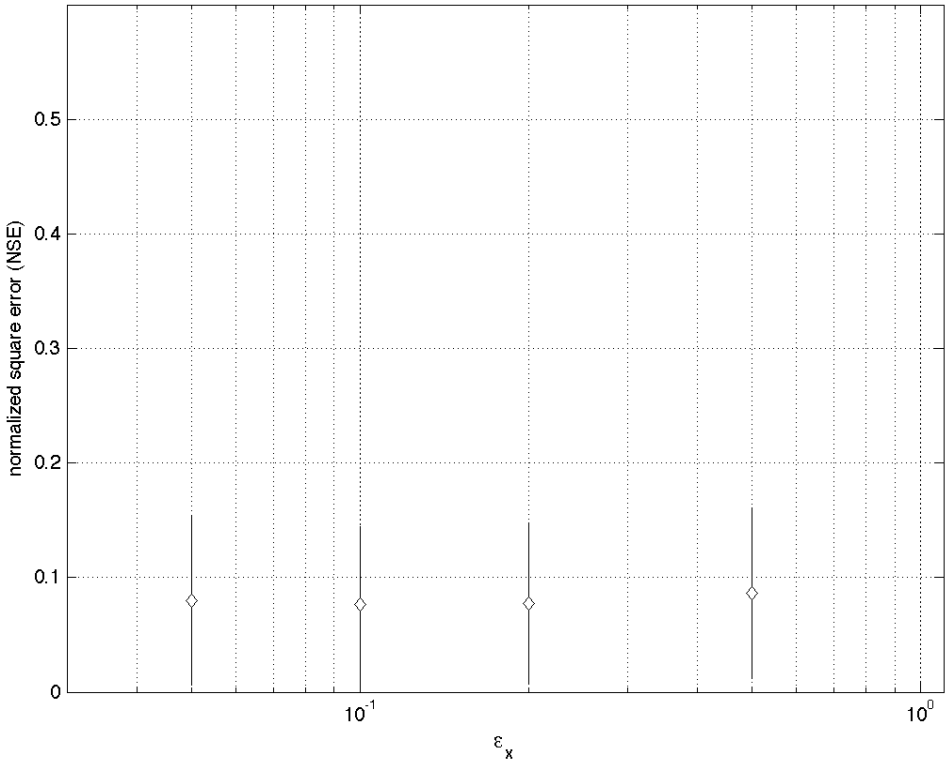

Figure A3. The averaged and standard deviation of the NSE for synthetic bimodal spectra versus varying position shifts, ε_x (a fraction of the cross-shore dimension of the array, l_x) , in each element of the alpha array.